



This is to certify that the

dissertation entitled

HIGHLY DISPERSED METALS IN PILLARED CLAYS.
PROPERTIES AS FISCHER-TROPSCH CATALYSTS

presented by

Edward Gordon Rightor

has been accepted towards fulfillment of the requirements for

Ph.D. degree in Chemistry

Date Nov. 7, 1986



RETURNING MATERIALS:
Place in book drop to remove this checkout from your record. FINES will be charged if book is returned after the date stamped below.

HIGHLY DISPERSED METALS IN PILLARED CLAYS. PROPERTIES AS FISCHER-TROPSCH CATALYSTS

Ву

Edward Gordon Rightor

A DISSERTATION

Submitted to
Michigan State University
in partial fulfillment of the requirements
for the degree of

DOCTOR OF PHILOSOPHY

Department of Chemistry

1986

ABSTRACT

HIGHLY DISPERSED METALS IN PILLARED CLAYS. PROPERTIES AS FISCHER-TROPSCH CATALYSTS

By

Edward Gordon Rightor

Recently developed methods (1,2) were utilized for the synthesis of highly dispersed Fischer-Tropsch active metals in the microporous regions of pillared clays. The stability, activity, and distribution of hydrocarbons formed on the resulting catalytic sites were investigated.

The first method (1) involved intercalation of hydroxyiron polycations into the clay galleries, followed by conversion of the polycations to Fischer-Tropsch active sites. The iron pillars produced primarily C_1 - C_7 paraffins and olefins, although minor amounts of branched hydrocarbons and C_1 - C_3 alcohols also were detected. Microanalysis in a scanning electron microscope indicated significant bulk iron inhomogeneities and iron enrichment at clay edges. X-ray diffraction revealed that even though the Fe-pillared clay was ordered and stable when calcined (air, 350°C), it was XRD amorphous after catalysis or after storage in air for a few months. This was most likely due to pillar hydrolysis.

In the second method (2), ruthenium carbonyls were selectively dispersed in the micropores of alumina pillared

montmorillonite (APM). These Ru sites were catalytically active without prereduction and gave non Schulz-Flory hydrocarbon product distributions initially. Conversely, prereduced Ru/APM catalysts did not show significant Schulz-Flory deviations, but exhibited greater conversions and enhanced production of high molecular weight products.

High resolution electron microscope studies (3) of nonprereduced Ru/APM after 30 hrs of reaction proved that Ru aggregated into large crystallites located on the external surfaces of the pillared clay. In contrast, prereduced catalysts gave a narrow distribution of small Ru microcrystallites that were mainly retained inside the pillared clay particles. A model was proposed that explained the location of relatively large crystallites (6nm) within void spaces created by layer packing disorders. Z-contrast imaging showed small microcrystallites in thicker regions of the clay which gave support for this model.

These Ru/APM catalysts exhibited high selectivities for internal olefins and branched hydrocarbons, an unusual result for Ru-based Fischer-Tropsch catalysts. The yields of these atypical isomer fractions were studied by variation of reaction variables and the addition of 1-olefin probe molecules. These experiments gave support to the proposal that this high isomerization selectivity is due to the strong intracrystalline acidity of alumina pillared clay.

REFERENCES

- 1. Tzou, M.S., Ph.D. Dissertation, Michigan State University, 1983.
- 2. Gianellis, E.P., Ph.D. Dissertation, Michigan State University, 1984.
- 3. Rightor, E.G.; Pinnavaia, T.J., to be published in <u>Ultramicroscopy</u>, 1986.

To Elizabeth McKenzie Keller and J. Gordon McKenzie

ACKNOWLEDGMENTS

Dr. T. J. Pinnavaia has provided generous support and encouragement along with the appropriate amount of guidance during my graduate studies, for which I am deeply grateful. He was always able to paint a broad picture of my Ph.D. project, which helped considerably in surmounting the short-range frustrations characteristic of research. His depth of knowledge, enthusiasm for science, and amiable personality are qualities I admire and I look forward to future association with him.

I would like to express my gratitude to Dr. D. G.

Nocera for his dedication and flexibility in editing this
dissertation despite his hectic schedule. I would also like
to acknowledge Dr. H. A. Eick for helpful discussions.

Additionally, the support personnel in the chemistry
department were excellent and I appreciate their efforts.

The patience, approachability and generosity of Mr.

Vivion Shull, Dr. Karen Klomparens and Dr. Stan Flegler was crucial in learning technical aspects of electron microscopy methods, for which I would like to express my thanks. Dr. John Heckman and Ms. Genevieve Macomber provided additional technical assistance. Arizona State University awarded me a scholarship to their NSF-sponsored

"Imaging and Microanalysis School," which was greatly appreciated.

Throughout my graduate studies my mother has been a continual source of encouragement, support, and love which has made it possible for me to presevere in this undertaking. Kathy Smith, my fiancee, devoted many hours to the word-processing of this dissertation and aided in the processing of the electron micrographs. Her support, inspiration, and dedication helped me make it through the final stages.

Finally, I would like to thank my friends, previous and present group members, and two super lab partners, Dr. Ivy Johnson and Todd Werpy, for their encouragement and understanding.

TABLE OF CONTENTS

Pa	ge
LIST OF TABLES	ii
LIST OF FIGURES vi	ii
CHAPTER I - INTRODUCTION	1
A. Constrained Systems	1
B. Clay Minerals	9
C. Fischer-Tropsch	20
D. Research Objectives	34
CHAPTER II - EXPERIMENTAL METHODS	37
A. Clay Preparation	37
B. Preparation of Alumina Pillared Montmorillonite (APM)	38
C. Immobilization of Ruthenium Carbonyl on APM	39
D. Catalysis	40
E. Electron Microscopy	48
F. Physical Measurements	50
G. Chemical Analysis	51
CHAPTER III - IRON-PILLARED CLAYS	53
A. Introduction	53
B. Synthesis and Physical Properties	62
C. Fischer-Tropsch Catalysis	67
D. Scanning Electron Microscopy	78
E. X-Ray Diffraction	92

F	•	Conclusions	94
CHAPT	ER	IV - RUTHENIUM ON ALUMINA PILLARED MONTMORILLONITE	98
A	١. :	Physical Properties of APM and Ru/APM 1	04
В	3.	Pristine vs. Prereduced Ru/APM Catalysts 1	.06
c	: .	Electron Microscopy	14
D		Nature of Ru Microcrystallites 1	33
E		Atypical Features of Ru/APM Fischer-Tropsch Catalysts	.39
F	٠.	Isomerization Mechanisms 1	54
G		Alkene Probe Additions and H ₂ /CO Variation	.60
Н	Ι.	Conclusions	.75
APPEND	XIC	A: Minimization of Microscope Artifacts 1	.79
APPENI	DIX	B: Feed Gas Impurities	83
APPENI	DIX	C: Preparation of Oxygen Scrubber 1	88
REFERI	ENC	ES	9.0

LIST OF TABLES

<u>Table</u>		Page
1	Shape Selectivity. Comparison of hydrogenation on Pt/Al ₂ O ₃ vs. Pt/ZSM-5, from ref. 10	5
2	Important Synthesis Gas Reactions. Adapted from 75,70	22
3	Solubility Products of Fe(III) Oxides. Adapted from 111, 25°C, Zero Ionic Strength .	58
4	Sorption of Probe Molecules on Fe/PILC	58
5	Summary of Physical Data for Fe/PILC	58
6	Summary of an Typical Fe/PILC FT Product Distribution	66
7	Summary of Physical Data for Al-Pillared Clays	103
8	Ru/APM Catalytic Data at 1 atm	110

LIST OF FIGURES

Figure		Page
1	Channel structure of ZSM-5 and ZSM-11 zeolites. Adapted from reference 6	4
2	Molecular sieving of common zeolites. Adapted from reference 6	4
3	The framework structure of montmorillonite, an typical smectite. Adapted from ref. 16	11
4	Schematic representation of pillared clay, along with various classes of pillars. From ref. 17	11
5	Influence of Process Variables on Fischer- Tropsch	22
6	Fischer-Tropsch Reaction Mechanisms	25
7	Comparison (a) between a experimental non-SF distribution (open symbols, 91), with a ESF curve (closed symbols, 95). For curve (A) Co/Al2O3 the mean pore radius was 6.5nm, and in (B) it was 30nm. The particle size distributions used to generate the ESF plots are given in (b). Reproduced from ref. 95	32
8	Reactor setup for catalyst studies with Fe/PILC	41
9	Reactor system for catalytic character ization of Ru/APM	45
10	Iron(III) hydrolysis and polymerization, as shown by Flynn (111). The numbers in parenthesis refer to relative reaction rates	57
11	Change in the pH of Fe/PILC sols during the process of washing (A), and XRD patterns (B) of air dried FE/PILC films after selected washings. The arrow in (A) indicates the pH and washing at which flocculation first occurred	64

Figure		Page
12	Schulz-Flory plots of Fe/PILC hydrocarbon production after 60 min. ⊙ ,103 min. △ , and ⊡ 1259 min. of reaction. Reaction conditions were 120 psi, 275oC, H2/CO=2, 2100 hr-1 GHSV, and 1.7s contact time	68
13	Experimental hydrocarbon production \odot for Fe/PILC (60min. TOS) compared to an calculated (Schulz-Flory) distribution. A chain growth probability of 0.42 was used for the SF plot. Experimental data from Figure 12.	71
14	Experimental hydrocarbon production ① for Fe/PILC (1259min. TOS) compared to calculated ① (Schulz-Flory) distribution. A chain growth probability of 0.49 was used for the SF plot. Experimental data from Figure 12.	72
15	Olefin/paraffin production for Fe/PILC cat- alysts as a function of conversion for C3=/C3- and C2=/C2	76
16	Edge-on SEM view (a) of Wyoming Na+-mont-morillonite air dried on glass. SEM image (b) near a crack in the air dried clay	81
17	SEM images of Fe/PILC air dried on glass at various magnifications. The substantial decrease in layer bending is evident at all magnifications	83
18	Generation of various signals in samples due to interaction with the beam in electron microscopes	85
19	SEM image of Fe/PILC (a) and the elemental distribution (b) determined by an x-ray microanalysis linescan	87
20	SEM of a different area (a) and an accompanying linescan (b) between the arrows	87
21	SEM image of the undulating surface of Na+ montmorillonite (a) and an x-ray microanal- ysis linescan (b)	91
22	Elemental microanalysis of Na+-montmor- illonite between the arrows in Figure 16a .	91
23	Elemental linescan of a well ordered Cr- pillared montmorillonite. Here the Cr dis- tribution follows that of Si, indicating a homogeneous pillared clay	91
		<i>3</i> T

Figure		Page
24	XRD patterns of Fe/PILC before and after Fischer-Tropsch reaction. The initially well ordered material (top) was essentially XRD amorphous after 3 months in air	93
25	Arrangement of detectors in the specimen chamber of a dedicated STEM. Reproduced from ref. 148	103
26	Infrared spectra of Ru/APM (a) immediately after synthesis (2130, 2104, 2080 cm-1), (b) prior to catalysis, aged 1 month in dessicator, (2150, 2080 cm-1), (c) post catalysis after 12.5 hrs, 225oC rxn. (2100, 2056 cm-1). a. ordinate expansion 400x	105
27	Schulz-Flory plots for Ru/APM catalysts after 8 min. ⊙ , and 138 min. △ of Fischer-Tropsch. The catalyst was not prereduced prior to reaction. Reaction conditions: 275oC, 8 atm., 300 hr-1, H2/CO=2	108
28	Comparison of Schulz-Flory plots for prereduced ⊙ and nonprereduced △ catalysts at 275oC. A prereduced catalyst run at 225oC gave the distribution shown by ⊡ . Reaction conditions: 1 atm., 300 hr-1, 50 min. TOS.	113
29	Dark field image of Ru/APM catalyst after 30 hrs. of catalysis at 275oC showing Ru aggregates. The catalyst was not reduced prior to catalysis. Arrows indicate aggregate exam]ned by the EDS analysis in Figure 33	117
30	Dark (a) and bright field (b) images of the Ru/APM catalyst showing a coalesced Ru particle. Catalyst was not prereduced	117
31	Twinned Ru aggregate on a Ru/APM post-run catalyst sample not reduced prior to catalysis. The catalyst was run for 30 hrs. of FT catalysis	117
32	Ruthenium crystallite sizes observed by STEM for nonprereduced catalysts after 30 hrs. of FT reaction at 275oC. Here ni is the number of particles with diameter di, dn is the number average and ds is the surface average particle size	110
		118

Figur	<u>ce</u>	Page
33	EDS spectrum from the Ru crystallite indi- cated in Figure 29. The Cu peaks are arti- facts originating from the Cu microscope grids	120
34	Ru crystallite sizes determined by STEM studies on numerous Ru/APM particles after 30 hrs. of reaction	120
35	Representative prereduced Ru/APM catalyst particle, found by STEM bright field (a), and dark field images (b), showing small Ru microcrystallites. An EDS microanalysis is given in Figure 35c. The catalyst was run for 30 hrs. of FT at 275oC and 1 atm	123
350	EDS spectrum from the 5 nm microcrystallite indicated in Figure 35	124
36	Model of air dried pillared clay showing mesopores created by layer packing disorders and layer bending. Plausible locations of Ru microcrystallites >2nm (labeled Ru), and less than 2nm (filled triangles) are indicated. Slabs represent clay layers and small open circles the "alumina" pillars	130
37	Pore size distribution of APM from liquid nitrogen desorption isotherms. Here rp is the mean pore radius, and Vp is the change in pore volume	131
38	Dark field (a) image of Ru/APM after catalysis. The area indicated in (a) is shown below in (b), using the Z-contrast ratio imaging technique, which shows microcrystallites < 5nm. Catalyst prereduced	135
39	Bright field (a) and difference Z-contrast image (b) for a prereduced Ru/APM catalyst particle showing the ability of Z-contrast to image Ru in thicker clay regions	135
40	STEM bright field image (a) for prereduced APM following FT catalysis. Nanodiffraction patterns (b) and (c) are from the microcrystallites indicated. (Provided courtesy of J. M. Cowley, Arizona State University).	138
	_ ·	

Figure		Page
41	Representative gas chromatograms for prereduced Ru/APM catalysts showing production of branched and internal olefin products. Chromatogram (a) is for the gaseous fraction, and (b) illustrates the components in the condensed liquid	140
42	Variation of the branched/straight chain hydrocarbon selectivities with temperature for Ru/APM catalysts. The symbols represent C4 ⊙, C5 ⊡, C6 △ and C7 ⊙ hydrocarbon fractions. The FT conditions were; 120 psi., 1910 hr-1, H2/C0= 2, 50 min. TOS, prereduced.	142
43	Change in the branched/straight hydrocarbon ratio ,normalized for conversion variation, at various pressures. Here the □ represent data at 1 atm, △ at 70 psi , and ⊙ at 190 psi. Intermediate pressures follow these trends but are excluded for clarity. Reaction conditions; 250oC, 1910 hr-1, H2/CO =2,50 min TOS	144
44	Production of Branched/straight hydrocarbons at longer run times (100 min.) for C4 ⊙, ⊡ C5 C6 △ and C7 ⊙ hydrocarbons. Run conditions were the same as in Figure 42	146
45	Steady state (200 min.) selectivity for branched hydrocarbons for C4 \odot , C5 \odot , C6 \triangle and C7 \odot products. Run conditions were the same as in Figure 42	147
46	Effect of space velocity on the branched/ straight ratio. The C4 hydrocarbons are represented by ⊙ ,C5 by ⊡ , C6 by △ , and C7 are shown by ⊙ . The slashed symbols show the ratio when the flow was returned to the original value. (275oC, 110 psi, H2/C0=2, 45 min TOS, prereduced, contact time from 1.3-0.33 seconds)	149
47	Production of internal olefins relative to terminal olefins (i Cn=/T Cn=), and n-alkanes (i Cn=/ Cn-) as a function of temperature. Here the symbols are defined as; iC4=/TC= is ①, iC4=/C4- ② , iC5=/TC5= △ , and iC5=/C5-is ①. Conditions were 120 psi. , 1910 hr-1, H2/CO=2, 50 min. TOS, prereduced	151

Figure		Page
48	Comparison of total alkene/alkane , norm-alized with respect to conversion, for 1 atm. ⊙,70 psi △ , and 190 psi ⊡ . FT conditions were; 250oC, 1910 hr-1, H2/CO=2, 50 min. TOS, prereduced	153
49	Ratio of alkenes to alkanes for Ru/APM catalysts as a function of flow rate. The symbols show C4 ⊙ , C5 ⊡ and C6 △ hydrocarbons. The slashed symbols show the recycle values. Conditions were 275oC, 110 psi., H2/C0=2, 45 min. TOS, contact time from 1.3-0.33 seconds	155
50	Yields of internal olefins relative to 1-alkenes and n-alkanes as a function of flow rate. Symbols are; iC4=/1-C4= ⊙ , iC4=/Cn- ⊙ ,i C5=/1-C5= △ and iC5=/Cn- ⊙ (275oC, 110 psi, H2/CO=2, 45 min. TOS, 1.3-0.33 sec. contact time)	156
51	Plausible mechanisms to account for hydro- carbon branching showing: (a) insertion of propene, (b) addition of chemisorbed methyl species, (c) isomerization associated with hydride shift, (d) formation and rearrange- ment of an alkylidiene, (e) carbocation rearrangements	159
52	Increase in hydrocarbon production resulting from incorporation of 1-alkene probe molecules. The symbols signify: steady state FT (100 min.) ⊙ ,hydrocarbon distribution during the first alkene addition △ , and after the second addition ⊡ . The [alkene] in the second addition was twice the first. (275oC,110psi.,4336 hr-1,H2/CO=2, prereduced.	162
53	Production of branched and straight hydrocarbons before and after 1-alkene additions. The \(\triangle \) show steady state FT (180 min.), \(\triangle \) and \(\triangle \) production after the first and second alkene additions, respectively. The slashed points are for straight isomers and the regular symbols are for branched products. (275oC, 110 psi., 4336 hr-1, H2/CO=2, prereduced)	163

Figure		Page
54	Breakdown of the 1-olefin probe molecules added during FT into internal olefins (iCn=), and total paraffins (Cn-). The regular symbols for FT steady state (180 min.) \odot , first addition \triangle , and second \boxdot refer to paraffins and the slashed symbols to internal olefins. FT conditions as in Figure 53	165
55	Transformation of 1-alkene probe molecules to alkanes in the absence of CO (no FT) as a function of the alkene to hydrogen ratio. The symbols represent; ⊙ C2, △ C3, △ C4, ⊙ C5, ⊡ C6, and C7. (275oC, 1 atm, 3230 hr-1)	168
56	Transformation of the added 1-alkene probes to internal olefins as a function of the alkene to hydrogen ratio. The symbols are; cisC4 ① , trans C4 ② , cis C5 △ , ※ trans C5 1-C4=①,1-C5=/\. (275oC, 1 atm., 3230 hr-1, prereduced)	169
57	Gas chromatograms of 1-alkene probe molecules after passing through the Ru/APM catalyst bed. (a) 25oC before any isomerizations, (b) reactor effluent when alkenes are added to the catalyst at 275oC, 1 atm., 3230 hr-1, 50 min. TOS, (1- Cn=/H2=1.25), (c) 1- Cn=/H2=2.8	170
58	Change in the selectivity for branched hydrocarbons during FT with H2/CO. The symbols are; ⊙ C4, △ C5, ⊡ C6, ⊙ C7, ∕ C8. (275oC, 120 psi.,3230 hr-1, prereduced).	172
59	Isomerized hydrocarbon production vs. normal FT production (n-alkanes and 1-alkenes) as a function of the H2/CO ratio. Here C4 hydrocarbons are shown as ⊙ , C5 as ⊡ , and C6 as △ . (275oC, 120 psi., 3230hr-1).	173
60	STEM dark field image of Ru crystallites formed by beam induced agglomeration in the microscope. Microdiffraction patterns are from the pseudo-hexagonal (b), and rectangular crystallites. Sample stage at room temperature	181
61	Ru/APM after 30 hrs. of FT reaction with feed gas containing carbonyl impurities at low (a), and high magnification (b). Microscope sample stage at room temperature	185

Figure		Page
62	EDS analyses of the aggregates indicated in Figure 61, which show the presence of Fe and	
	Ni impurities	186

Chapter I

Introduction

A. Constrained Systems

Chemical research involving the synthesis, characterization, and applications of constrained reaction systems has grown dramatically since 1960 into a broad, multidisciplinary area. The principle objective is to geometrically alter the local environment of molecules to induce unusual physical or catalytic properties. This can be accomplished by confining a guest molecule within a somewhat rigid host matrix. The reactivity of the quest is thus limited and interaction with reactant molecules may afford greater selectivity than obtained with free molecules. Suitable organic constrained systems can involve molecules or polymers that mimic enzymes, whereas inorganic systems are commonly materials with two or three dimensional pore networks. The diversity of materials being used to investigate the effects of molecular constrainment can be appreciated by considering the numerous classes of constrained systems which includes: cyclodextrins (1, 2); lipids and microemulsions (2); bilayered systems and graphite intercalants (1, 2, 3); zeolites and layered clays (2, 3); chalcogenides and β -aluminas (2, 3); and crystalline silicic acids (2, 3).

Some of the most effective inorganic constrained systems have been zeolites. Zeolites have demonstrated remarkable selectivity in transformations of organic molecules and provide an excellent example of the types of geometrical influence that many inorganic constrained systems strive to achieve. The synthesis and technical application of zeolites started with the first industrial research efforts in 1948 at Union Carbide, and has generated a new field of inorganic materials with vast scientific interest. In the twenty-five years following the commercial application of zeolites in 1954, over 15,000 scientific contributions and over 10,000 patents have explored this area(4). In 1979 the molecular sieve industry alone, was projected to be a 250 million dollar market (4).

Among the attractive characteristics of zeolites for industrial catalysis are their sharply defined pore sizes, high and adjustable intracrystalline acidity, and high surface areas. They also have excellent hydrothermal stabilities and their relatively easy synthesis from inexpensive raw materials makes them economically attractive.

Zeolites are crystalline aluminosilicates composed of a three-dimensional network of linked silica and alumina tetrahedra. The tetrahedra link through shared oxygens to form rings typically containing 4-12 tetrahedral units. These ring structures form the entrances to channels that define the diameter of pores that propagate throughout the structure (5). The size, and arrangement of the channels

resulting from connected pores are of utmost importance as they affect many unusual properties of these materials. Channel networks for two pentasil zeolites of particular catalytic importance (ZSM-5 and ZSM-11), are shown in Figure 1. The dimensions of zeolite pores and channels are similar to the critical dimensions of simple isoparaffins and substituted aromatics. The relationships between zeolite pore dimensions and hydrocarbon reactant, intermediate or product size then provides the fundamental basis for shape selective catalysis. The size and shape of the pores and channels influence the sorption of molecules into zeolite interiors. Figure 2 shows a comparison between zeolite window (pore) size and the kinetic diameters of representative sorbate molecules (6). Molecules with critical dimensions less than those of the pores can pass through these openings whereas molecules that are too large cannot. This leads to selective sorption of molecules, termed molecular sieving (7).

The shape selectivity of zeolites in catalysis, first reported by Weisz and Frilette (8), has become a dominant feature in catalytic applications. S. Csicsery (9), in a recent review on zeolite shape selectivity, distingushed four different types of selectivity:

(a) Reactant selectivity occurs when the pores of windows are too small to allow some reactant molecules to diffuse to active sites.

The hydrogenation of olefins and aromatics on Pt/ZSM-5

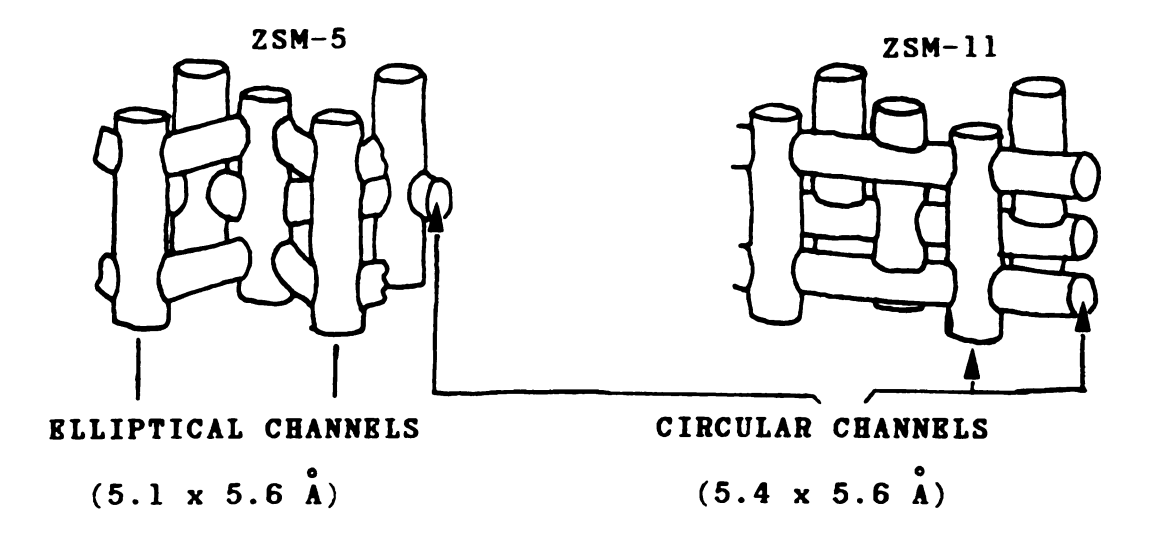


Figure 1. Channel structure of ZSM-5 and ZSM-11 zeolites. Adapted from reference 6.

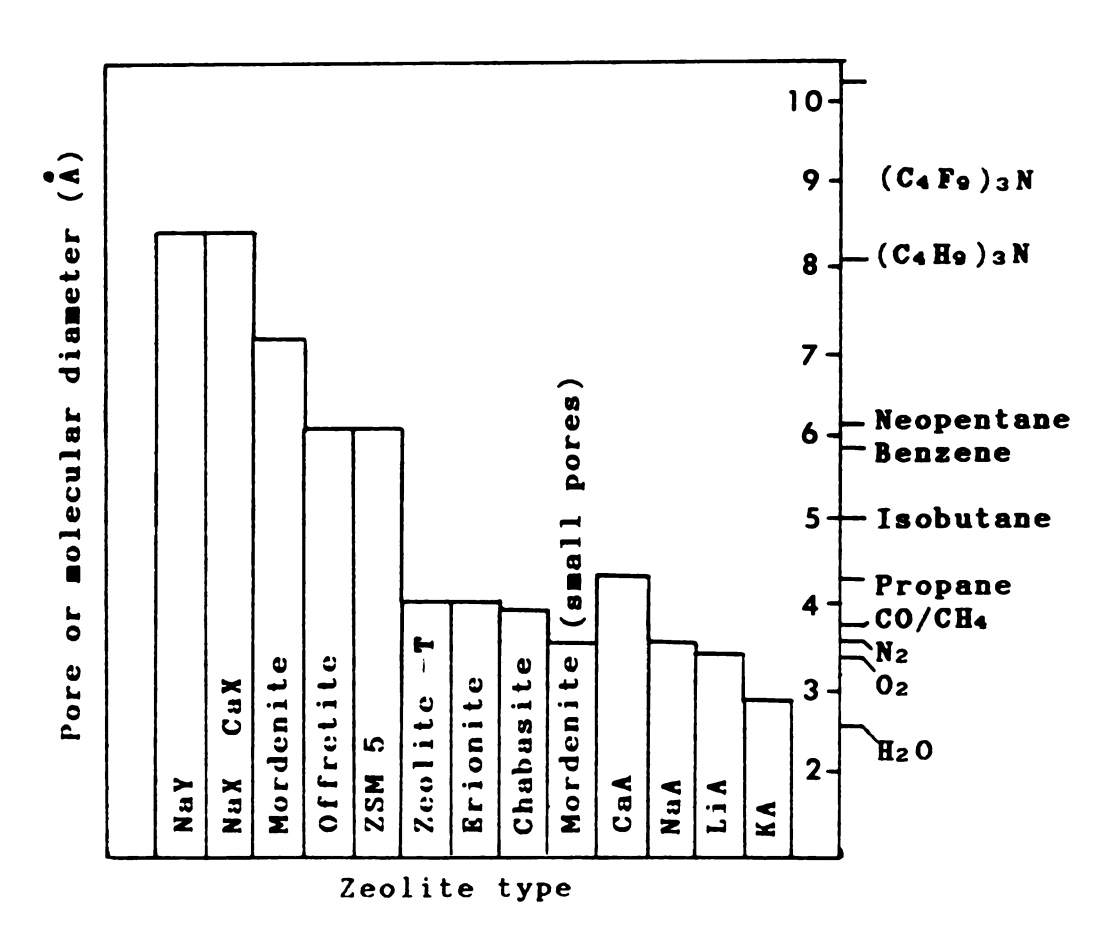


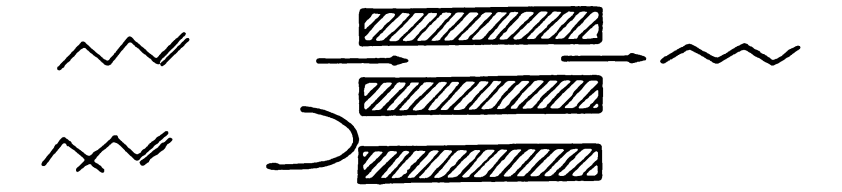
Figure 2. Molecular sieving of common zeolites. Adapted from reference 6.

provides a dramatic example of reactant selectivity. Table 1 shows that bulky hydrocarbons which were reactive on macropore Pt/ λ l₂O₃, were almost inert on the zeolite catalyst as they were excluded from the active sites.

Table 1. Shape Selectivity. Comparison of Hydrogenation on Pt/Al₂O₃ vs. Pt/ZSM-5, from ref. 10.

Catalyst	Temp.(°C)	Pt/Al ₂ O ₃	Pt/ZSM-5
		Hydrogen	nated (%)
Bexene	275	27	90
4,4-Dimethylhex-l-ene	275	35	<1
Styrene	400	57	50
2-Methylstyrene	400	58	<2

This reactant selectivity has been illustrated by Csicsery as follows.

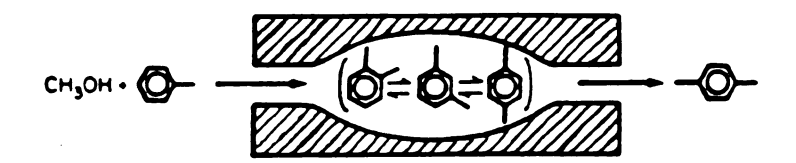


Diffusion is of paramount importance in shape selective catalysis, as one type of molecule will generally react preferentially if its diffusivity is one or two orders of magnitude greater than competing types of molecules (9). Branching has a profound effect on diffusivity, whereas increased hydrocarbon length results in a smaller diffusivity effect.

(b) Product selectivity results when the diffusion of certain products from active sites to the external surface of

the zeolites is limited.

Diffusion limited molecules may produce an equilibrium shift to less bulky molecules or can block the pores resulting in catalyst deactivation. The diffusivity of paraxylene is approximately 10³ greater than m-xylene in ZSM-5 (10). This product selectivity is illustrated below.



The selectivity can be further modified by the addition of phosphorus which may partially occlude the pores.

- (c) Restricted transition state selectivity occurs when steric constraints of the rigid zeolite pore limit the formation of bulky intermediates or transition states. The tendency for selective zeolites with small pore openings to exhibit greatly decreased coking rates probably is the result of bulky, fused ring polycyclic hydrocarbon formation being sterically prohibited in the pore confines.
- (d) Molecular traffic control can occur when more than one type of pore system exists in zeolites.

 Adsorption data from Derouane (ll) presents the possibility that reactant molecules could enter the cylindrical, zig-zag pores of ZSM-5 whereas diffusion of bulkier molecules would preferentially occur through the linear elliptical pores

(see Figure 1).

These various modes of shape selectivity make zeolites versatile and effective supports for catalytic hydrocarbon transformations.

The intracrystalline acidity of zeolite channels is another prominent feature responsible for the unusual capabilities of these materials. Acid sites are generated in zeolites by exchanging the natural cations with more polarizing ones (higher charge/radius) or with ammonium ion followed by calcination. The greatest Bronsted acidity is attained between 400 and 550°C,

but above 550°C water is expelled and primarily Lewis acid sites are formed.

$$\begin{pmatrix} 0 & si & 0 & si &$$

Bronsted acidity is responsible for the carbocation chemistry of catalytic cracking and many other hydrocarbon transformations.

Acidified zeolites have much greater activity in these reactions than amorphous alumina-silica mixtures or acid treated clays. This is due to zeolitic acid sites being in greater concentration and proximity within the pores, and more uniform in their intermediate acid strength (12,14). Further, the concentration of hydrocarbons within the pores

is typically much higher than in silica-alumina pores. Additional information on surface acidity is given in the excellent review by Corma and Wojciechowski (12) and the book by Gates, Katzer and Schuit (13).

Yet zeolites do have limitations. Although the number of different zeolites synthesized is rather large, relatively few zeolites (X, Y, ZSM-5, Mordenite, Erionite, A) have found widespread applications. This is partially due to the fact that the small pores of zeolites severely limit their application in reactions that involve reactants with molecular dimensions larger than the pore openings. The supercages of faujasitic zeolites (X and Y) represent the largest zeolite pores at about 7.5 Å. For example, heavy vacuum gas oil, which contains C_{18} - C_{25} aromatics, has limited accessibility to zeolite pores and cannot be effectively cracked to more useful hydrocarbons. Typically large molecules are cracked on zeolite exteriors which results in a substantial loss in selectivity (13).

Partially in response to this zeolite limitation there is considerable interest in microporous materials that feature more adjustable, larger pores, but also have high intracrystalline acidity similar to that of zeolites. Adjustable pores would allow more flexibility in influencing the catalytic chemistry of larger molecules. Materials with great potential in this regard, that also offer molecular constrainment and intracrystalline acidity, are layered clays.

B. Clay Minerals

1. Structure

The term clay mineral defines a large, diverse class of inorganic materials that have particles less than 2 microns in diameter. Elemental units of this member of the phyllosilicate family are silicon-oxygen tetrahedra, and aluminum-oxygen octahedra. The tetrahedra and octahedra link in various fashions to form structurally distinct members of each clay mineral class.

The mineral class of greatest interest here is smectite clays which are 2:1 layered structures containing one octahedral sheet sandwiched between two tetrahedral sheets. As formed in nature a variety of cations may be found in place of the aluminum and silicon in octahedral and tetrahedral layers of idealized clays. This results in numerous clay isomorphs. For example in montmorillonite Mg²⁺ fills some octahedral cation positions, and in beidellite Al3+ is found in tetrahedral positions. In both cases a charge deficiency results as the Mg²⁺ and Al³⁺ have lower charges than the cations normally occupying these positions. This charge deficiency results in a net negative charge on the layers that is balanced by hydrated cations between the layers. The magnitude of the layer charge significantly affects chemical and physical properties of these clays and can be used in their classification (15).

Smectites have a layer charge between the low

charged pyrophillite-talc group and the highly charged vermiculites and micas. The smectite layer charge can arise in the tetrahedral layer such as in beidellite and saponite, or in the octahedral layer as in hectorite and montmorillonite. Figure 3 illustrates the smectite framework, origin of layer charge, position of interlayer hydrated cations, and d_{001} spacing measured by x-ray diffraction. The d_{001} spacing is the sum of the layer thickness and free space between layers which is also called the gallery height.

2. Smectite Properties

The intermediate layer charge of smectites is responsible for many of their unique physical properties. Highly charged clays (e.g. micas) tightly hold interlayer cations, while low charged clays (e.g. talc) require few interlayer cations, but smectite interlayer cations can be readily exchanged by a great variety of cations. Additionally, smectite layers can be separated by multilayers of polar solvents so the layers can be swollen to accomodate large molecules. Their considerable cation exchange capabilities and swellability give these minerals their unparalled versatility for intercalation of almost any desired cation (17). Intercalation here means insertion of cation guests between the layers of host (clay). Intercalation of vermiculite, which has a relatively high layer charge, commonly yields "stuffing" of the interlayer with cations which leads to diffusion related problems in

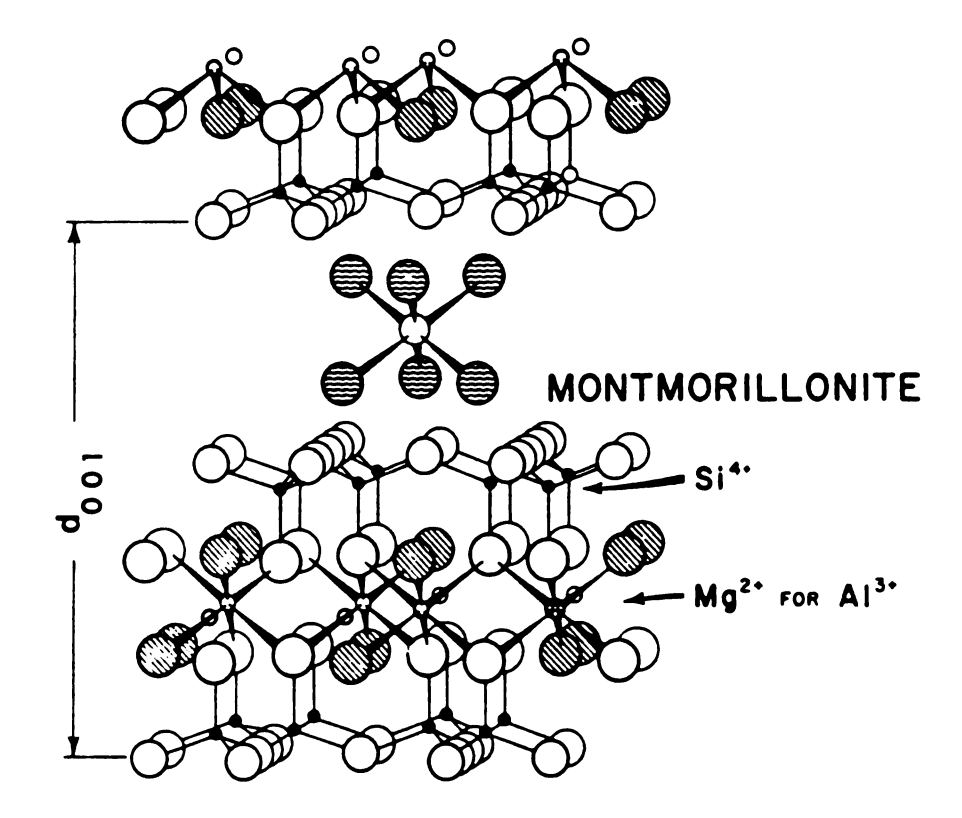


Figure 3. The framework structure of montmorillonite, a typical smectite. Adapted from ref. 16.

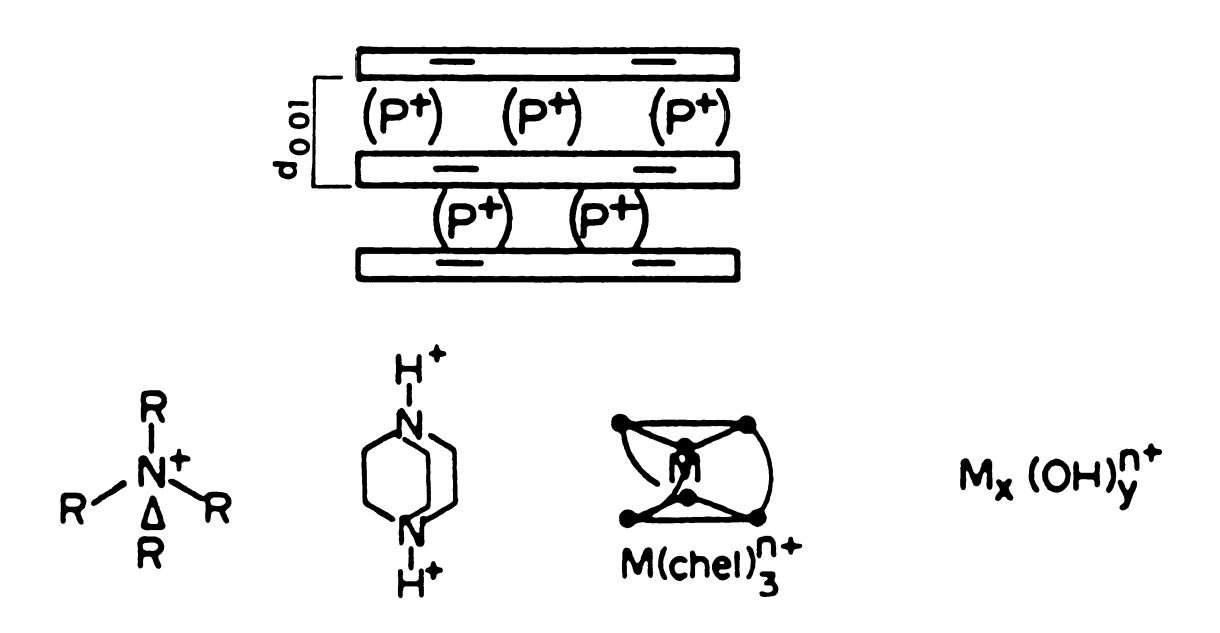


Figure 4. Schematic representation of pillared clay, along with various classes of pillars. From ref. 17.

catalysis.

3. Catalysis using Expanded Clays

The ability to swell smectites to accomodate different sized guests, intermediate cation exchange capacity, and large interlamellar surface area (750 m^2/g , theoretical), suggests that these materials should be ideal for heterogenizing homogeneous catalysts. The goal of heterogenizing a homogeneous catalyst is to combine the advantages of heterogeneous and homogeneous catalysts while minimizing their disadvantages (18-20).

Intercalation of catalytically active reactants between silicate sheets then may result in product selectivities different from those encountered in homogeneous catalysis. For example, Pinnavaia and coworkers (21) demonstrated that Rh(PPh₃)₂⁺ intercalated hectorite gave significantly improved yields of cis-alkenes in alkyne hydrogenations relative to isomerization products. This work also showed that choice of swelling solvent can dictate gallery height and influence reaction rates and selectivities relative to homogeneous catalysts. The size and shape of alkyne substrates also proved to be important, leading to the postulate that transition state size selectivity was present.

Hydrated interlayer cations are more acidic in clays than commonly found in solution (22,23) which is another important property of intercalated clays. Although

intercalated clays can exhibit both Lewis and Bronsted acidity, protonic acidity is dominant in reactions with organic substrates. Bronsted acidity originates from the polarization of water molecules coordinated to cations restricted between the clay layers, and increases with increasing cation charge to radius ratio (24,25). Further, as the interlayer water content and layer separation decrease, the cations are more confined and hence Bronsted acidity increases. The relative state of hydration and nature of interlayer cation present then greatly influences the acidity, which is important to the unusual chemical reactivities, conversions and selectivities.

Natural montmorillonites, have Hammett H_O values from 1.5 to -3 (26). Dramatic increases in acidity can be achieved by simply replacing the natural cations with protons, resulting in acidity values -5.6 and -8 (27). The surface acidities of such modified clays are comparable to that of concentrated nitric and sulfuric acids. The Bronsted acidity of these clays is the key to producing carbocations which are responsible for the transformations, rearrangements and conversions observed with organic molecules.

The versatile nature of clays in catalyzing unusual conversions of organics has been the subject of many recent reviews (28-30). Adams et al. (31) have reported the pseudocatalytic selective conversion of straight chain alk-1-enes over ion-exchanged montmorillonites to

di(2,2'-alkyl) ethers. The interlayer cations that yield the greatest acidity, Fe³⁺, Cr³⁺, and Al³⁺, also are the most reactive, but montmorillonite intercalated with Cu²⁺ gave the highest selectivity. This reaction gives unusual products in that rearrangement products characteristic of other ether syntheses are avoided. Dehydration of primary alcohols in acidic homogeneous solutions normally yields fast rearrangement of a primary carbocation to the more stable secondary carbocation. The corresponding alkene is the favored product. Yet, Ballantine et al. (32) found that primary alcohols are converted to di(alk-1-yl) ethers over exchanged montmorillonites.

For the S_N^2 reaction mechanism to prevail on protonated primary alcohols without rearrangement the reactants must be in proximity. The authors suggest that the clay gallery promotes reactant contact and the intermolecular product is preferred (ether) over the intramolecular product (alkene). Weiss (33) in fact proved that reactant pair proximity can effect catalytic conversions in clay galleries. By using a series of smectites with varying layer charge, he was able to change the distance between gallery cations which altered product selectivies in oleic acid oligomerization. Thus the acidity of and distance between interlayer cations are variable components of clay catalysts which can afford adjustable environments for unusual chemical conversions.

4. Pillared Clays

The collapse of clay layers resulting from interlayer dehydration at elevated temperatures severely limits application of these layered clays in heterogeneous catalysis. The demonstration by Barrer and McLeod (34) in 1955 that interlayer porosity could be stabilized by the intercalation of molecular props or pillars however, has led to materials that successfully circumvent this problem. These materials, called pillared clays, contain robust molecular props that hold clay layers apart at elevated temperatures so that interlayer porosity is retained (Figure 4). The adjustability of pillared clays, and the fact that their pores can be larger than zeolites, has led to renewed interest in clays as heterogeneous catalysts. This is particularly true for reactions with large molecules, such as high molecular weight crude oil.

Barrer and McLeod's early work involved the intercalation of $N(CH_3)_4^+$ and $N(C_2H_5)_4^+$. These cations provided stable intracrystalline porosity so that both nonpolar and polar molecules could be adsorbed in intralamellar regions. Selective sorption of pentanes with these clays was inversely related to their cross-sectional area, <u>i.e.</u> uptake of $C_5H_{12} > iso-C_5H_{12} > neo-C_5H_{12}$. Also uptake of O_2 increased eight-fold and C_6H_6 adsorption increased twelve-fold, compared to similarly prepared Na^+ montmorillonite. The sorption properties of a variety of methyl ammonium montmorillonites (ie. $(CH_3)_{4-x}NH_x)^+$ were studied by Barrer

and Reay (35). The found exclusion of molecules with critical dimensions greater than the gallery heights of those expanded clays, and determined that alkyl ammonium pillars were stable up to approximately 250°C.

The concept of pillared clays was further advanced with the intercalation of a large bicyclic amine called 1,4 diazabicyclo [2,2,2] octane (DABCO). Mortland and Berkheiser (36) showed the protons of diprotonated DABCO to be labile and observed conversion of acetonitrile to acetamide with DABCO-smectites. Shabtai et al. (37) demonstrated that DABCO-montmorillonite had higher catalytic activities for esterification of carboxylic acids than alkyl ammonium intercalated clays. They also demonstrated that these materials had shape selective capabilities.

The third major class of molecular props to be intercalated in smectites is the tris-metal chelates. A variety of metals and coordinating ligands have been used including Cu^{2+} and Fe^{2+} complexed with 1,10-phenanthroline (38), Fe^{2+} , Cu^{2+} , Ru^{2+} with 2,2-bipyridyl (38,39) and Cr^{3+} , Co^{3+} , Cu^{2+} , with tris-ethylenediamine (40). The ability of these materials to bind more metal complex than expected, called intersalation, follows the anion tendency to ion pair (i.e. $SO_A^{--} > Br^{--} > Cl^{--}$).

The report by Brindley and Sempels in 1977 (41) of smectites pillared with hydroxy-aluminum cations led to a new class of polynuclear metal pillared clays. The hydroxy aluminum beidellites prepared had basal spacings near 17 Å

and maintained this spacing upon calcination up to 500°C. Montmorillonites pillared with hydroxy cations of Zr (42) showed similar basal spacings (d₀₀₁), thermal stabilities and surface areas $(300-400 \text{ m}^2/\text{g})$. Nitrogen adsorption isotherms for these materials showed considerable micropore character and displayed Langmuir adsorption isotherms. Lahav et al. (43) reported the basal spacing of Al-pillared clays to be dependent on age of the hydroxy-Al solutions, OH/Al ratio, and concentration of Al solution relative to clay. Vaughan and Lussier (44) found that Al-pillared clays adsorbed 1,3,5-triethylbenzene (7.6 Å) and smaller molecules, but not 1,2,3,5-tetramethylbenzene (8 Å) or perfluorotributylamine (10.4 Å). In addition to demonstrating these molecular sieve properties, they also found that mesopores (60-150 Å diameter) were present along with the dominant micropore (<15 Å) character. Further, they suggested that gallery porosity could be optimized by controlling ion exchange capacity of the clay, degree of pillar hydrolysis, and drying conditions.

The potential of these clays for heterogeneous catalysis was demonstrated by Shabtai and Lahav (45,46) and Vaughan et al. (47,48). Pillared clays showed improved reaction rates for catalytic cracking of hydrocarbons (especially those with kinetic diameters > 9 Å) (49), and produced gasoline octane ratings in the cracking of Gas Oil comparable to zeolite catalysts (47).

A variety of cations have been used since these

initial studies of polynuclear metal pillared clays. In addition to further developments with Al (50-52), and Zr (52-54) pillars, Si (55), Bi (56), Cr (57), Ni (42), and Fe (58,59) pillars have been used to induce permanent clay porosity. Yet, the Al and Zr pillars seem to be the most thermally stable pillars found so far.

Two general synthetic routes are commonly followed for the pillaring of clays: <u>in situ</u> construction of the pillar precursor within the galleries, and exchange into the galleries of a pillar preformed in solution (60). The <u>in situ</u> method is illustrated below with a silicon acetly-acetonate (acac) pillar.

$$\frac{\text{Si(acac)}_{3}^{+} + \text{Na}^{+} \longrightarrow \overline{\text{Si(acac)}_{3}^{+}} + \text{Na}^{+}}{\text{Si(acac)}_{3}^{+} + \text{H}_{2}^{0} \longrightarrow \overline{\text{Si(OH)}_{4}^{+} + \text{H}^{+}} + 3(\text{CH}_{3}\text{CO)}_{2}\text{CH}_{2}}$$

Although this method circumvents the numerous manipulations common to the exchange method, it does not allow control of the pillar stoichiometry. Typically pillar hydrolysis continues until the interlayer is filled, producing a chloritic-type layer. This method can be used however, to form unusual pillars within the galleries such as Ta and Nb pillars (61).

Direct exchange of pillars formed in solutions into clay layers is the preferred synthetic method for heterogeneous catalyst preparation as it yields materials with high porosities. The stoichiometry of the cluster and

density of the pillar within the gallery is readily controlled with the direct method. A variety of cation pillars can be introduced this way, including a new pillar based on silsequoxides (62,63).

5. Properties of Metal-Hydroxy Pillars

Salts of metallic elements with high charge to radius ratio polarize water molecules and induce the loss of protons when dissolved. The addition of hydroxide ions will facilitate this process, and the subsequent formation of polymeric species. This process, termed olation, is depicted below.

$$\left[\left(H_{2}^{(H_{2}^{(O)})} \right)_{x-1}^{(Y-1)^{+}} \right] \xrightarrow{\left(H_{2}^{(O)} \right)} \left[\left(H_{2}^{(O)} \right)_{x-1}^{H_{2}^{(O)}} \right] \xrightarrow{y+1} \left[\left(H_{2}^{(O)} \right)_{x-1}^{H_{2$$

Elevated temperatures, longer aging times, and higher pH promote the hardening of the polymers formed through another process called oxolation.

For high surface area pillared clays it is desirable to intercalate small, yet robust, oligomers. These can be obtained if the above mentioned variables are carefully controlled. Once inside the confines of the clay galleries however, additional hydrolysis can occur, again due to the polarizing nature of the layer. Thus, once clay solutions are pillared the clay is quickly washed to remove excess electrolyte and dried. Following drying the pillared clays

are normally calcined to convert the hydroxylated pillar to the more stable oxide as shown below for alumina-pillared clays.

$$Al_{13}O_4(OH)_{24}(H_{2}O)_{12-x}^{(7-x)+} \longrightarrow ("Al_2O_3") + (7-x)H^+$$

Pillar dehydroxylation also results in the formation of Bronsted acid sites. These sites are in large part responsible for the catalytic transformations observed with pillared clays from polynuclear metal cations below 400°C. Above 400°C, the Lewis acidity of the pillars begin to play a more dominant role.

Although the acidity of pillared clays has been central in the previously described transformations of organic molecules, these materials can also be loaded with catalytically interesting metals to take advantage of the microporous nature of this unusual support. This can be demonstrated in Fischer-Tropsch chemistry, as described in the following pages.

C. Fischer-Tropsch (FT)

Progress in the catalytic synthesis of hydrocarbons from CO and H₂ began in 1902 when Sabatier and Senderens (64) found that reduced nickel catalyzed the hydrogenation of CO to methane. Later, workers at BASF showed that alcohols, aldehydes, ketones, fatty acids and assorted aliphatic hydrocarbons could be formed over alkali promoted cobalt and osmium oxides (65). Fischer and Tropsch (66,67)

went on to demonstrate the production of hydrocarbons > C₅ at one atmosphere using Fe catalysts, and greatly advanced the fundamental understanding of this reaction.

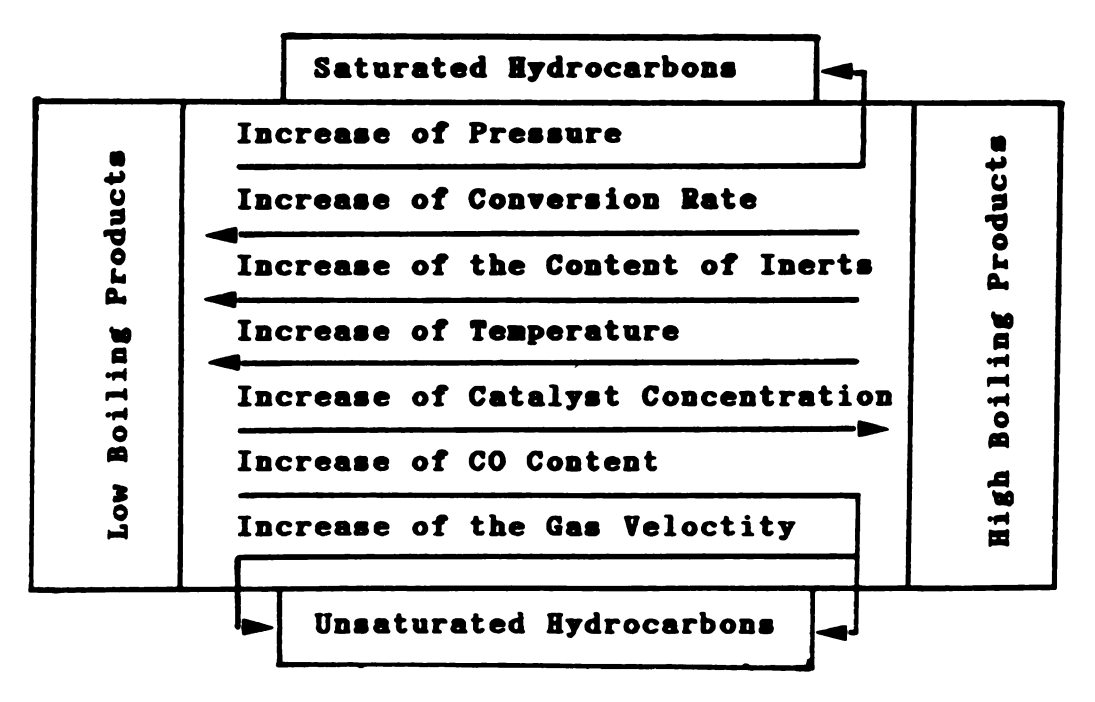
Commercialization of this process soon followed and by 1943 the ten German plants alone produced 585,000 metric tons/yr. of hydrocarbons (46% gasoline, 23% diesel, 3% lubricating oil, 28% waxes and detergents) (68). Scientific and technogical interest in FT reached a high point between 1940-1955, as reviewed in a number of important papers (69-71), before the discovery of inexpensive Middle East oil reserves caused a shift towards an oil based fuel and chemical industry. Industrial research and application of FT has been cyclic ever since, and the great upturn in oil prices in 1973 resulted in renewed research and development efforts in this area.

The wide variety of organic products formed in the catalytic hydrogenation of CO leads to a complex mixture of hydrocarbons which requires costly separations. Typically, linear paraffins, olefins and some alcohols result with relatively few branched products. In addition to the major reaction pathways, side reactions can yield less desirable products and affect activity and selectivity. These reactions are summarized in Table 2. The water gas shift reaction (rxn. 6) can be very important on some metal catalysts, as water produced in FT may react with CO forming H₂, which will shift the H₂/CO ratio in the reactor. Fischer-Tropsch involves a great number of process

Table 2. Important Synthesis Gas Reactions. Adapted from references 75,70.

			al/mol
		ΔG°	△H ₀
			-51.3
(2n + 1)H2 + nCO =	(2)	-7	-39.4
$C_{n}H_{2n+2} + nH_{2}O$			
$2nH_2 + nCO = C_nH_{2n} + nH_2O$	(3)	-8	
$2H_2 + CO = CH_2OH$	(4)	+4.5	5
$2nH_2 + nCO = C_nH_{2n+1}OH +$			
(n-1)H ₂ O	, ,	·	
$CO + H_2O = CO_2 + H_2$	(6)	-5	-9.5
$CO + H_2 = C + H_2O$			-31.9
nC = Ca	, ,		
	(8)	-20	-41.5
_	``'		
	(9)		
	$2nH_2 + nCO = C_nH_{2n} + nH_2O$ $2H_2 + CO = CH_2OH$ $2nH_2 + nCO = C_nH_{2n+1}OH + (n-1)H_2O$	$(2n + 1)H_{2} + nCO = (2)$ $C_{n}H_{2n+2} + nH_{2}O$ $2nH_{2} + nCO = C_{n}H_{2n} + nH_{2}O \qquad (3)$ $2H_{2} + CO = CH_{3}OH \qquad (4)$ $2nH_{2} + nCO = C_{n}H_{2n+1}OH + (5)$ $(n-1)H_{2}O$ $CO + H_{2}O = CO_{2} + H_{2} \qquad (6)$ $CO + H_{2} = C + H_{2}O \qquad (7)$ $nC = C_{n}$ $2CO = C + CO_{2} \qquad (8)$ $nC = C_{n}$ $xM + C = M_{x}C \qquad (9)$	$ \begin{array}{cccccccccccccccccccccccccccccccccccc$

Figure 5. Influence of Process Variables on Fischer-Tropsch.



Reproduced from reference 189.

variables that affect the product distributions obtained. Figure 5 shows a simplistic scheme that emphasizes the influence of variables on product saturation and boiling point.

The activity and relative proportions of product groups also varies considerably with catalytic metal. The specific activities of metals for the methanation of CO were determined by Vannice (72) in terms of turnover frequencies (molecules converted site⁻¹s⁻¹). Nickel, for example, has a high activity and is one of the few metals that affords close to 100% product selectivity in CO hydrogenation. Although that selectivity is for methane, methanation converts synthesis gas of low heating value (5-6 M*Joules/m³) to natural gas with heating values of 35-40 M*Joules/m³ (73).

Iron is far more efficient at producing higher hydrocarbons, including large proportions of alcohols and olefins, although elevated pressures are typically required.

Iron catalysts however, are also good catalysts for the water gas shift reaction, and exhibit a wide variety of carbides under reaction conditions (74). Cobalt catalysts on the other hand do not form carbides appreciably and give low alcohol yields.

Although ruthenium suffers the disadvantage of higher cost, it is also the most active metal for CO hydrogenation. It has the capability to be supported easily in high dispersion, and produces high molecular weight

hydrocarbons at low temperatures and pressures (76). The tendency to produce higher molecular weight hydrocarbons on these metals follows

1. Mechanisms

The mechanism of FT still a topic of considerable debate. Polemics regarding postulated reaction mechanisms abound in the literature and are summarized in several recent reviews (74, 76-78).

Many recent studies indicate that nonoxygenated intermediates play a dominant role in the mechanism. This supports the hypothesis that dissociative adsorption of CO occurs on the active metal surface. The adsorbed carbon atoms are further hydrogenated to form methylene groups, which can then propagate to form higher molecular weight products. This mechanism, known as the surface carbide mechanism (79), is shown in Figure 6A. It readily explains many aspects of FT, but fails to account for the formation of large quantities of alcohols and other oxygenates on a metal such as Fe. The mechanism proposed by Storch, Coulumbic, and Anderson (70) in fact predicts high oxygenate production by arguing for the condensation of surface oxymethylene species, as shown in Figure 6B. Finally, the CO insertion mechanism, particularly advocated by Pichler and Schulz (80), is the third mechanism recognized by many researchers, as illustrated in Figure 6C.

Figure 6. Fischer-Tropsch Reaction Mechanisms. Adapted from reference 189.

ີ	Formyl Mechanism Initiation	C	Polymerization	H C H CH3 CH3 C H3 C H3 C H3 C H3 C H3	Desorption		M (H2) adm RCH3 + H2O + M
ъ.	Hydroxy-Carbene Mechanism Initiation	M (H2) a d s M	Polymerization.	H CH3 OH CH3 OH N H20	Descrition H COH		M (H2) 4 4 B + H2 0 + M
Α.	Surface Carbide Mechanism	C C C O C C O C C O C C O C C O C C O C C O C C O C C O C C O C C O C C O C C O C C O C C O C	Polvmerization	CH2 CH2 CH3	Desorption CH2	M (HZ) ads > CH4 + M CIIR	M (H2) ada RCH3 + M

2. Nonselective Product Distributions

Widespread commercial application of the FT conversion of synthesis gas (CO and H₂) however, is severely limited by the low selectivity obtainable for a hydrocarbon fraction. Product distributions are typically broad and optimization is hindered by an interdependence among selectivities. The only commercial application of FT processes is in South Africa where the process is economical due to inexpensive coal reserves. The interdependence among product selectivities has been thoroughly discussed, using a variety of SASOL iron based catalyst studies by Dry (81).

The product distributions obtained are governed by the statistics of a linear, stepwise addition of single carbon units to the growing hydrocarbon chain. A competition is present in which hydrocarbons can continue to grow on the metal surface or undergo chain termination by desorption from the surface. Assuming that the reactivity of intermediates is independent of size and that the relative probabilities of continued C-C bond formation and product desorption remain constant, a statistical model can be derived and used to predict distributions and selectivities (70,82). This mathematical formulation is identical to that derived earlier by Flory (83) and Schulz (84) for linear polymerization processes. According to the Schulz-Flory (SF) relationship the weight fraction of product with n carbon atoms, termed W_n is

$$W_n = n \quad \alpha \quad (n-1) \quad (1-\alpha)^2 \quad (1)$$

Here α is the probability of growth. If this SF distribution is followed then a plot of $\log W_n/n$ versus n will yield a straight line with a slope of $\log \alpha$. Schulz-Flory product distributions have been a dominant feature of FT since the early experiments. Yet, the consequence of a product distribution following SF is that once process variables are fixed the entire broad, product distribution is determined. This inherent lack of product selectivity prohibits commercial utilization of FT.

3. Selective Fischer-Tropsch

In a recent review, King (85) summarized current approaches to more selective systems for the conversion of synthesis gas to fuels and chemicals. To this I would add the concept of structure sensitivity, so the areas are:

- a. Limitation by pore size
- b. Metal size dependence: structure sensitivity
- c. Bifunctional catalysts
- d. Alternative mechanisms

a. Limitation by pore size

The approach here is to confine the Fischer-Tropsch active site within a small pore and force termination of chain growth due to spatial restrictions. Production of hydrocarbons longer than the pore limits would be severely diminished in this case, and the product distribution would shift to lower molecular weight products.

A number of brief communications have shown that with zeolites (86-90), and aluminas with various pore sizes

(91,92), unusual product selectivities can occur in FT. For example, by carefully encapsulating iron in the micropores of zeolite Y (89), a catalyst was obtained that selectively produced butenes (47%) and few higher hydrocarbons (250°C). When a similar reaction was run at 300°C methane production became dominant at the expense of butene production. Further, when a catalyst prepared with large iron clusters present on the zeolite external surface was examined at 250°C, it gave a distribution that was similar to that at 300°C for the encapsulated iron. The authors suggested that the catalyst contained Fe active sites within zeolite cavities initially but higher temperatures induced migration and sintering of iron atoms which resulted in aggregates on the zeolite exterior. A similarly prepared cobalt catalyst demonstrated butene selectivity near 70%, and showed resistance to Co migration up to 260°C. In all cases hydrocarbon production decreases greatly beyond C 5.

Research with Co encapsulated A and Y zeolites showed propylene as the only detectable product, and gave 70% production of C_4 - C_7 hydrocarbons respectively (86). A Co/A sample that had been reduced with H_2 however, showed a typical product distribution (about 65% CH_4), which indicated Co migration from the zeolite cavities.

Preparation of such catalysts by heterogenizing metal cluster carbonyls has received considerable attention recently (93), as it offers zero metal oxidation states and

intimate contact between metals in the case of mixed metal complexes (94). The use of a metal carbonyl precursor also eliminates the need for a reduction step prior to catalysis, allows metal placement in zeolite micropores as many clusters are < 7Å, and permits infrared characterization of the metal cluster in situ. The elimination of the reduction step is important as metals which may have been carefully encapsulated in micropores may migrate during reduction in hydrogen.

b. Metal particle size dependence: structure sensitivity

The role of pore constraints in shaping the FT distributions however, is difficult to separate from that of the unusually small metal particle sizes present within zeolite cavities. When the small metal clusters used to introduce metals into micropore cavities are exposed to elevated reaction temperatures they decompose and can aggregate to form ensembles of metal atoms (typically 1 nanometer (nm) in diameter). As activities and selectivities of such small metal ensembles may differ from that of bulk metal, a metal size dependence seems plausible.

Based on this line of reasoning, and the non Schulz-Flory distributions mentioned above, Nijs and Jacobs (95) proposed an "Extended Schulz-Flory" model (ESF). Two assumptions are central to this ESF model: (1) a metal particle size dependence exists in FT which results from the metal particle size and geometry imposing a maximum on

the hydrocarbon chain length which can be produced, (2) on each metal particle hydrocarbon chain growth can be described by SF with the number of polymerization steps being governed by assumption (1). These assumptions imply however, that reaction mechanisms involving a one by one insertion of C_1 units into the growing M-alkyl chain must be ruled out in favor of those having flatly adsorbed alkyl chains.

To obtain theoretical product distributions based on these assumptions Nijs and Jacobs (95) used Schulz-Flory to calculate product distributions for all hydrocarbons less than the maximum hydrocarbon chain length. The weight of the hydrocarbon of maximum chain length (N) producible on the metal particle of limited dimensions is

$$W_N/N = 1 - \sum_{1}^{N-1} \alpha^{n-1} (1-\alpha)^2$$

Since the maximum length of the hydrocarbon is strictly limited by the particle size in this theory, (N) could be determined for each metal particle of diameter d by

$$d = AD_{N}$$
 (3)

where D_N is the particle diameter in terms of the carbons in C_N and A is a proportionality factor. For example, if decane would just stretch across a metal particle of diameter d (and if A were 1) D_N would be 10. A skewed Gaussian relation was used to calculate metal particle size distributions, and d values were generated by equation 3.

To test the validity of this model non-SF distributions

in the literature were numerically fit by optimizing α , along with d, and the particle distribution variance from the Gaussian curve. Figure 7 shows the reference FT distribution determined by Vanhove et al. (91) for Co/alumina compared with the product distribution generated by ESF. The DN values used for A and B were 4 and 17 respectively (α =0.89). ESF produced curves that provided a good fit with the experimentally determined non-SF distributions.

The success of ESF in fitting non-SF distributions for metals dispersed in zeolites or amorphous supports, implies that to obtain selective FT distributions very narrow metal particle size distributions, and high chain growth probabilities are required. Broad particle distributions with numerous different D_N 's would result in broad product distributions, and without a high probability of forming long chain hydrocarbons the cutoff in production of higher molecular weight products would not be detectible. One great advantage of zeolites (and perhaps pillared clays) as FT supports then may be their ability to retain narrow metal size distributions and small metal sizes, as sintering of metals could be greatly diminished in the microporous channel networks.

The distributions that ESF fit however, were from very brief communications which lacked detailed product analyses, kinetic data, or experimentally determined metal particle size distributions. More rigorous investigations of the relationship between product distributions and metal

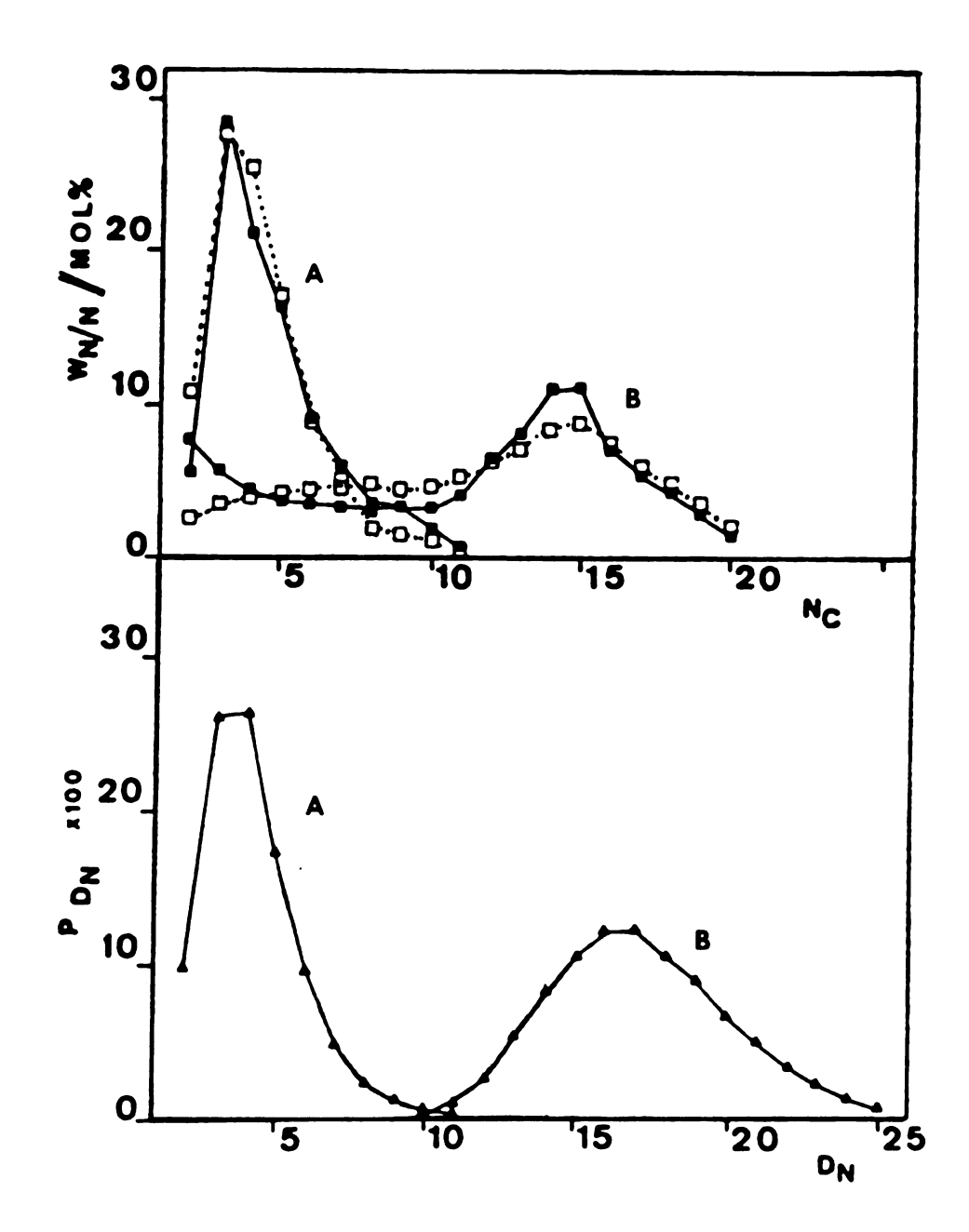


Figure 7. (a) comparison between a experimental non-Schulz-Flory distribution (open symbols, 91), with an Extended Schulz-Flory curve (closed symbols, 95). Curve (A) is from 2% Co/Al₂O₃ with mean pore radius 6.5nm, (B) 2% Co/Al₂O₃, 30nm mean pore radius. (b) particle size distribution (P_{DM}) for particle diameters used to generate the theoretical Extended Schulz-Flory plot. Reproduced from ref. 95.

particle size have not substantiated the ESF model and it has not been widely accepted. For example, Kellner and Bell (96) showed product distributions of highly dispersed Ru on alumina to be essentially invariant with Ru dispersion (inversely related to metal size).

Dependence of FT product distribution on metal size falls within the scope of structure sensitive reactions. In structure sensitive reactions the characteristics of heterogeneous catalytic reactions are affected by the surface geometry, or nature of a supported metal. As the number of atoms in the particle decreases the proportion of atoms in unusual crystallographic environments (i.e. corner atoms) should increase offering various propensities for unusual chemical reaction (97). Further, as metal particles decrease below approximately 20 A in diameter (about 500 atoms) electronic properties begin to differ from those of bulk metals (97,74,98,99). That FT is a structure sensitive reaction is suggested by its similarity to ammonia synthesis and hydrogenolysis which are known to be structure sensitive, and the probability that a relatively large site is required for the many components of chain growth (75).

c. Bifunctional catalysts

This approach involves the production of primary or low molecular weight intermediates (e.g. olefins), and their conversion to higher molecular weight products on a

second catalytic site <u>via</u> a chemistry different from FT.

Researchers at Mobil (100-102) used ZSM-5 to directly

convert alcohols and other hydrocarbon intermediates to

light hydrocarbons. The zeolite acid sites perform the

second transformation, allowing improved control over

product selectivites.

d. Alternative mechanisms

Finally, it should be noted that catalysts are available which are not limited by the non-selective mechanisms of Fischer-Tropsch. Two such processes are the use of methanol as a feedstock, and the direct conversion of synthesis gas by organometallic clusters (85).

D. Research Objectives

The diversity of cations used to permanently expand layered silicate clay minerals has increased dramatically since polycations of Al and Zr were intercalated into clay interlayers. Aluminum and zirconium pillared clays have high thermal stability and are active in the catalytic transformation of organic molecules at elevated temperatures, which has encouraged the synthesis of new robust inorganic polycation pillars. The intracrystalline acidity of these materials is a dominant feature in these catalytic reactions. Yet, their application in high temperature reactions, such as catalytic cracking, has been limited by their high coking rates and low hydrothermal stability relative to their zeolite counterparts. It has been of

particular interest then to demonstrate the catalytic potential of these materials at moderate temperatures and examine catalytic features of these materials other than the intracrystalline acidity.

The primary objective of the present work is to investigate the catalytic potential and characteristics of certain pillared clays in Fischer-Tropsch, a moderate-temperature catalytic reaction. Fischer-Tropsch requires that catalytically active metals be dispersed in the pillared clays. The first method used to disperse metals in the pillared clay galleries involves iron pillared clays, discovered by M.S. Tzou (58). The catalytic research on these iron pillared clays focuses on examination of: the activity of these pillars in Fischer-Tropsch; hydrocarbon distributions obtained; and the stability of the pillars during catalysis. The micropore location and chemical environment provided by the pillared clay for the Fischer-Tropsch active site is of particular interest as it may influence the product distributions obtained.

The second method of highly dispersing Fischer-Tropsch active metals takes advantage of the intracrystalline acidity of alumina pillared clays to protonate ruthenium carbonyl clusters within the clay galleries. This unique synthetic method, was also discovered at Michigan State University (103). We viewed this method as a means of selectively introducing a Fischer-Tropsch active site into the micropore regions of one of the most stable pillared

clays known. Ruthenium has a propensity for relatively high molecular weight hydrocarbon production in Fischer-Tropsch, and is one of the most catalytically active metals in this reaction. Another major focus of the present work then is to investigate the activity, hydrocarbon distribution, and disposition of the Fischer-Tropsch active sites formed by ruthenium cluster introduction into alumina pillared clay micropores.

CHAPTER II

Experimental Methods

A. Clay Preparation

The Wyoming montmorillonite used in the preparation of iron pillared clays was dispersed in distilled water and then centrifuged at 2000 rpm for 15 min. to remove large particles and carbonate impurities. The decantate was used in pillaring reactions. Arizona montmorillonite was used for preparation of alumina pillared clays that were to be loaded with Ru, as it contained less free iron oxides and had little constitutional iron. Before pillaring however, the Ca²⁺-montmorillonite from Apache County, Arizona (obtained from the Source Minerals Repository, 1981), was converted to the sodium exchanged form by stirring the dispersed clay in 1M NaCl overnight. The clay was then dialyzed against deionized H2O until Cl free, then sedimented 12 hrs in large graduated cylinders. All but the bottom 200 ml was removed by suction. The clay suspension was then centrifuged and the resulting solid treated with 150 ml 1N Na Acetate buffered to pH 5 by acetic acid, per 5 gram portion of clay, to remove the carbonates present naturally in this clay. The mixture was digested at 70-80°C for 3 hrs with occasional stirring with a rubber

policeman-fitted glass stir rod. The sample was transferred to a beaker, cooled, centrifuged, and washed one time with distilled $\rm H_2O$. Forty ml of 0.3N Na-citrate and 5 ml of 1N NaHCO₃ was added for each 5 g of clay remaining, and the solution was warmed to 75-80°C on a hot plate. At this point 1 g of Na₂S₂O₄ was added /5 g clay to the stirred solution and the temperature carefully kept within this range for 30 min so that free iron oxides could be removed. When the solution had cooled it was again centrifuged and washed with $\rm H_2O$. At this point the solution was dialyzed again and resedimented, before distilled water was added to bring the solution to 1 wt%.

B. Preparation of Alumina Pillared Montmorillonite (APM)

The synthetic method used to prepare the alumina pillared clays used in this work was similar to that discussed by Landau (104). The pillaring reagent used here was 50 % w/w chlorhydrol solution obtained from Reheis Chemical Company. The amount of chlorhydrol solution required for a given synthesis was weighed (2.6 g chlorhydrol/ g clay) and diluted immediately prior to the pillaring reaction (50 ml of distilled water/ g clay). The resulting solution (0.23M in Al) was added slowly to a rapidly stirred 1 wt% clay solution (15.5 mmol chlorhydrol/ mmol clay). The solution was stirred for 2 hrs following completion of chlorhydrol addition, and then the product was washed and centrifuged repeatedly with deionized water to remove excess electrolyte. The alumina pillared clays with the highest basal

spacings and surface areas were obtained by carefully minimizing the time that the pillared material was exposed to large quantities of water. After the first centrifugation of pillared clay solution the mother liquid was decanted and additional clay suspension was added to the original centrifuge tubes without redispersal of the clav. This process was continued until all of the original clay suspension was centrifuged. The clay was transferred to an Erlenmever flask with a minimum amount of distilled water and any clay clumps were broken up by repeated shaking of the stoppered flask. The amount of water required to fill the centrifuge tubes was then added and the resulting solution was shaken vigorously before the nonstop process of centrifuging and washing was continued. The flocculated, pillared clay obtained after 10-11 washings was air dried on glass sheets in an area of good ventilation. material was scraped from the glass soon after drying was complete and calcined for 3 hrs at 350°C under vacuum.

C. Immobilization of Ruthenium Carbonyl on APM

The alumina pillared montmorillonite (APM) was reactivated at 350° C for 4 hrs in vacuum in preparation for ruthenium cluster immobilization. Ru₃(CO)₁₂ was added to the cooled, activated clay (13 mg Ru₃(CO)₁₂/ 0.5 g clay) using appropriate techniques for air/water sensitive compounds. Methylene chloride was then added and the solution was stirred for 16-20 hrs according to the method of

Giannelis (104). The solution was then transferred to a glove box for filtration and carefully washed to remove excess ruthenium cluster, as physically bound clusters would decompose and enhance Ru sintering during catalysis. The green powder obtained was kept dessicated until used in initial experiments, but as the material eventually changed so that it was not catalytically active (about 2-3 months), the material was later stored in the glove box and small portions were removed for various studies.

D. Catalysis

Iron pillared clays were characterized for Fischer-Tropsch catalysis in a 304 stainless steel (s.s.) fixed bed flow reactor having a 7 mm inside diameter (Figure 8). Gas flows were regulated using a Brooks model 5890 mass flow controller. Approximately 0.3 g of Fe/PILC catalyst was mixed with enough low surface area & -Al2O2 diluent (Norton Chemicals, 10-14 mesh) to make a bed height of 7 cm. The catalyst was held in the middle of the reactor tube by plugs of glass wool. A 304 s.s. thermocouple (Omega) was placed in the middle of the bed so that the oven temperature could be regulated by a Eurotherm model 990 temperature controller. Catalysts were dried in He flow at a gas hourly space velocity (GHSV) of 300 hr -1 (V/V/hr, 35 ml/min) for 18 hours. They were then cooled to 25°C, the gas was changed to H2 and the GHSV was increased to 428 hr 1 before reduction in hydrogen began (200°C, 30 min; 400°C, 16 hrs). After the reactor had cooled, the flow gas was

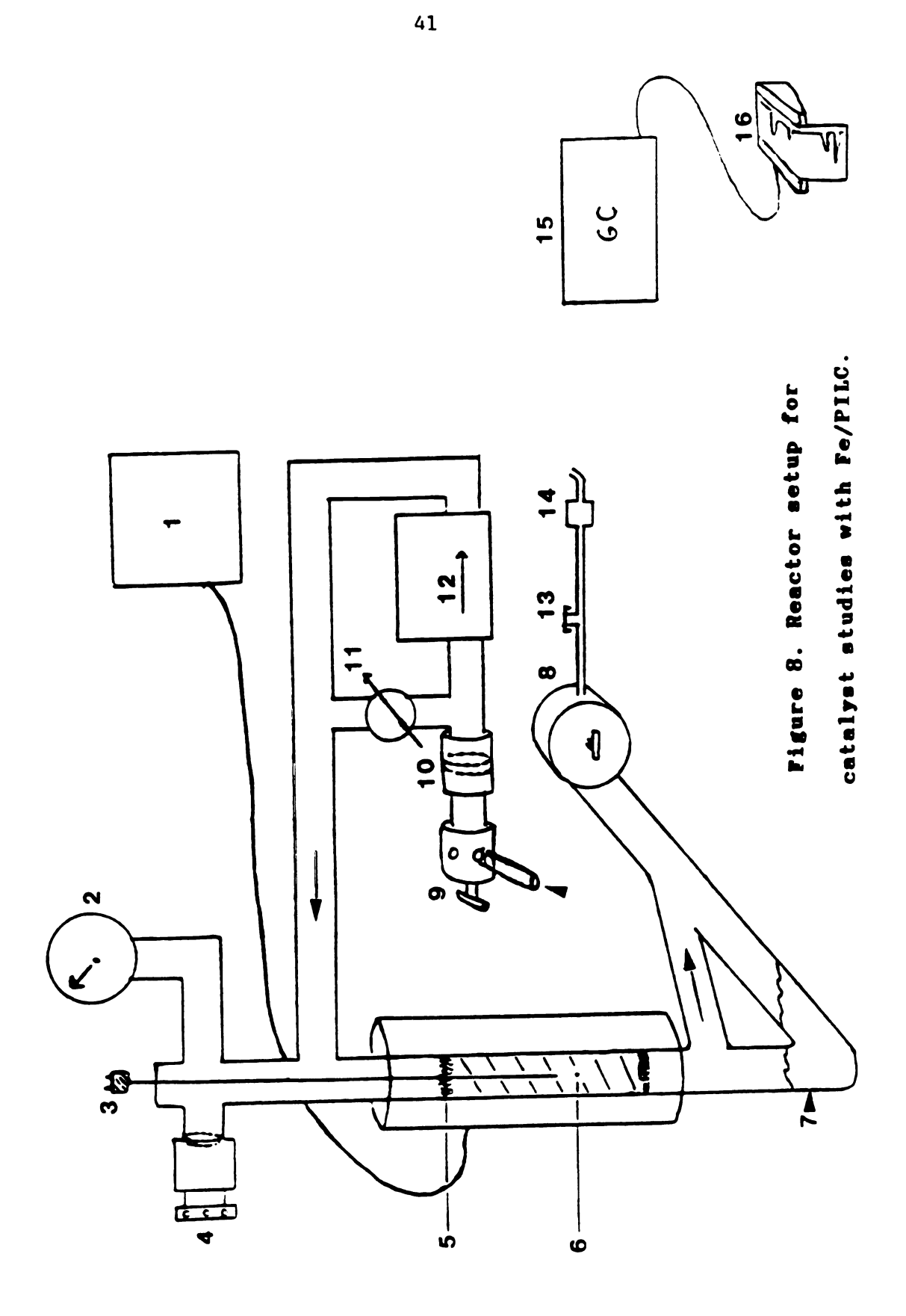


Figure 8 Key.

1.	1. furnace temperature controller	6	9. four port valve /gas selection
2	2. pressure gauge	10.	10. 0.5 micron filter
8	3. thermocouple	11.	11. bypass valve
4	4. blowout valve	12.	12. mass flow controller
5.	5. glass wool plug	13.	13. gas sampling valve
9	catalyst bed	14.	14. gas bubbler
7.	condensible products trap	15.	15. gas chromatograph
œ.	8. backpressure regulator	16.	16. recorder

switched to a premixed feed gas (Air Products, $H_2/CO = 2$), the GHSV was lowered to 300 hr⁻¹, and temperature and pressure were increased to $275^{\circ}C$ and 120 psi. Condensable liquids were trapped in the elbow of a steel vessel cooled to $-78^{\circ}C$ ($CO_2(s)/Acetone$). Gaseous fractions were sampled using a valved gas tight syringe (Supelco). Reactor connections were made using Swagelok fittings.

Hydrocarbon fractions were analyzed on a F and M Scientific model 402 by flame ionization, fitted with a 5' \times 1/8" stainless steel Poropak Q (Waters Assoc.) column.

Permanent gases were detected by thermal conductivity on a Varian model 920 GC with 6' x 1/8" s.s. Carbosieve S-II (Supelco) column. Alkane and alkene standards (in He) from Scott Specialty Gases were used for GC calibration.

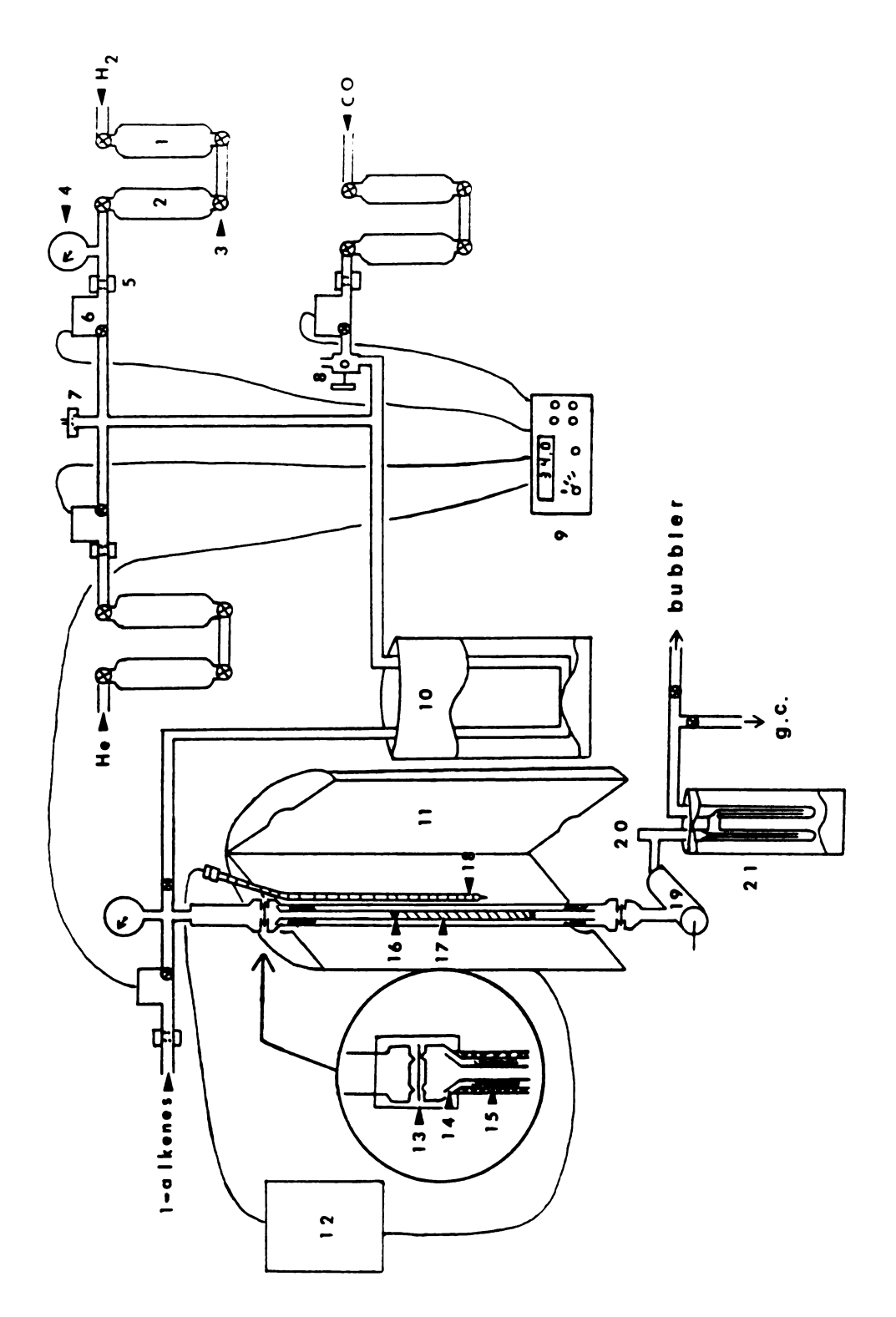
Three major changes were made to this system for the catalytic characterization of ruthenium loaded alumina pillared montmorillonite (Ru/APM). In response to the low conversions of Ru/APM at 18-20 psi, and sensitivity to feed gas impurities (Appendix B), all technical grade gases were purified by passage through a trap filled with 5Å molecular sieve and cooled to -72°C (CO₂(s)/EtOH). Second, the reactor described above was replaced with a 7 mm i.d. quartz tube fitted with a glass to metal transition and flexible s.s. tubing. The catalyst was placed atop a quartz frit in the middle of the glass tube and catalyst and diluent loadings were as above.

The elbow collection vessel used above was removed for

these studies at 18-20 psi and gaseous products were sampled just below the reactor by syringe at a sampling port. Condensable products were trapped at -72°C immediately following the heated back pressure regulator. The molecular sieve trap effectively eliminated the formation of a mirror, caused by impurity decomposition products inside the quartz reactor.

Finally, the hydrocarbons were analyzed on a Hewlett Packard 5890 GC, fitted with a 0.250 um x 60 m SPB-1 capillary column with 0.25 um film thickness (Supelco), by flame ionization. This GC was also equipped with a thermal conductivity detector, and permanent gases were sampled by an in line GC switching valve and separated on the Carbosieve S-II column.

The catalytic characterization of Ru/APM at elevated pressures, required a redesign of the reactor system and complete removal of background activity from the reactor. The redesigned system is sketched in Figure 9. In this system ultrahigh purity CO (99.9%), H₂(99.999%) and He (99.999%) obtained from Matheson were further purified over a Mn/SiO₂ catalyst (synthetic procedure, Appendix C), that reportedly removed O₂ to less than 1 ppb (105) and serves as its own indicator due to a green to black color change with oxidation. The CO purchased was contained in an aluminum cylinder. Each gas was then passed through a 5 Å molecular sieve for H₂O removal. These purifications were accomplished in 1 liter 316 s.s. vessels that acted as



Reactor system for catalytic characterization of Ru/APM. Figure 9.

Figure 9. Key

12. furnace temperature controller	13. VCR glands, teflon gasket	14. quartz insert	15. teflon tape	16. silanized glass wool	17. catalyst bed	18. thermocouple	19. heated backpressure regulator	. heated sampling port	. condensible products trap
12	13	14	15	16	17	18	18	20.	21.
l. oxygen scrubber	2. moisture scrubber	3. regulating valve	4. pressure gauge	5. 0.5 micron filter	6. mass flow controller	7. rupture disk/ blowout valve	8. ball valve	mass flow controller interface module	10. cold trap (-72°C) filled with Al203
1.	2	ъ.	4	5	6	7.	œ	6	10.

reservoirs for purified gas. Purified gas flows were controlled by Porter Instruments mass flow controllers and a CM-4 control module. Before entering the reactor, gases were additionally passed through a cold trap filled with the low surface area alumina mentioned earlier at -72°C. The reactor tube itself consisted of a 4 mm I.D. quartz insert that was wrapped with teflon tape to make a light seal with its 316 s.s. retainer. The entire reactor tube was attached to the reactor system using teflon gaskets and VCR fittings obtained from Cajon Ru/APM catalysts were placed atop a short plug of silanized glass wool that sat on a quartz frit in the reactor insert, and held in place by another glass wool plug. Typically 0.350 g of Ru/APM catalyst was loaded in the insert, giving bed heights near 45 mm, and Al₂O₃ dilutents were not used. This reactor system was used for all catalytic characterizations of Ru/APM other than that shown in Table 8.

Although pretreatment conditions were varied (Chapter IV), all catalysts were dried in H_2 at low temperatures (100°C) before catalysis. Prereduced catalysts were loaded and reduced at 1 atm in H_2 as the temperature was slowly increased stepwise to the maximum reduction temperature (400°C). Catalysts were then cooled to the desired reaction temperature in H_2 , and then the pressure was increased (if desired) using the back pressure regulator. CO flow and pressure were equilibrated to the values required for catalytic study and then added to the reactor by use of a

ball valve (Figure 9).

E. Electron Microscopy

Preparation of specimens for Scanning Electron Microscopy (SEM) utilized short segments of wood applicator sticks, that had been flattened on one side and adhered to the surface of a SEM stub. Clay particles that had been air dried on glass and removed by scraping with a razor blade, were wedged between these two wood pieces. A thick liquid agent (Tube Coat) was applied around the base and exterior of the clay and atop the wood segments to enhance conduction and eliminate sample charging in the SEM. A light coat of gold was evaporated onto all surfaces using a sputter coater. SEM was done on a JEOL JSM35-C that had a Kevex Energy Dispersive X-ray (EDS) detector and Tracor Northern digital beam control. EDS spectra linescans were obtained by doing a computer controlled scan of the electron beam across the sample.

Suitable specimens for transmission electron microscopy (TEM) were obtained by subjecting the catalyst to sonification in isopropyl alcohol for 5 min. The suspension then was allowed to settle for 3 min and the upper portion of the suspension was withdrawn. Holey carbon films (186) mounted on copper grids were dipped 3-5 times in this portion, which yielded numerous thin clay particles trapped on the grid. The Philips 300 TEM, and the SEM mentioned above, are located at The Center for Electron Optics at Michigan State University.

Post catalysis Ru/APM specimens for scanning transmission electron microscopy (STEM) were prepared in a fashion similar to TEM samples.

Most of the results for Ru/APM were obtained on a Vacuum Generators Ltd. HB501 STEM equipped with fieldemission gun, Link Systems spectrometer for x-ray microanalysis (atomic number 11 and higher), electron spectrometer, annular dark field detector, and liquid nitrogen The instrument is part of the MSU HREM facility. On the basis of the virtual objective aperture size and condenser lens currents used for our studies an electron probe diameter of 1-2 nm and a beam current of 1-3 nanoamps are expected. X-ray microanalysis was performed using collection times of 100 seconds. Count rates were low when the sample was mounted on a fixed stage, but the use of a tilting specimen holder inclined 20° from horizontal towards the detector greatly improved the counting statistics. EDS analysis was limited to thin areas of the specimens, so that corrections for atomic number, x-ray absorption or fluorescence were not required.

The method of combining the inelastic electron signal for electrons with small energy losses (those deflected through small angles, bright field detector) with the elastic signal for electrons with large energy losses (large angle deflection, dark field detector) was also employed for Ru/APM STEM studies. The procedure applied in this work for this technique, called Z-contrast imaging, was

similar to that described by Treacy et al. (168). The inelastic signal (for energy losses 15 eV<\December E<30 eV) was electronically combined with the elastic signal (50 um objective aperture used) to minimize the contribution of atomic scattering of APM in the dark field image. By subtracting the inelastic signal from the elastic signal, or taking the ratio of these signals, the contribution of the heavier ruthenium microcrystallites in the image could thus be enhanced relative to the clay support.

F. Physical Measurements

Surface area measurements for iron pillared clays were determined on a Perkin-Elmer-Shell model 212 sorbtometer. Alumina pillared clays were characterized for surface area on a Quantachrome Jr. sorptometer. Measurements on both sorptometers was done at -196°C using nitrogen as a sorbate and helium as a carrier gas. The gases used with the Quantachrome were ultrahigh purity (Matheson, 99.999%) whereas the 212 used technical grade gases purified with a liquid nitrogen trap. Samples were outgassed at 350°C under flowing Ar for 2 hrs with Fe/PILC, but outgassed at 350°C under vacuum for APM measurements. In both cases measurements were taken at three partial pressures of nitrogen and surface areas calculated by the BET theory (187).

The Quantachrome Jr. was also used to determine desorption isotherms from which pore size distributions of APM could be calculated. The values of P/Po (0.98 to 0.05)

were obtained by varying the ratios of flow rates of He and N_2 using a linear mass flow controller system purchased from Quantachrome. The calculations used were those found in the Quantachrome Jr. manual which follow the method described in greater detail by Lowell and Shields (188).

A Philips x-ray diffractometer (Ni filtered CuK) was used to determine the d_{001} reflections of pillared clays. Samples were prepared by air drying 1 ml of 1 wt% clay suspension on a glass slide. The slide was then calcined along with the bulk pillared clay for 3 hours. Iron pillared clay samples were calcined in air whereas APM was calcined in a vacuum (about 10^{-2} torr).

Adsorption of organic molecules was studied using a McBain balance equipped with quartz glass springs. Samples were activated at 350°C under dynamic vacuum for 2 hrs prior to measurements.

Infrared spectra were recorded on a Perkin-Elmer model 475 grating spectrophotometer by mixing the samples with mineral oil and placing between CsI disks.

G. Chemical Analysis

Elemental analysis of iron pillared clays was carried out at the Department of Toxicology Department (inorganic laboratory) at Michigan State, using a Jarrel-Ash 995 Atom-Comp analyzer. J.T. Baker instra-grade Si, Al, Fe, Mg and Na were used as instrument standards and NBS clay 98a served as a clay standard. Clay samples (0.05 g) were fused with lithium borate (0.3 g Gold label, Aldrich) for

2 min at 1000° C and the resulting glass quickly dissolved in 3% $HNO_3(30 \text{ ml})$, before being diluted to 100 ml with deionized water.

Ru/APM samples were sent to Galbraith Analytical Laboratory, Inc. (Knoxville, TN) for Ru analysis.

Chapter III

Iron-Pillared Clays

A. Introduction

Iron has been one of the principal components in innumerable FT catalysts, yet iron alone supported by a substantial number of carriers has been very ineffective in FT (106). Highly dispersed iron supported by oxides such as Al₂O₃, SiO₂ and MgO is very difficult to reduce to Fe⁰ due to strong metal support interactions. If these interactions are diminished reduction to Fe⁰ can be accomplished, but metal crystallites are obtained due to migration and agglomeration. This results in ineffective use of metal atoms for catalysis and loss of the potentially useful properties of small metal sites, mentioned in chapter I. Optimum iron-support interactions that result in small, yet stable, zero-valent iron atoms have been elusive for the most part. Additionally, when iron is supported by SiO₂ and Al₂O₃ the iron oxide can migrate even before reduction, and metal crystallites continue to grow after formation (106).

Brenner and Hucul (107) however, were able to obtain high iron dispersions below 300°C on alumina using various iron carbonyls. Temperature-programmed desorption studies

suggested that different catalytic properties might be achievable from clusters of different nuclearity. Hughes et al. (108) impregnated magnesia and alumina with iron carbonyls in pentane and found that small iron metal and oxide particles produced large yields of ethylene and propene initially, but normal hydrocarbon production was found within a few hours. Iron agglomeration may account for the change in selectivity. Lung et al. (109) also achieved success in highly dispersing Fe by using a variety of carbon based supports that offered easily reducible Fe³⁺. Carbon monoxide turnover numbers were eight times higher with these catalysts than Fe/Al₂O₃.

Efforts to extend the family of hydroxy-metal pillared clays by M.S. Tzou (58) may be of particular interest in highly dispersing iron. It was shown that smectites could be pillared with hydroxy-iron polymers. These microporous, expanded clays had basal spacings as high as 30 Å, relatively high surface areas, and thermal stabilities near 500°C. It occurred to us that if a thin outer sheath of the pillars could be reduced, small Fe sites could be generated within the clay galleries that may be active in FT. These active sites would be unique among FT active sites as they would be very small and confined within microporous cavities. The demonstration that pillars could be catalytically active would also be unusual as catalytic transformations involving pilared clays typically result from intracrystalline acidity.

Hydrolysis Chemistry of Fe(III)

The hydrolysis chemistry of Fe(III), used by Tzou for Fe-pillar formation, has been the subject of a great number of investigations due to its widespread technological importance. The knowledge obtained in these studies is the subject of comprehensive reviews (110,111), so only the salient features will be presented here.

The initial species formed due to increased acidity of water coordinated to metal ions and subsequent hydrolysis, are low molecular weight products. The addition of base, or elevated temperatures, induces color changes in Fe(III) solutions from yellow to orange to deep brown, which are indicative of continuing hydrolysis through the general reactions of olation and oxolation mentioned in chapter I. Early studies by Spiro et al. (113) indicated that polymers were formed with continued hydrolysis, and that the polymer fraction in fresh Fe(III) solutions increased linearly with OH/Fe ratio. The molecular weight of the polymer was found to remain relatively constant in the OH/Fe range of 0.5 to 2.0, but increases considerably when the ratio was raised further. Murphy et al. (114-117) showed that discrete, spherical polyoxocations were formed initially in the OH/Fe range mentioned above. discrete spheres, observed by electron microscopy, were 1.5-3.0 Å in diameter. With time spheres linked together to form rods containing 2-6 spheres, then coalesced forming rods 200 x 30A, which eventually aggregated into rafts of

rods. These investigators reanalyzed the earlier work of Spiro et al. (113) and calculated the molecular weight of these spheres to be near 10^5 . Assuming Fe(OH)_{2.5} as a monomer formula Flynn (111) calculated that the spheres contain roughly 100 iron atoms. This process of polymer growth, coalescence, and aggregation is shown in Figure 10. The initial stages of polymerization represented by spheres and rods are however very far from thermodynamic equilibrium, and hydrolysis can continue for months or years until final forms such as goethite (α -FeO(OH)) are formed. Polymerization is accelerated by increasing parameters such as: temperature (118), Fe(III) concentration, pH, ionic strength (114), and by changing the anion (117). With chloride ion, agglomeration of spheres was fast and rods were formed after 3-4 hours. However, electron microscopy showed only spheres at comparable aging times for nitrate or perchlorate salts (114-117). Agglomeration of the rods to rafts however, was slower with chloride salts. Thermodynamic data for the formation of potential precipitates are given in Table 3.

2. Iron Pillared Clays

The high basal spacings (> 18Å) for the iron pillared clays synthesized by Tzou (58) were significantly larger than those previously obtained for iron(III) smectite intercalants (119). Tzou studied the effect of OH/Fe, aging time, temperature and iron counter anion on iron

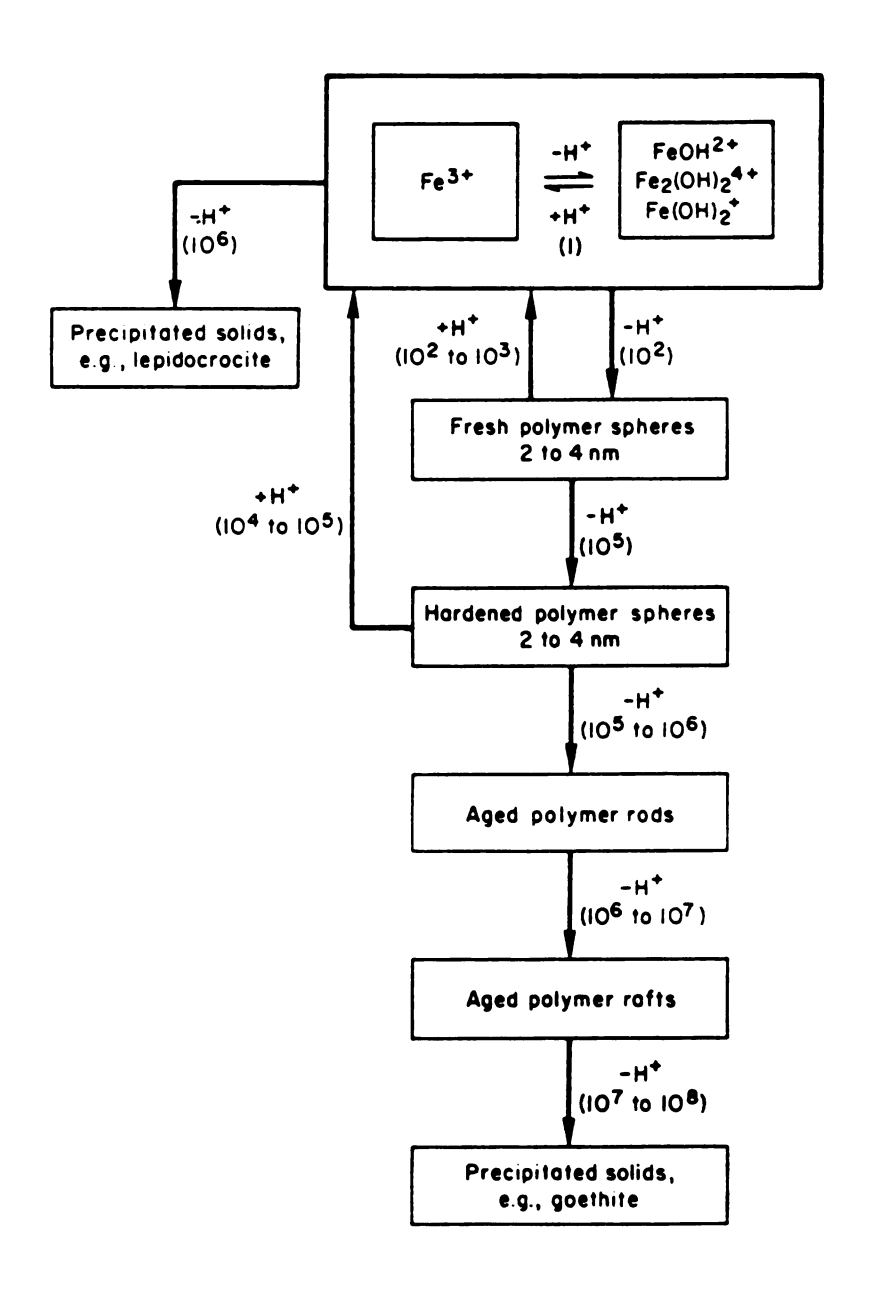


Figure 10. Iron(III) hydrolysis and polymerization, as shown by Flynn (111). The numbers in parenthesis refer to relative reaction rates.

Table 3. Solubility Products of Fe(III) Oxides. Adapted from 111, 25°C, Zero Ionic Strength.

 $1/2 \text{ Fe}_2 O_{3(5)} + 3/2 \text{ H}_2 O \rightleftharpoons \text{Fe}^{3+} + 30 \text{H}^{-}$ $\text{FeO}(OH)_{(5)} + \text{H}_2 O \rightleftharpoons \text{Fe}^{3+} + 30 \text{H}^{-}$

	solid phase	-logKs
(1/2)	α -Fe ₂ O ₃ (hematite)	41.7
	FeO(OH) (goethite)	41.7
	"Fe(OH)3" amorphous	37.1-39

Adapted from Flynn (111), 25°C, zero ionic strength.

Table 4. Sorption of Probe Molecules on Fe/PILC.

_ Tz	ou(58)		Yamanaka (et al.	(59)
Probe <u>Molecule</u>	K.D.	Amt. Ads.	Probe Molecule	K.D.	Amt. Ads.
benzene neopentane 1,3,5 TKB PFTBA	5.8 6.2 9.2 10.2	2.6 1.7 1.2	benzene p-xylene mesitylene	5.8 7.3 8.4	4.6 3.2 2.4

^{1,3,5} TEB = 1,3,5-triethylbenzene PFTBA = perfluorotributylamine

K.D. = kinetic diameter (Å)

Amt. Ads. = amount adsorbed (mmol/g) at 25°C

pillared clay formation.

In a series of syntheses with various OH/Fe ratios $(0.2 \text{M FeCl}_3 \text{ and Fe}(\text{NO}_3)_3)$ the basal spacing of the airdried Fe-pillared clay (Fe/PILC) increased steadily in the range OH/Fe=0.0 to 2.0. At OH/Fe=0 the d_{001} was only 12.3Å indicating the intercalation of only the small, low molecular weight species. With OH/Fe=1.0 a material was found with d_{001} =23.5Å and at OH/Fe=2 the Fe/PILC exhibited a d_{001} =24.8Å. With OH/Fe=2.5 however, interstratified clays were obtained. Pillaring using solutions with OH/Fe from 1.0 to 2.0 then allows intercalation of iron-polycation spheres that are similar to the dimensions found in the previously mentioned studies on Fe(III) hydrolysis chemistry.

When smectites were pillared with FeCl₃ solutions that had aged for various times it was found that basal spacings increased with longer aging times. This corresponded with decreased pH values of the pillaring solutions with time. Although basal spacings increased from 27.2Å for clays pil lared with solutions aged 3 hrs to 29.5Å for solutions aged 7 days, surface areas decreased from 351 to 270 m²/g, respectively. Elemental analysis showed the iron content per unit cell increased from 6.8 to 8.8 Fe/cell for these same clays. As Fe-polycations grow they decrease in overall charge and the intercalation of more polycations to balance the layer charge, is consistent with these trends. The steady increase in basal spacing with time could be

attributable to a higher proportion of the larger spheres seen by EM being intercalated. With aging times greater than a day rafts and perhaps bundles of polymer rods are intercalated which would dramatically decrease interlayer surface areas.

The dependence of Fe-polycation formation on counter anion was also examined with respect to the ability to prepare Fe/PILCs. Although the chloride, perchlorate and nitrate salts gave similar, well-expanded clays, sulfate solutions gave low basal spacings. This was in accordance with anion penetration arguments which explain that sulfate competes favorably with hydroxide for iron centers. This inhibits Fe-polycation formation in the case of sulfate Fe(III) solutions.

The Fe/PILCs prepared by Tzou retained high basal spacings (>20Å) up to near 500° C in air, decreasing from their original spacings by only 1-2 Å. Additionally, these materials had fairly large micropores as they absorbed 1.2 millimole/g 1,3,5-triethylbenzene (9.2Å) and 0.96 millimole/gram of perfluorotributyl-amine (10.4Å).

Recently, Yamanaka et al. (59) synthesized an iron-pillared clay by the intercalation of acetato-hydroxo iron (III) nitrate in montmorillonite. Subsequent calcination of this material yields iron oxide pillars in the galleries which yield a product with a 16.7\AA basal spacing and surface area of $300 \text{ m}^2/\text{g}$ at 500°C . As elemental analyses showed the mole ratio of acetyl: Fe in the materials to be

less than that expected, based on stoichiometry, they suggested that the acetate complex was intercalated in partially hydrolyzed forms. If this is so, the gallery may be filled with hydrolyzed iron species as is the case for <u>in</u> situ hydrolysis preparation methods discussed in chapter I. Yet, the large surface area and high sorption capacities of this material suggests that it is guite porous.

The nature of the pillaring reagent used by Tzou (58). Yamanaka (59), and Oades (120) is considerably different. The work reported here, and that of Tzou, involves the intercalation of freshly formed or hardened polycation spheres (and sometimes rods) based on the terminology of Figure 10. The population of polycation sizes intercalated, and the gallery height obtained, depends on the set of conditions chosen (pH, OH/Fe, age, etc.), which determines the extent of Fe(III) hydrolysis. Polycations in the initial hydrolysis stages gave the best combination of gallery height, and surface area. Even though acetatoiron complexes were intercalated by ion-exchange in the work of Yamanaka et al. (59), after the Fe/clay complex was held in suspension for 3 hours partially hydrolyzed forms were intercalated also. As mentioned the lack of control over pillar hydrolysis and chloritic interlayer formation are drawbacks of this method.

Oades (120) hydrolyzed Fe(III) nitrate solutions and used NaOH to promote polycation formation. The addition of such a strong base however encourages precipitation of the

iron salt. He used solutions of this salt aged 2 to 4 days at room temperature that were filtered before being added to clay solutions. His solutions undoubtedly contained substantially more higher molecular weight polycations than used by Tzou. Also, he simply added the polycations to clays without washings and low gallery heights were obtained for the iron clays (10.3 Å) and Al-clays (14.7 Å) after heating to 150°C.

The basal spacing between 25 and 29Å found by Tzou are much larger than those found by Yamanaka et al. Tzou's materials had lower sorption capacities for large organic molecules (Table 4), and thus may have more micropore character.

B. Synthesis and Physical Properties

A synthetic procedure similar to that of Tzou (58) was followed in this work to obtain smectite clays pillared with polynuclear iron oligomers. Although both the nitrate and chloride iron salts were used here, clays pillared with iron chloride gave sharper XRD patterns (indicating more well ordered materials) and were the preferred pillar precursor. Although detailed synthetic procedures are covered in chapter II, it is important to point out that the iron to clay ratio in this work was nearly half that used by Tzou (30mmol Fe³⁺/milliequivalent of clay vs. 70).

The washing procedure used proved to be crucial in the synthesis of a well-ordered iron-pillared clay. Several processes may occur simultaneously during the washing

process including: alteration of pH, change in the charge upon the clay layers, continued pillar hydrolysis and growth, and removal of excess iron oligomer. Washing the pillared clay with deionized H2O steadily increased the pH of the clay as illustrated in Figure 11A. An increase in pH can influence the net charge on the clay surfaces and the extent of hydrolysis (and charge) of surface bound cations (120). This is turn affects the balance between attractive and repulsive forces of clay sheets and determines whether individual clay platelets are dispersed or aggregated together (flocculation) in clumps or tactoids. X-ray diffraction patterns taken of the Fe/PILC after each wash revealed a well-ordered, pillared clay with high gallery heights $(d_{001} > 14\text{\AA})$ only after the ninth washing (Fig 11B), which is also the point at which flocculation occurred. Additional washings resulted in further increases in layer ordering as shown by the sharper XRD reflections. Attempts to bypass the laborious washings by raising the pH to the point of flocculation with addition of solid Na₂CO₃ after a few washings, gave a Fe/PILC that indeed was pillared but not well-ordered. After two or three washings the pH altered Fe/PILC appeared just as well-ordered as control Fe/PILCs having the same number of washings.

The pH increase through washings, or Na_2CO_3 addition, may result in a substantially increased degree of pillar hydrolysis and growth within the clay galleries. If

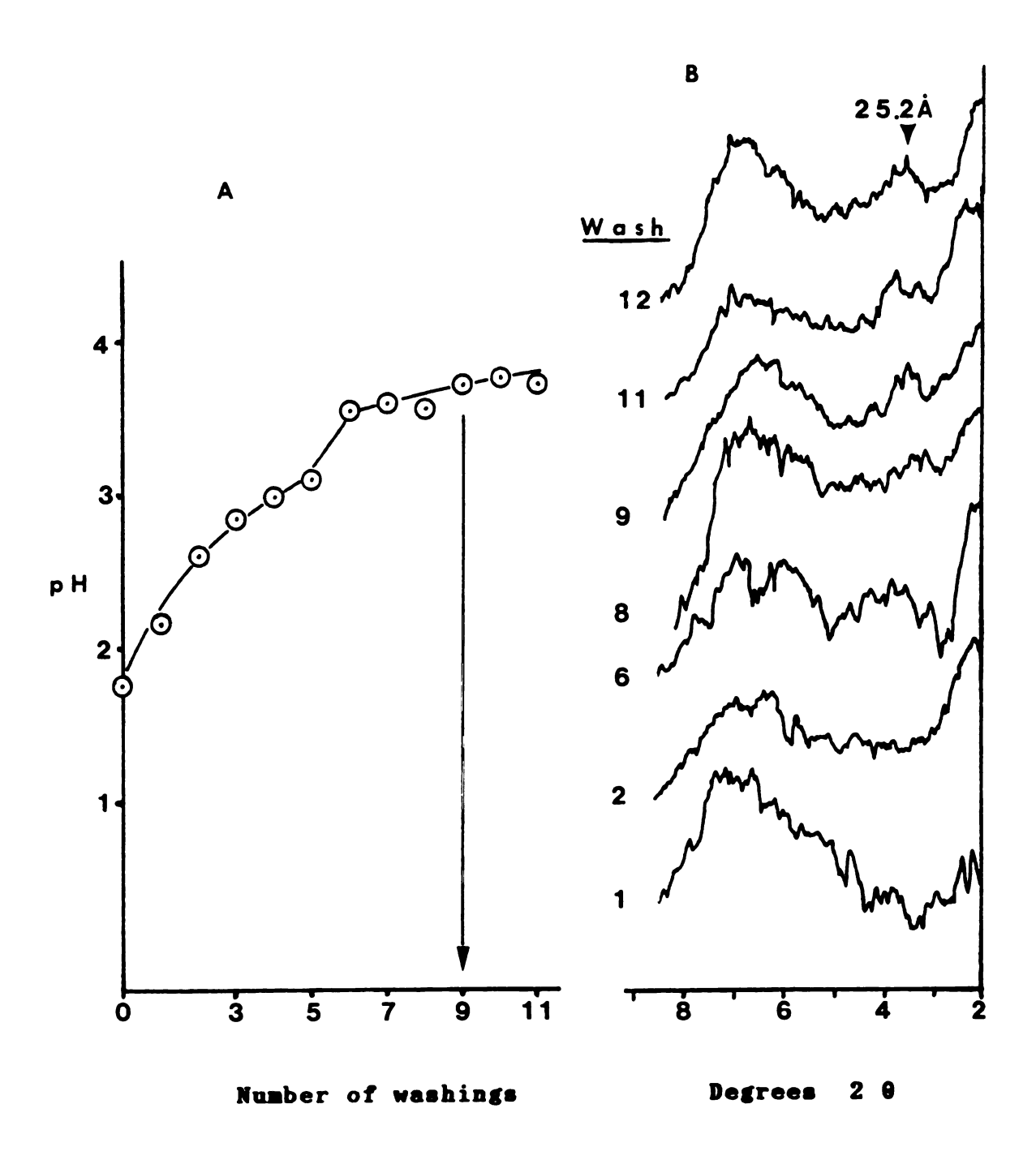


Figure 11. Change in the pH of Fe/PILC sols during the process of washing (A), and XRD patterns (B) of air dried Fe/PILC films after selected washings. The arrow in (A) indicates the pH and washing at which flocculation first occurred.

uncontrolled, this may result in a chloritic interlayer similar to the in situ pillar preparation method. When a portion of the Fe/PILC washed twelve times was dialyzed against deionized water for one week the material showed a broad hump at 14.2 A confirming chloritic interlayer formation. Other experiments using dialysis of Fe/PILC at various stages in the washing process showed that dialysis did not lead to flocculation, perhaps because iron-oligomers could not pass through the dialysis membrane. Due to the relatively facile hydrolysis of Fe/PILC, washings were done as quickly and as continuously as possible. The nonequilibrium state of intercalated Fe-polycations also must be considered when deciding on the method of PILC drying.

Oades (120) has demonstrated that the amount of metalpolycation adsorbed on a clay can dramatically affect the
clay surface charge and the point at which flocculation
occurs. Thus, the removal of excess oligomer during washings can play a role along with the pH in controlling flocculation. Excess Fe-oligomer may also block the PILC
micropore channels and form large Fe crystallites during
catalysis. Thus, circumventing the numerous washings by
dialysis or base addition would not be beneficial. The
need to remove this excess though must be balanced with the
pillar hydrolysis that will undoubtedly occur with the time
and higher pH required for numerous washings.

Table 5 summarizes the relevant physical data for the

Table 5. Summary of Physical Data for Fe/PILC.

			maol Pe3+	Pillar		XRD (Å)	• €	Surface
Aut	Authors		meq clay	Age(hrs.)	Fe/unit celle	do o 1	do o 1	Area(m2/g)
A	A. This work	work a	30	Q	6.98	25.2 15.4	15.4	298
.	B. Tzou (58)b	4(88)	70	24	9.75	22.5	12.8	244
ິວ	Yaman (59)	C. Yamanaka et al.º (59)	ıc U	34	7.75	16.7	6.9	320

a.calcined 2 hrs. 350°C, air, 0.1M FeCl3 b.calcined 24 hrs. 350°C, air, 0.1M FeCl3 c.calcined 20 hrs. 350°C, vacuum, 0.04M [Fe3(OCOCH3), 0H 2H20]NO3 d.[Fe3(OCOCH3), 0H] + left 3 hrs. in clay suspension e.interlayer compositon, 02°(OH) + anion basis for silicate layer

iron pillared clay used in this work with that of Tzou and Yamanaka et al. Tzou's Fe/PILC contained approximately 40% more interlayer iron than the clay prepared in this work. This is due to the shorter aging times used here and the lower ratio of iron oligomer to clay. A higher surface area was obtained here however, which is consistent with the trend observed by Tzou. The amount of iron in A is also less than that intercalated by Yamanaka et al., yet surface areas are similar. The most significant feature of this comparison is the much higher basal spacing for calcined Fe/PILC A than that obtained by Yamanaka. It is also somewhat higher than that obtained by Tzou under similar iron concentration and pillar age. It is of interest that C used only a fivefold excess of iron whereas both A and B used larger excesses. Of course the Fe excess required the extensive washing procedure, while Yamanaka et al. centrifuged and washed "several times".

C. Fischer-Tropsch Catalysis

The Fe/PILC summarized in Table 5 was typical of well ordered Fe/PILC, so the catalytic and physical features presented in this chapter are those of this material. Figure 12 shows SF plots (eqn. 1) of the product distributions obtained using the catalytic methods outlined in chapter II, for three sampling times. Although the lines drawn through the data points for all three times have nearly the same intercept their slopes steadily increase

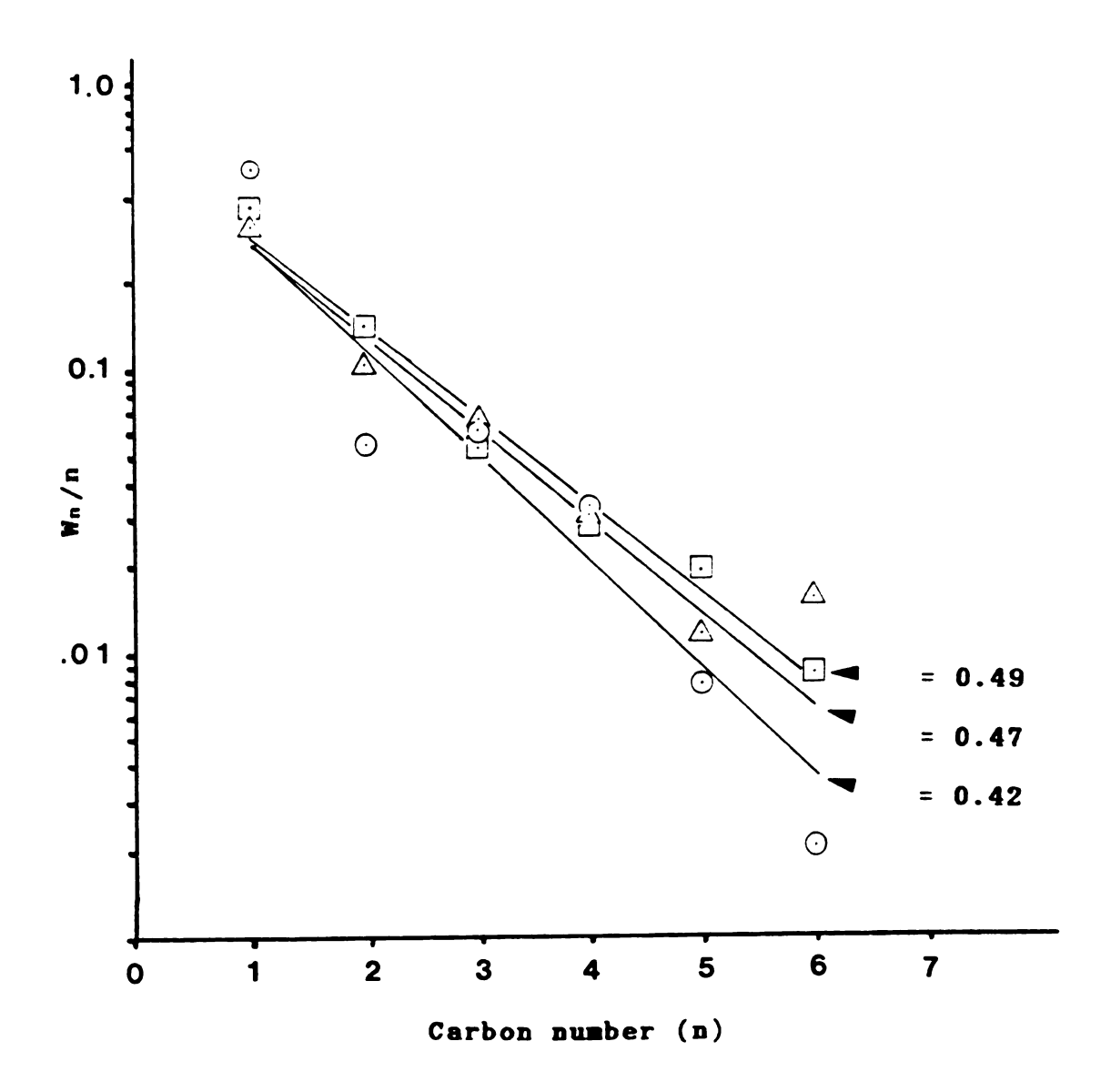


Figure 12. Schulz-Flory plots of Fe/PILC hydrocarbon production after 60 min. \odot , 103 min. \triangle , and 1259 min. \bigcirc of reaction. Reaction conditions were 120 psi, 275°C, H₂/CO=2, 2100 hr⁻¹ GHSV, and 1.7s contact time.

with longer run time. The probabilities of chain growth obtained from these slopes increase with time, reflecting the trend towards higher hydrocarbon production. This contrasts with the work of Krebs et al. (121) who applied surface analytical techniques along with catalytic measurements to compare FT features of reduced and unreduced magnetite (Fe₃O₄). In reduced magnetite and clean iron foils the α -values steadily decreased from 6 to 200 min which corresponded to the gradual increase in carbon deposited on the sample. They suggested that the "clean", reduced iron surface had the greatest ability to produce high chain growth probabilities (α).

The nature of the catalytic active site for iron is still a matter of considerable debate as the potentially active phases such as: iron oxide, reduced iron, and the numerous iron carbides formed may all be components of hydrocarbon production (122). The formation of carbide phases is represented below.

Fe₃0₄ \rightleftharpoons Fe[°] \rightleftharpoons FeC (X, \in , \in '...) Several studies (123,124) support the proposal that α -iron is active initially in FT, but rapidly deactivates due to the formation of graphitic overlayers. Yet, others (125,126) observed increasing activity with time which correlated with accumulation of iron carbides. Iron carbides in FT have been discussed in detail elsewhere (106).

For all three data points, methane falls above the weight fraction suggested by the least-squares line drawn

in Figure 12. This is particularly true at 60 min. This deviation is typical of FT distributions as excess methane may be formed from hydrogenolysis of higher hydrocarbons. Another general trend observable in Figure 12 is that deviations from the line decrease with time. For example, C₂ production is far lower than expected in the SF plot at 60 min, slightly less at 103 min, and on the line with the other hydrocarbon components at 1259 min.

These deviations can be depicted in a more illustrative way by using the α value obtained for each sampling time to produce a theoretical SF distribution by applying equation 1. Figure 13 shows such a comparison at 60 min between experimental and theoretical SF-derived data. The relative magnitude of these deviations can be better appreciated in this manner and the decrease in deviation with higher hydrocarbon easily noticed. Comparison between the experimental and SF theoretical distributions at 1259 min, in Figure 14 however, shows that indeed with time deviations from Schulz-Flory distributions become minor with increasing time on stream (TOS).

The distribution of olefins and paraffins, conversion data and the composition of the trapped reactor liquid are summarized in Table 6. The initial methane production of about 50 wt% drops considerably to 32% CH₄ at 103 min, which further indicates higher hydrocarbon production. The increase in conversion with TOS may be accounted for by the formation of a surface carbide vital to hydrocarbon

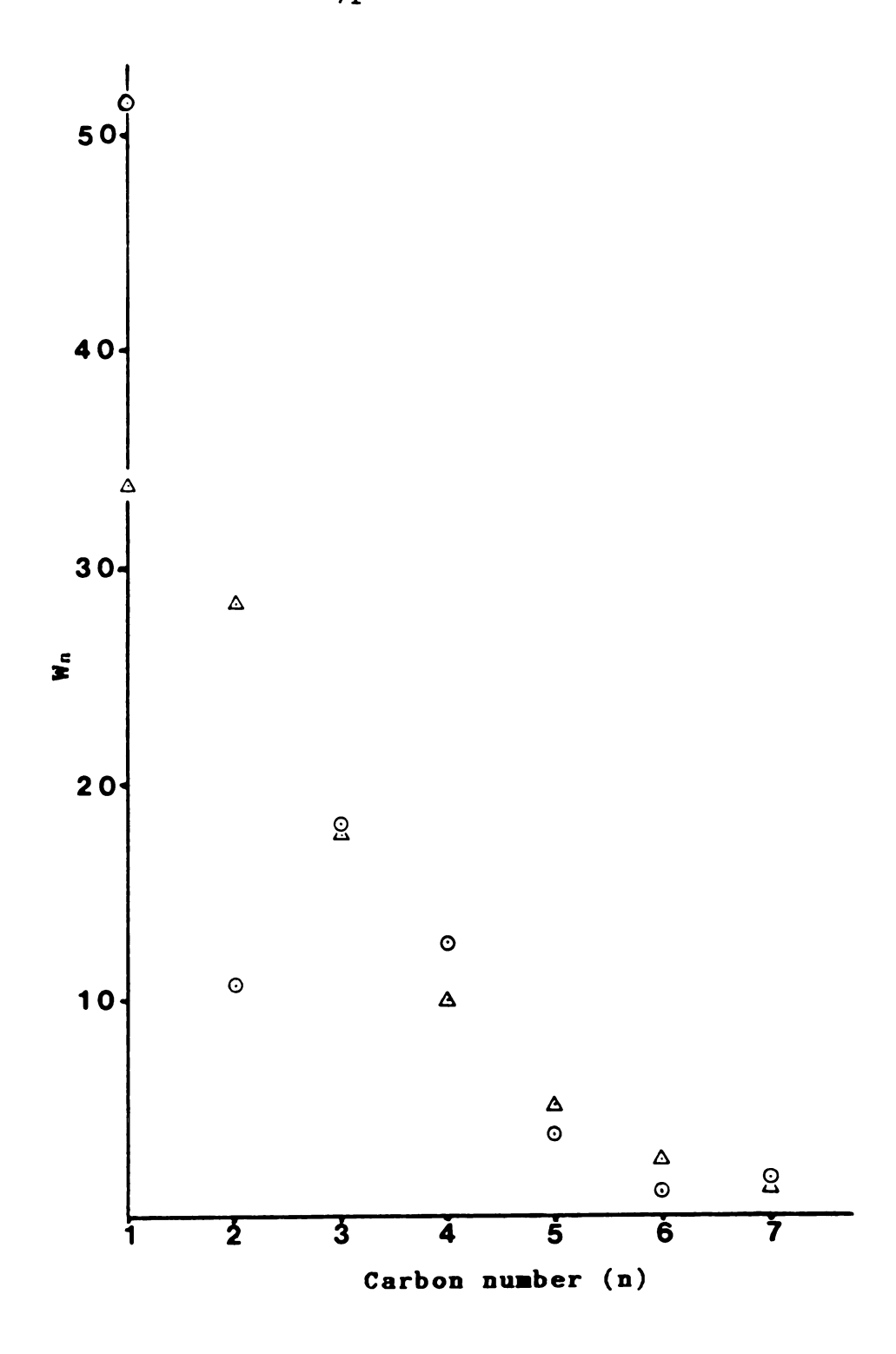


Figure 13. Experimental hydrocarbon production \odot for Fe/PILC (60min. TOS) compared to calculated \triangle (Schulz-Flory) distribution. A chain growth probability of 0.42 was used for the SF plot. Experimental data from Fig. 12.

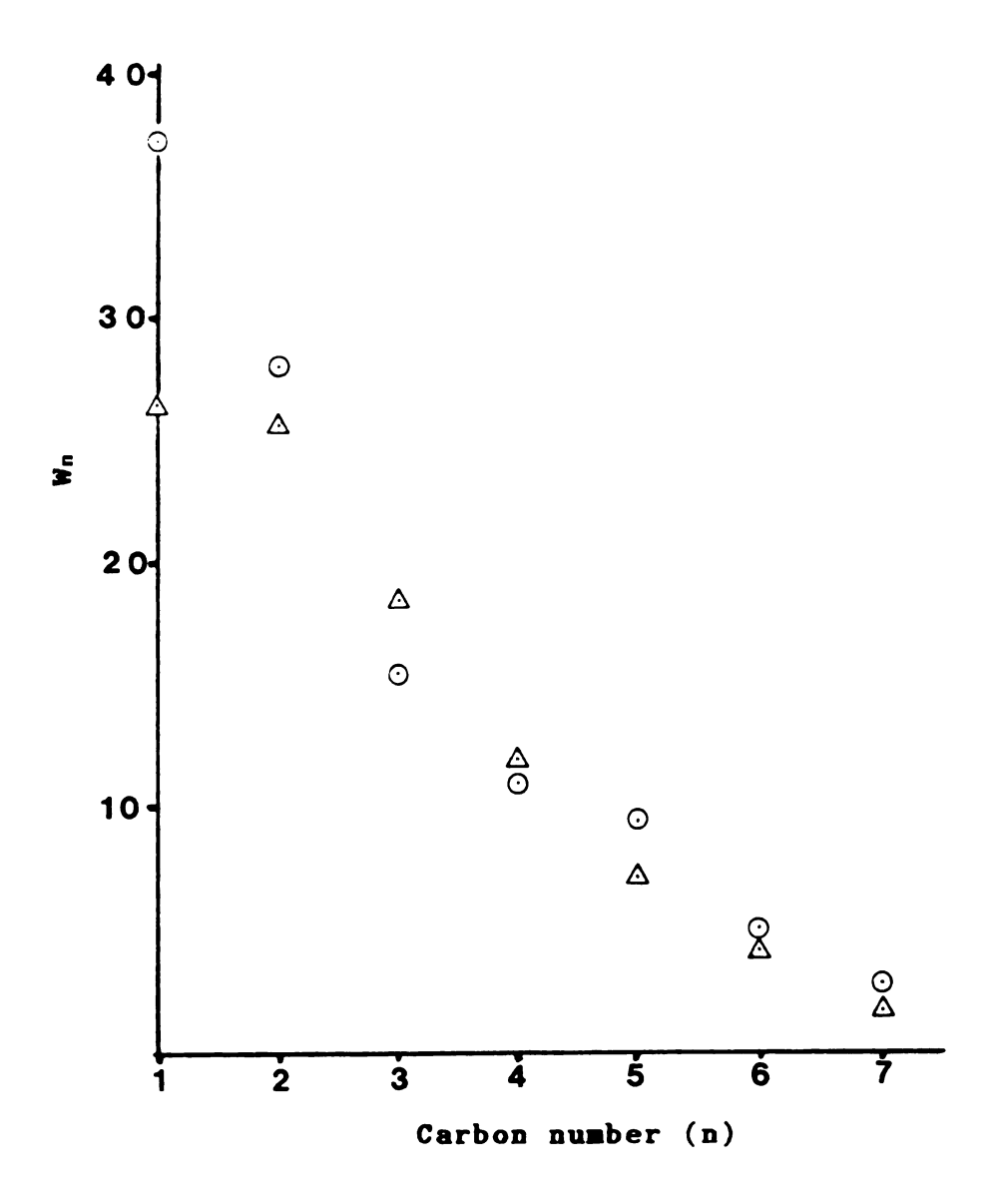


Figure 14. Experimental hydrocarbon production ⊙ for Fe/PILC (1259min. TOS) compared to calculated ⊡ (Schulz-Flory) distribution. A chain growth probability of 0.49 was used for the SF plot. Experimental data from Fig. 12.

Summary of an Typical Fe/PILC FT Product Distribution. Table 6.

						Wei	weight x				
TOS(min)	TOS(min) % Conversion	8	Cı	C2 =	C2 = C2 _	C3 =	ر ₃ -	*	Cs	ပို့	72
09	.75	.42	42 51.6	6.	8.6	9.8 16.3 1.3 12.7 3.8	1.3	12.7	3.8	1.2 2.4	2.4
103	1.1	.47	47 31.9 1.4		18.9	18.9 15.8 3.6	3.6	11.9	11.9 5.9	9.2	E
1259	1.3	.49	37.4	1.1	49 37.4 1.1 17.7 11.7	11.7	3.8	3.8 11.0	9.5	5.0 2.8	2.8

Reduced in Hz, 400°C, 4 hrs. Renction at 275°C, 120psi, Hz/CO=2, 35 ml/min or 300hr

Trapped liquid composition: 89.1% H20, 7.6% MeOH, 2.9% RtOH, .4% PrOH

production as mentioned earlier. The unreduced magnetite studied by Krebs et al. (121) and unreduced hematite (Fe₂O₃) studied by Dictor and Bell (127) both showed increased activities in the first 20 hrs of exposure to FT reaction conditions. These results are consistent with the above mentioned observations of the present Fe/PILC study.

Additionally, the values of α obtained in this work are similar to that of Arcuri et al. (128) for Fe/SiO₂ (α =0.43 at 14 atm, 250°C, H₂:CO=3), and Krebs et al. (121) (1 bar, 298°C, H₂:CO=3) where α ranged from 0.46 to 0.39. Dictor and Bell (127) showed α to increase with decreasing hydrogen partial pressure (pH₂), increased pCO, and decreased temperature whereas the gas flow rate had negligible affects. Although the α values for these studies are not directly comparable, they are very similar, suggesting that Fe/PILC catalyzed hydrocarbon chain growth in FT is similar to other dispersed iron catalysts.

The dominance of water in the trapped liquid (Table 6) is typical of iron-based FT catalysts where this is the primary path of oxygen removal from the catalyst surface. At elevated pressures the water gas shift reaction decreases (128). At the pressures used in Fe/PILC F-T, the CO₂ produced typically accounted for 6% of the total CO converted. The liquid fraction also contained significant portions of methanol and ethanol and smaller amounts of propanol. Methanol production increases with higher reaction pressures also, and may become the dominant product

(second only to CH₄) for iron and iron-cobalt catalysts (128). Branched hydrocarbon production was below the detection limits of the analysis system used for most Fe/PILC studies.

In numerous catalytic runs with well-ordered Fe/PILC the olefin/paraffin ratio decreased with increasing conversion. This is shown in Figure 15. The decreasing values of C_n^{-}/C_n^{-} versus conversion agrees with previously obtained results (128,130). It has been proposed that ethylene plays a special role in the chain growth process (71,130) as it can be readsorbed and incorporated into growing hydrocarbon chains. Another suggestion is that terminal olefins (in particular ethylene) are the principal products in FT (127), and that they can undergo further reactions to form paraffins and internal olefins. Increased conversion then may result in increased incorporation of light olefins into growing hydrocarbon chains. The incorporation of these olefins also explains C_2-C_3 hydrocarbon production below that predicted by SF, such as C₂ in Figure 12. The olefin/ paraffin ratio typically increases with decreasing H_2/CO ratio (olefin hydrogenation requires H2), decreasing pressure and temperature, and increasing gas velocities (122).

The fact that C_2 deviations from SF decrease with increasing time and conversion for Fe/PILC is interesting, because the above argument suggests that deviations should increase with larger conversions as more C_2^- is

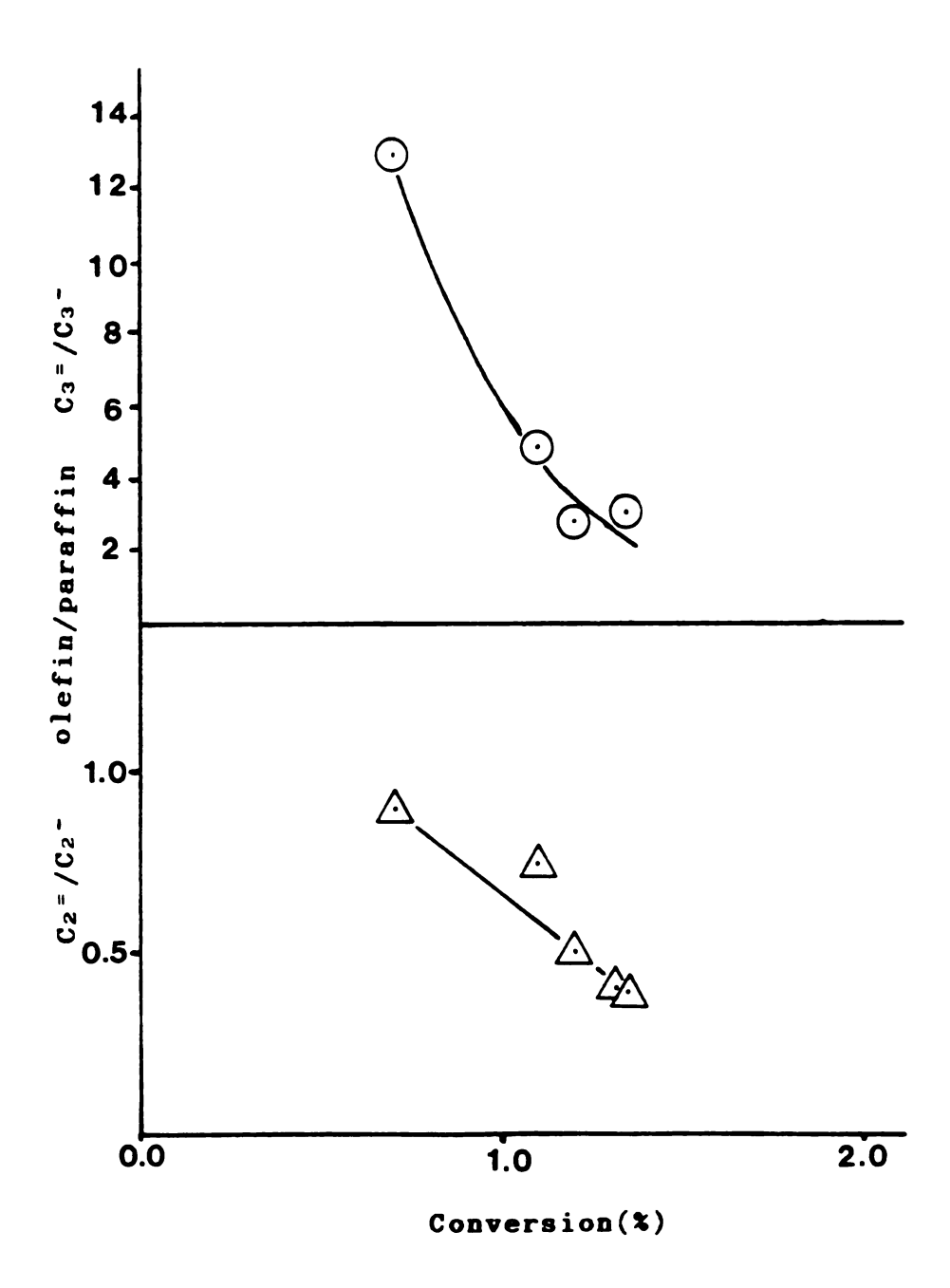


Figure 15. Olefin/paraffin production for Fe/PILC catalysts as a function of conversion for $C_3^{\,-}/C_3^{\,-}$ and $C_2^{\,-}/C_2^{\,-}$.

incorporated into growing chains. Also, the increase in α with time is a curiosity. This may be due to the greater propensity for light hydrocarbon production within the confines of the Fe/PILC microporous network initially. The fact that α changes with time suggests that the active site is changing with time, perhaps due to the changing nature of the iron pillar.

Previous studies with precipitated iron (122, 131, 132) and hematite (127) catalysts have shown that more than one α can be found in FT synthesis. In these studies, hydrocarbon production beyond a certain carbon number (typically C_{7-10} and higher) was significantly greater than predicted by the SF line for lighter hydrocarbons, and two chain growth probabilities were required to adequately fit the distribution. The origin of the break in α is not well understood at present, but in many instances potassium was used as a promoter. It has been suggested (122,131,132) that two different active sites arise from sites containing various levels of K. Potassium is known to promote the production of higher molecular weight hydrocarbons, and sites of varying alkali concentration may differ in their strengths of hydrocarbon adsorbtion explaining this effect. Yet, Huff and Satterfield (132) showed that similar iron catalysts without alkali promoters, could also generate product distributions requiring two α 's. It appears that nonuniformities in structure and/or composition of the active site can be responsible

for the bi- α anomaly. In the present work we can fit the product distribution with one α value but the fact that α changes with time suggests that there is a tendency toward two α values.

It is plausible that a structural or compositional reorganization of the Fe/PILC may account for the unusual shift in α with time, and the tendency toward higher hydrocarbon production. To examine such possibilities the fundamental nature of Fe/PILC catalysts and the local elemental composition was examined using scanning electron microscopy.

D. Scanning Electron Microscopy

Electron microscopy has been invaluable in establishing the morphology, structure, classification, and
properties of clay minerals (15,133,134). Clays can
exhibit a wide variety of textures as a result of the
layers being weaved into ribbon-like, cylindrical, or
matted fabrics. High resolution electron microscopy and
microanalysis have been used to discover new topologies of
multiple chain silicate structures, correlate local composition with polytype, and investigate atomic structure near
framework imperfections (135). In the case of montmorillonite the morphology of the elementary layer is platey,
but owing to the flexibility of the layers, isomorphous
substitutions which induce curvature or undulation, and the
turbostratic nature of layer stacking an aggregated
particle rarely exhibits three dimensional order. Thus

the texture of montmorillonite is raglike, even though the elementary layers are regularly stacked in the vertical direction.

The edge-on SEM image in Na⁺-Wyoming montmorillonite in Figure 16a demonstrates a number of elemental plates clinging to the edge, the stacking and bending of numerous layers (lower left), and the wavy morphology (Figures 16a and b). Early EM investigations noted that the intercalation of organic cations in clay galleries stiffened montmorillonite layers so that bending decreased (136). Isomorphous substitutions (chapter I) within the clay layers are partly responsible for the extensive clay undulations, as substitution of a larger cation for a smaller one will alter the mismatch between octahedral and tetrahedral layers (15). The intercalation of a charged pillared species in the galleries, then modifies the interlayer charge distribution so that oxygen framework distortions decrease and the layers become cemented together.

Figure 17 shows a specimen of Fe-pillared Wyoming montmorillonite that was prepared in the same manner as in Figures 16a and b. The increase in ordering of clay layers is clearly evident in these micrographs. Undulations have been greatly minimized through pillaring, though some bending and curling near edges are still present, as indicated in Figures 17b and c.

When the focused electron beam in the microscope impinges on a specimen surface, a wide variety of

Figure 16. Edge-on SEM view (a) of Wyoming Na+-montmorillonite air dried on glass. SEM image (b) near a crack in the air dried clay.

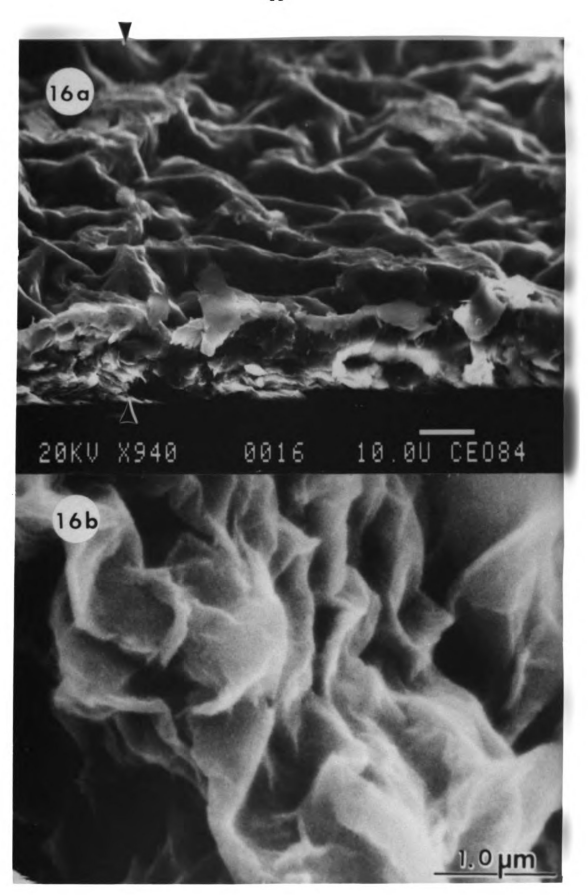
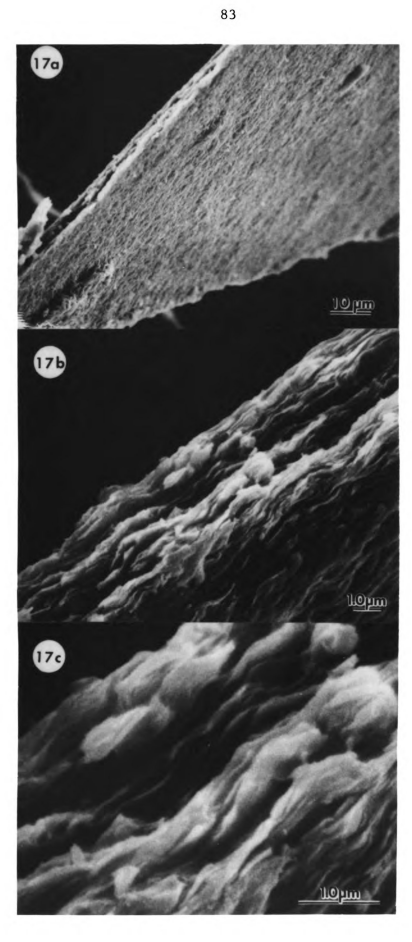


Figure 17. SEM images of Fe/PILC air dried on glass at various magnifications. The substantial decrease in layer bending is evident at all magnifications.



interactions occur, including the emission of secondary electrons, backscattered electrons, characteristic and continuum x-rays, Auger electrons, and other assorted photons (137). These signals originate from specific volumes or depths within the sample that are a function of average sample atomic density, and the initial electron beam energy. The specific emission volumes are illustrated in Characteristic x-rays can be produced when the Figure 18. incident beam dislodges an atomic inner shell electron, resulting in an atom in a excited state. When the atom returns to the ground state by transition of an outer shell electron to fill the inner shell vacancy, the atom loses energy by the emission of an x-ray photon. Due to quantized atomic energy levels the emitted x-ray will be characteristic of each excited atom. Characteristic x-ray emission offers the capability to perform in situ elemental analysis with microscopic resolution to identify elements and investigate their distribution.

Figures 19a and 20a show electron micrographs of airdried iron-pillared clay samples. A computer controlled scan of the electron beam accross the sample, and analysis of the characteristic x-rays produced, will give the distribution of counts recorded for each element. Figures 19b and 20b show these linescans between points indicated on the neighboring micrographs. The linescan in 20b gives a qualitative indication that regions of high iron concentration corresponded with regions of low Si and Al.

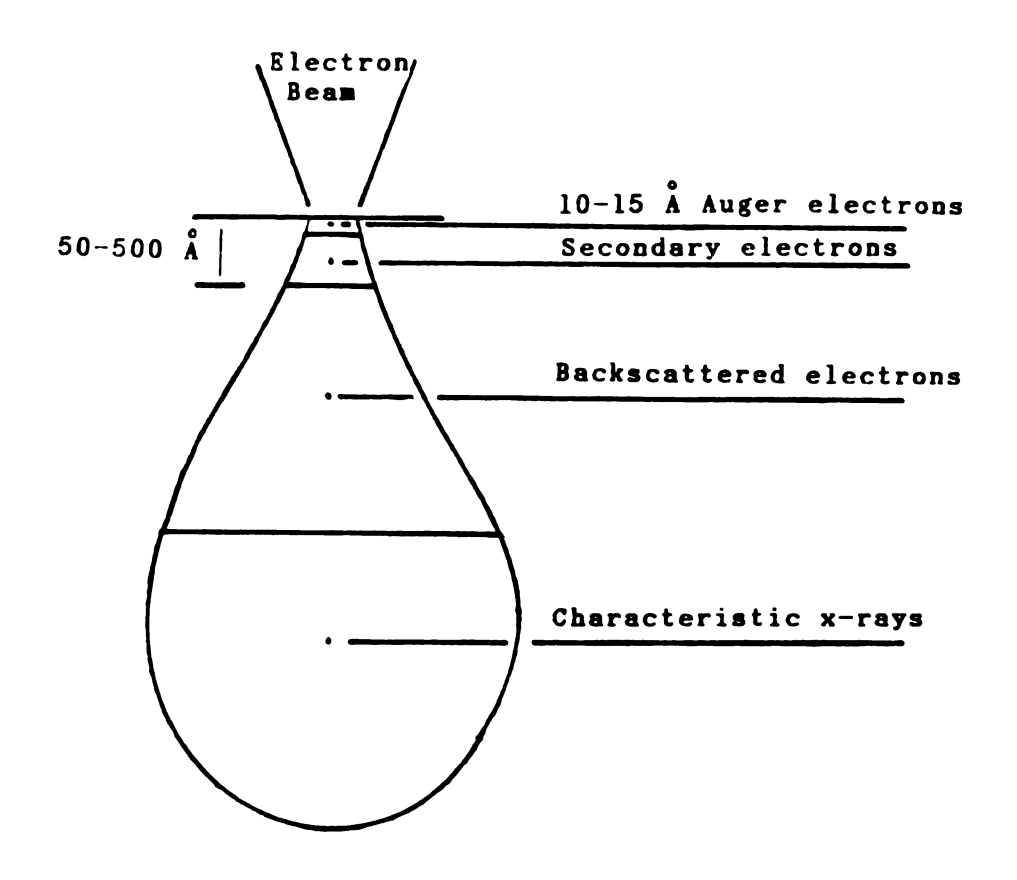
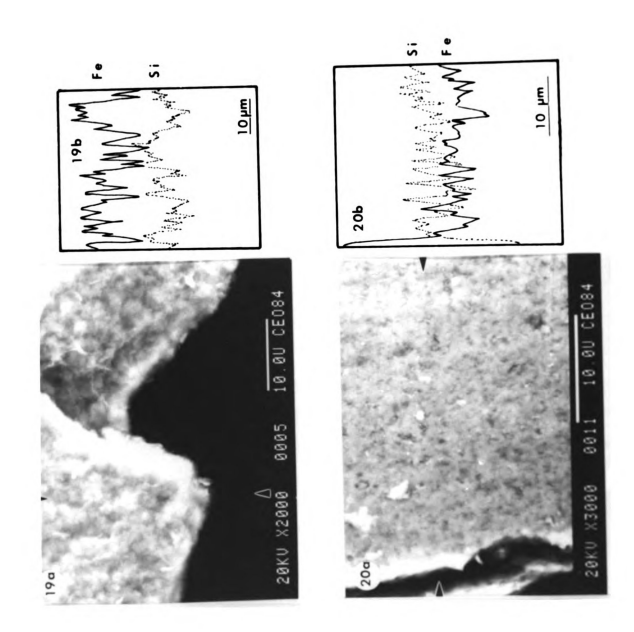


Figure 18. Generation of various signals in samples due to interaction with the electon beam in electron microscopes.

Figure 19. SEM image of Fe/PILC (a) and the elemental distribution (b) determined by an x-ray microanalysis linescan.

Figure 20. SEM of a different area (a) and an accompanying linescan (b) between the arrows.



A linescan including the region near an edge (Figure 20b) shows a high concentration of iron near the edge relative to Si and Al. The Si and Al distributions are indicative of relative clay concentrations. The fact that iron was found in excess where clay was in less abundance was unexpected. This pointed to the fact that iron deposits may exist within the clay and at the edges. The calcined Fe/PILC samples were kept under room temperature conditions for the months between synthesis and SEM investigation. That inhomogeneities in Fe distribution were evident was interesting as the Fe/PILC used exhibited relatively welldefined XRD patterns after calcination. We postulate that redistribution of Fe occurs in these clays, and this may have particular importance in explaining the steady increase in α with time in the catalytic studies. The implications and validity of these qualitative inferences were further investigated.

When x-rays are induced by electron beam bombardment they are partially absorbed as they travel from their point of emission to the surface. Based on the 20kv accelerating voltage and the density of clay the maximum depth of x-ray production is near 6-7 microns in these studies. X-ray production in SEM is a function of the sample topography, as the electron trajectories and path length are dependent on the angle between the incident beam and sample. The elemental distributions shown in the linescans then are qualitative as the corrections for x-ray absorption, atomic

number and fluorescence effects required to quantitate results (138) were not applied.

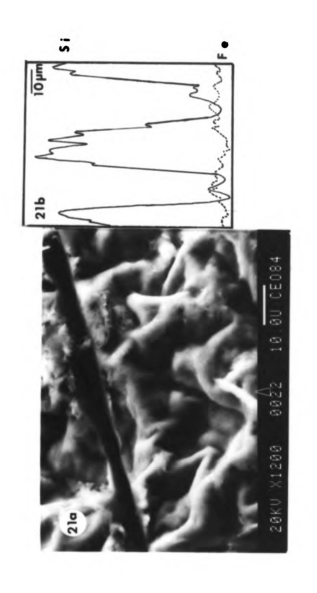
To obtain a better picture of the validity of the linescan interpretations, the Na⁺montmorillonite shown earlier, and a sample of thermally, stable, chromium-pillared clay prepared by S.D. Landau (104) were studied. Figure 21 shows an SEM micrograph of Na-montmorillonite along with a linescan between the points indicated. The linescan exhibits severe fluctuations in Si and Al x-ray count rates as the beam traverses the peaks and valleys of the sample. X-rays are nearly completely absorbed in regions of severe depression, yet the relative concentrations of Al and Si correspond with one another. Iron here is near the threshold level of detection as the only iron in natural montmorillonite is that found due to substitutions in the octahedral layer (about 4 wt% reported as Fe₂O₃). In Figure 22 a linescan between the points indicated in Figure 16a is presented showing less severe x-ray count fluctuations. Although the x-ray counts vary with morphology, they do so in a consistent manner. It should be reinterated that such fluctuations should be far less with Fe/PILC than with Na⁺montmorillonite as the dried film undulations are far less severe.

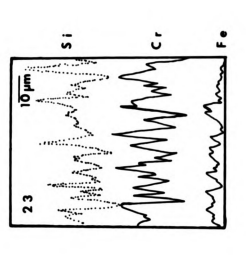
Figure 23 illustrates the linescan found on a basal surface of a highly ordered chromium pillared montmorillonite, which supports the argument that pillared clays should show a homogeneous distribution of elements in

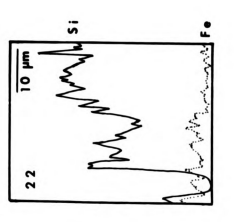
Figure 21. SRM image of the undulating surface of Na+montmorillonite (a) and an x-ray microanalysis line-scan (b).

Figure 22. Blemental microanalysis of Na+-montmorill-onite between the arrows in Figure 16a.

Figure 23. Blemental linescan of a well ordered Cr-pillared montmorillonite. Here the Cr distribution follows that of Si, indicating a homogeneous pillared clay.







qualitative x-ray microanalysis.

E. X-Ray Diffraction

At this point it was evident that heterogeneities in Fe distribution in Fe-pillared clays did indeed exist and that alteration of iron pillar structure and Fe distribution within the clay galleries was occurring with extended aging under ambient conditions.

When the Fe/PILC used in the catalytic runs was examined by XRD, shown in Figure 24, it revealed no discernable reflections, suggesting that an amorphous material had formed. Reexamination of the same XRD slide prepared after Fe/PILC synthesis, which had shown a ordered, highly expanded material after calcination, revealed that it had become x-ray amorphous after 3 months under atmospheric conditions. Apparently the humidity present in air causes the iron pillar to hydrolyze, which results in an amorphous material. Some of this iron then may agglomerate in the reactor or SEM beam. This would explain the presence of large Fe crystallites within the clay and iron being transported to the edges of individual clay platelets. increase in α then is most likely a result of the small Fe active sites on the pillars decaying with time and large Fe agglomerates being formed.

Aluminum and zirconium pillared clays are typically stable after calcination with respect to this reversal of the pillaring process but many other pillars exhibit pillar

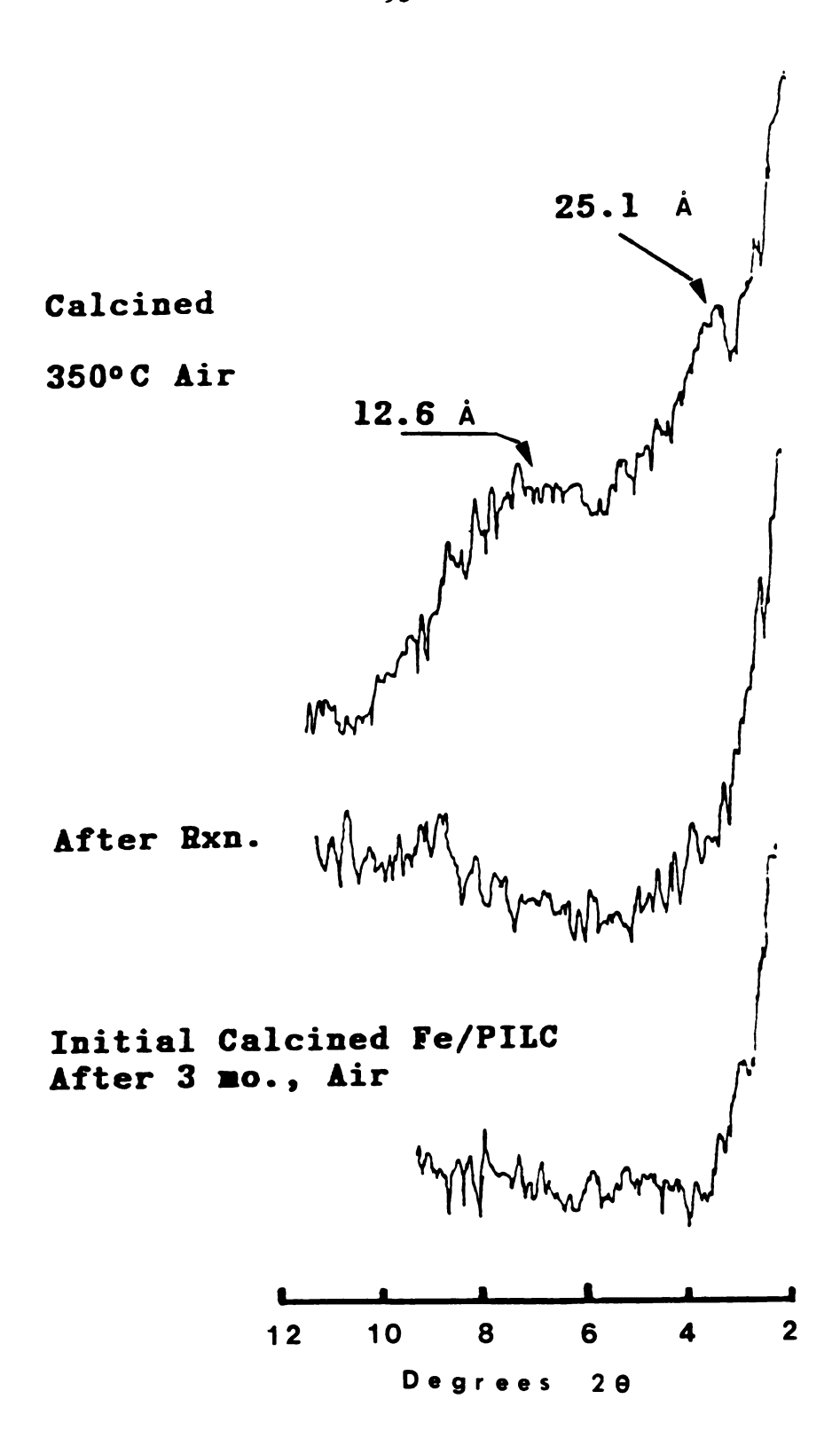


Figure 24. XRD patterns of Fe/PILC before and after Fischer-Tropsch reaction. The initially well ordered material (top) was essentially XRD amorphous after 3 months in air.

destruction at elevated temperatures. Indeed, pillar hydrolysis even limits the application of Al and Zr pillared clays for catalytic cracking due to steam induced pillar hydrolysis.

The fact that iron pillared clays show an instability towards pillar hydrolysis and layer collapse at the relative humidity of air strongly suggests that synthesis of Fe/PILC stable under the conditions of FT, where water is produced, would be improbable. Thus, more stable pillared clays such as Al-pillared clays were investigated as means to supporting catalytically active FT metals. Even though the iron pillar did not have the long term stability initially hoped for, the pillar was certainly active in FT initially. The novel idea of confining the active metal between clay sheets in the form of a pillar demonstrates that pillars themselves may be considered as catalytically active components.

F. Conclusions.

The iron pillared clays used here offered unique catalytic sites for Fischer-Tropsch (FT) hydrocarbon production as the metal particles were very small and confined within the microporous cavities of the pillared clay. These iron-pillared clays had higher basal spacings at elevated temperatures than any previously or presently reported Fe intercalated clay system. The high gallery heights of these pillared smectites (15 Å), interlayer surface areas, and initial thermal stabilities suggested that these materials

had considerable potential for investigating unique catalytic properties of the small iron active sites. The unusual catalytic site in these systems was the pillar itself.

The pillar was indeed active in FT converting carbon monoxide to C_1 - C_7 hydrocarbons. Straight chain paraffins and olefins were the dominant hydrocarbon products, although methanol, ethanol and propanol were also detected. Water was the major component of the trapped liquids (87 wt%) with the remainder composed of the light alcohols.

Product distributions primarily followed the Schulz-Flory (SF) relationship with significant deviations in the C₁-C₄ range being present at short run times. These deviations were common however of the FT process, such as high methane and low C₂ production. Deviations from SF decreased significantly with longer run times, and by 20 hrs, hydrocarbon production showed no deviations. Olefin/paraffin ratios increased with greater CO conversion in agreement with previous supported iron catalysts.

The probability of chain growth (α) derived from SF plots of hydrocarbon distributions slowly increased with time signifying the trend toward higher hydrocarbon production. The decrease in α with time was aided by the drop in methane production from 50 wt% at 60 min, to near 37 wt% at greater than 100 min of reaction. This propensity for higher hydrocarbon production may have been related to structural or compositional changes of the active site with time. This possibility was supported by reports of two

chain growth probabilities on supported Fe-catalysts, that may have active sites differing in structure or relative degrees of promotion by potassium.

Characteristic x-ray production induced by the electron beam in a scanning electron microscope was used to examine the distribution of elements within these pillared clays. This microanalysis indicated heterogeneities in the iron distribution. Regions of high iron concentration corresponded to low concentrations of the Al and Si of the clay. Additionally concentrations of iron were enriched at edges relative to basal planes which suggested iron migration. Natural montmorillonite and a well-ordered chromium pillared clay were used as standards to test the validity of the qualitative microanalysis. The implications of the fluctuation in Fe distributions of Fe/PILC were supported by this work.

This led to reexamination of the iron pillared clay used in catalysis and the material that had not been subjected to the harsh reaction conditions. X-ray diffraction patterns of these materials revealed that iron-pillared clay had collapsed in the reactor, when stored at atmospheric conditions. As the relative humidity present in air induced pillar hydrolysis and reorganization of the Fe/PILC, synthesis of iron-pillared clays that would be stable under FT conditions (where H₂O is produced) was deemed improbable.

Although catalytically unique, the Fe pillar

demonstrated activity in FT hydrocarbon production, the demise of the pillared structure with humidity led us to investigate other means of highly dispersing active metals in the microporous regions of pillared clays.

CHAPTER IV

Ruthenium on Alumina Pillared Montmorillonite

Clays pillared with aluminum oxycations have generated more interest and research since their discovery than any of the other inorganic pillars mentioned in Chapter I. This is due to their excellent thermal stability, Bronsted and Lewis acid sites, and adjustable pore structure. Pinnavaia and coworkers (139) demonstrated that the method used to dry the flocculated pillared clays was more important than whether the Al-oligomer was obtained from base hydrolyzed Al solutions or a commercial reagent (aluminum chlorhydrate). In this study air drying of pillared clay solutions yielded materials with zeolite-like micropores whereas freeze dried clays had considerable macropore character. They suggested that the presence of macroporosity in freeze dried clays was due to delaminated regions, where edge to face and edge to edge association of clay layers occurs, based on similarities to a synthetic lath shaped hectorite (Laponite) that exhibits strong delamination tendencies. The presence of delaminated regions may alter the diffusion properties of reactant molecules, allowing larger molecules to penetrate the clay interior for catalytic reactions. The importance of this aspect of pillared clays has been further investigated by catalytic (140,141) and physical characterization (142) studies.

Although the delamination model explains numerous differences between air dried and freeze dried clays, recent work by Van Damme and Fripiat (143) suggests another expla-They reanalyzed earlier adsorption data for freeze dried and air dried clays by a fractal model and found that pillars are homogeneously and regularly distributed in both of these alumina pillared clays, and not concentrated in a zeolite-like region relative to a delaminated area. alternative explanation for these observed differences is that continued pillar hydrolysis occurs in air dried clays filling additional porespace, whereas in freeze dried clays hydrolysis is halted due to the temperatures employed and the rapid withdrawal of water (144). This is supported by the fact that when Al-pillared clay solutions were washed only 2-4 times and then dialyzed, adsorptions of perfluorotributylamine and surface areas were lower than pillared clays washed and centrifuged numerous times (104). Both clays were air dried and had similar gallery heights. The size and distribution of pores within pillared clays has particular relevance to catalytic studies with these materials, as the dimensions and populations of constrained cavities are affected.

The interaction between the pillars and neighboring clay sheets has also been an area of active research in the past few years. Plee et al. (145) showed that a

tetrahedrally charged smectite (beidellite) interacted with the clay layers when calcined, whereas octahedrally charged smectites failed to react when treated similarly. The authors suggested that the substantial structural transformation for beidellite arose from the formation of a 3 dimensional network as the pillar was grafted onto the clay structure. The resulting materials had high surface areas and increased acidity relative to octahedrally charged clays. The crosslinking of pillars to the clay network may result in enhanced thermal stabilities and increased resistance to pillar hydrolysis which would also be of interest in catalysis.

The use of well defined molecular clusters in loading metals on catalyst supports has gained considerable acceptance in the past decade due to the advantages mentioned in chapter I. The discovery by Giannelis (103) that metal carbonyl clusters can react with the intracrystalline acidity of alumina pillared clays is of particular interest as it allows metals to be highly dispersed in clay galleries. For the present study the fact that alumina pillared montmorillonite (APM) was found to protonate Ru₃(CO)₁₂ was especially interesting as ruthenium is one of the most active FT metals and has a propensity for forming high molecular weight hydrocarbons.

Giannelis found that $\mathrm{Ru_3(CO)_{12}}$ reacted with the acid sites of activated APM, forming ($\mathrm{HRu_3(CO)_{12}}^+/\mathrm{APM}$), which was identified by infrared spectroscopy. Removal of the

protonated cluster from the interlayer by exchange with KPF_6 in acetone, allowed the cluster to be further identified and confirmed by agreement with literature results. Experiments with collapsed clays exposed to Al-polycations showed that $Ru_3(CO)_{12}$ clusters were only physisorbed and could be removed by CH_2Cl_2 washings. The protonation of this carbonyl cluster in homogeneous solution requires 98% sulfuric acid, which again demonstrates the intracrystalline acidity of APM. Cluster protonation within the gallery however, was reversible and after a few hours in air the infrared absorptions were identical to $Ru_3(CO)_{12}$. Prolonged exposure to air, or vacuum treatment at $25^{\circ}C$, led to mononuclear ruthenium complexes of the type $[Ru(CO)_2(O-Al <)_2]_n$. When heated in air, further decarbonylation occurred and oxidized Ru atoms were formed on the clay mineral.

The objective of this present study was to characterize the catalytic features of these ruthenium loaded clays in FT. The dispersal of Ru₃(CO)₁₂ in APM due to the intracrystalline acidity was particularly important as the ruthenium was specifically contained in micropores where a constrained environment would exist for the FT site. Thus, the distribution of hydrocarbons obtained in FT catalysis was closely examined for potential influence of the constrained site or chemical nature of APM.

The breakup of the trinuclear Ru carbonyl skeleton and the eventual decarbonylation to Ru atoms suggests that Ru mobility on the clay surface would have to be examined as

metal sintering may occur. The most effective means of characterizing the change in Ru disposition was high resolution electron microscopy. A brief introduction is given here, although the reader may wish to examine the references given for additional information.

High resolution electron microscopy is one of many high vacuum techniques that have been employed extensively recently for the characterization of catalyst surfaces. The imaging and microanalysis capabilities of this technique have provided important information concerning the composition, structure, and disposition of the fundamental particles that constitute heterogeneous catalysts (146-148). Recent efforts in this field have focused in part on the imaging and analysis of metal crystallites of various supports (149).

Although scanning electron microscopy (SEM) and transmission electron microscopy (TEM) can provide a great deal of information, the most powerful and versatile EM technique for catalyst characterization is analytical electron microscopy (AEM). The dedicated AEM used in this work (a Vacuum Generators HB501) has a very bright (yet small) electron beam, ultrahigh vacuum specimen area (10⁻⁹ to 10⁻¹⁰ torr), and a variety of imaging and analysis capabilities. The specimen chamber and arrangement of various detectors in the VG HB501 is illustrated in Figure 25. In addition to the analysis methods shown, microdiffraction patterns can also be recorded, and the availability of

SCANNING TRANSMISSION ELECTRON MICROSCOPE

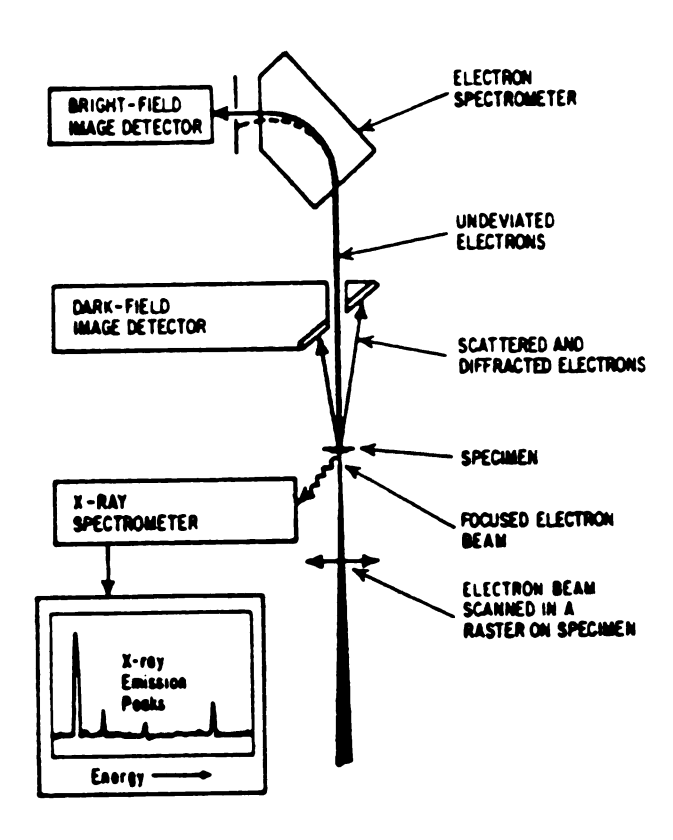


Figure 25. Arrangement of detectors in the specimen chamber of a dedicated STEM. Reproduced from ref. 148.

Table 7. Summary of Physical Data for Al-Pillared Clays.

	XRD dool(Å)	Surface Area	PFTBA Adsorption (mmol/g)
This work	18.4	345	0.41
Landau (104)	20.1	369	0.42
Tzou (58)	18.5	260	0.24

clays calcined at 350°C

PFTBA = perfluorotributylamine

electronic processing allows the signals from the dark and bright field detectors to be combined.

Dark field images are of particular importance in EM investigations of supported metals as the electrons deflected at high angles by supported metals are preferentially recorded in dark field.

A. Physical Properties of APM and Ru/APM

The APM obtained from the synthetic method described in Chapter II had the physical properties listed in Table 7. These properties were similar to those previously obtained by Landau (104) and exhibited higher surface areas and PFTBA adsorptions than comparable materials prepared by Tzou (58).

Elemental analysis showed that ruthenium loading ranged from 0.2 to 0.5 wt%. Characterization of these materials by infrared spectroscopy (Figure 26a) revealed that they were protonated Ru clusters bound within the clay interlayer, in agreement with the previous work mentioned (103). When the Ru/APM samples were weighed and loaded into the reactor tube they were still green. Infared spectroscopy of these materials prior to catalysis revealed that the protonated complex had undergone decarbonylation in the dessicator (Figure 26b) to form a complex similar to that previously assigned to monomeric [Ru(CO)₃X₂]_n/Al₂O₃ by Kuznetsov and coworkers (150). Although the APM was not examined in situ by infrared in the present work, a few post-catalysis samples were characterized by infrared as



Figure 26. Infrared spectra of Ru/APM (a) immediately after synthesis (2130, 2104, 2080 cm⁻¹), (b) prior to catalysis, aged 1 month in dessicator, (2150, 2080 cm⁻¹), (c) post catalysis after 12.5 hrs., 225°C rxn. (2100, 2056 cm⁻¹). a. ordinate expansion 400x.

shown in Figure 26c. These absorbtions are at higher wave numbers (2100, 2056 cm⁻¹) than those assigned by the above mentioned authors to $[Ru(CO)_2X_2]_n/Al_2O_3$ (2045-2050, 1950-1970 cm⁻¹) and may be due to CO adsorption on Ru crystallites. When the post-catalysis Ru/APM samples were examined by XRD the reflections observed indicated that APM was stable under FT conditions, in contrast to Fe/PILC. For example, a typical APM used in this study had a d_{001} = 18.4Å. After this material was loaded with the Ru cluster, prereduced in the reactor at 420°C for 5 hrs., and run 30 hrs. at 275°C in FT synthesis, it still gave an 17.8 Å d_{001} reflection. Thus despite these harsh conditions, and the production of H_2O in FT alumina pillared clays were stable and retained their expanded gallery heights.

B. Pristine vs. Prereduced Ru/APM Catalysts

As mentioned earlier, metal carbonyls provide a low metal oxidation state when used as catalyst precursors. Although it is highly probable that support interactions partially oxidize the Ru in these clusters, completely reduced Ru decomposition products have been claimed (151) for Ru₃(CO)₁₂ vapor impregnated zeolites. The dispersion of these metal complexes in zero-valent, or low oxidation states that can be readily reduced, offers the advantage that catalyst prereduction can be avoided. This is desirable as the elevated temperatures employed to reduce metal catalysts may induce metal migration and agglomeration.

To examine whether the freshly prepared Ru/APM catalysts would be active in FT (indicating low valent Ru initially), a number of catalysts were examined without prereduction in hydrogen. Although ${\bf C_1}$ to ${\bf C_5}$ hydrocarbons were detected for catalysts without prereduction, conversion of CO was often very low (0.4%) at one atmosphere and 275 °C. Elevated pressures resulted in increased conversion. At short run times (8-45 min.) unusual FT product distributions were obtained that showed significant devia tions from common Schulz-Flory distributions. Among the uncommon features observed were low methane production (26 wt%), relatively high yields of (C_6-C_{10}) hydrocarbons, and the appearance of more than one chain growth probability. These features were short-lived however, and after approximately 2 hours: no deviations from SF were found, methane yields increased dramatically, and production of higher hydrocarbons decreased. Although conversion increased substantially with longer reaction times, this was normally due to the increase in methane production.

Figure 27 shows a particularly interesting example of a Ru/APM Fischer-Tropsch catalyst that was <u>not</u> prereduced in hydrogen prior to catalysis. This experiment showed an SF distribution of C_1 - C_5 hydrocarbons and featured unusually high production of C_6 - C_{10} hydrocarbons. These deviations were slightly diminished at a reaction time of 43 min however, and by 138 min the product distribution followed that predicted by SF with only two exceptions. At

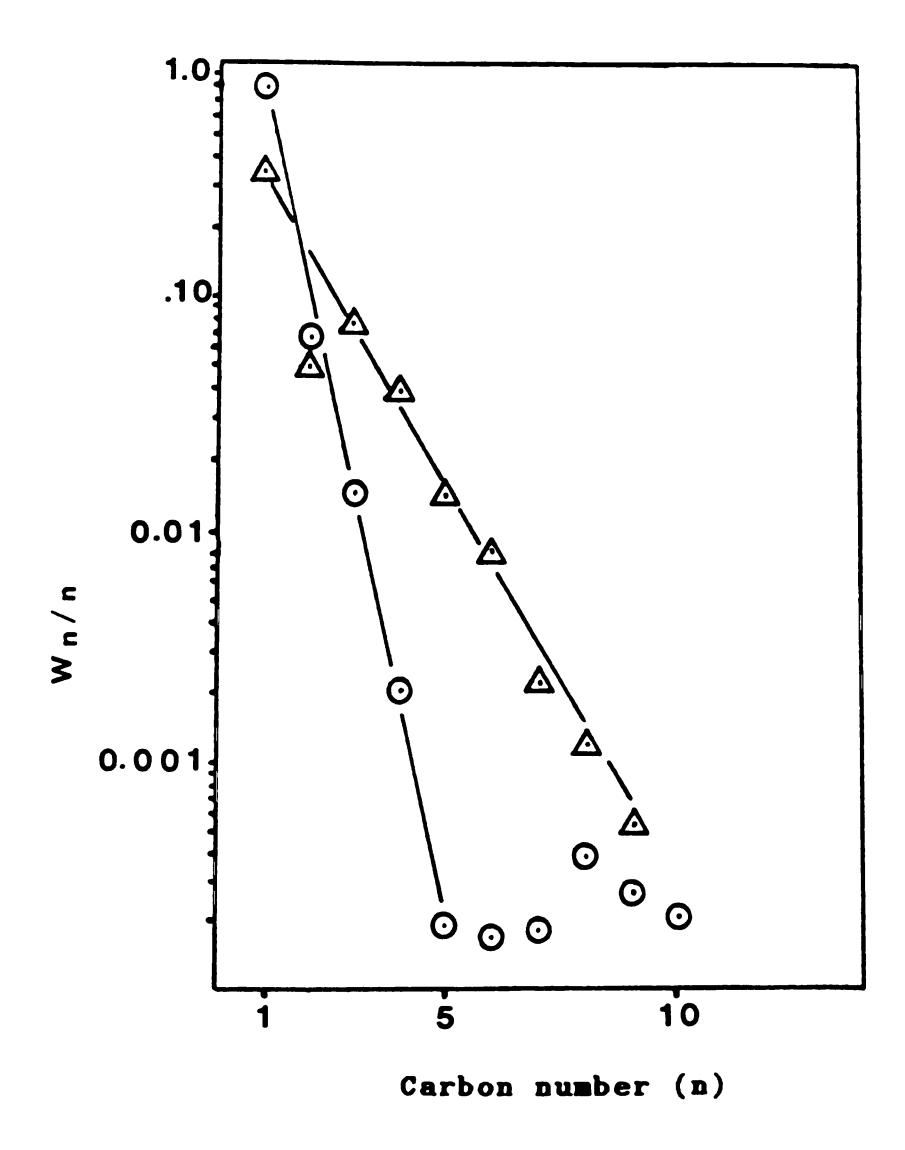


Figure 27. Schulz-Flory plots of Ru/APM catalysts after 8 min. \odot , and 138 min. \triangle of Fischer-Tropsch. The catalyst was not prereduced prior to reaction. Reaction conditions: 275°C, 8 atm., 300 hr⁻¹, H₂/CO = 2.

even longer times on stream the SF plots obtained were similar to that at 138 min. Conversion for this reaction at 8 atm was 9.8% so that production of the unusual quantities of C_6 - C_{10} hydrocarbons was substantial and easily detected by gas chromatography. In this case methane selectivity decreased with time.

The most interesting feature of the deviations in Figure 27 is that the product distribution appears to follow a very different chain growth probability for C1-C5 as compared to C_6-C_{10} hydrocarbons. Although the presence of two chain growth probabilities in FT has been reported for iron-based catalysts, as mentioned in Chapter 3, ruthenium catalysts have not exhibited this phenomenon. The initial heterogeneity of the Ru active site may result in a variety of geometrical structures of CO attachment which result in different activation energies for reaction intermediates, and enthalpies of absorption for reactants and products (152). A number of studies (153-155) indicate that CO can adsorb on ruthenium in monoadsorbed and diadsorbed (CO-Ru-CO) forms. The diadsorbed form was associated with isolated Ru atoms, or very small clusters which interact strongly with oxygen from the support, in earlier work (150,155). The geometry of CO adsorption may have particular importance as experiments by Kellner and Bell (155) suggested that sites that monoadsorb CO are active in FT whereas diadsorbed CO sites were inactive.

In experiments without a prereduction step, ${\rm H_2}$ and ${\rm CO}$

Table 8. Ru/APM Catalytic Data at 1 atm.

	Reaction						Weight &	×		
Pretreutment	Temp. (°C) (103	(10°) Rate	Conversion(%)	Cı	C3	C3	* 3	C _S	" "	C., •
nonreduced	275	2.7	o. 3	17.4	14.7 (1.4)	.	2.2 (6.5) [0.04]	1.4 (1.0)		
prereduced	275	8	0	70.8	11.1	8.1	4.2 (2.6) [0.07]	4.0 (2.4) [1.4]	0.8 (0.7) [.74]	<u>:</u>
prereduced	225	4.0	0.4	46.3	10.0	16.2	13.4 (5.6) [0.06]	9.6 (3.6) [1.2]	4.5 (0.8) [1.2]	-

All data at 50 min TOS
() olefin/paruffin ratio
[] branched/straight ratio
rute in mol CO
g cat hr

flows were equilibrated over the catalyst at room temperature and 120 psi before the temperature was increased to 275°C. It is likely that decomposition of the carbonyl cluster in H₂ and CO gave Ru active sites dissimilar to those found under steady state conditions. The changes in product distribution, chain growth probability, presence of SF deviations and conversion are probably a result of the active site reaching a homogeneous, steady state structure with time.

A comparison between catalysts that were not prereduced with those that were reduced at 1 atm revealed significant differences as demonstrated in Table 8. Ru/APM catalysts prereduced in H2 at 420°C gave greater conversions, reaction rates, and higher hydrocarbons than the pristine catalysts for reaction conditions of 1 atm. and 275 °C. Small amounts of C₅ hydrocarbons were obtained with nonprereduced catalysts whereas prereduced Ru/APM gave significant yields of hydrocarbons up to Cg. For prereduced catalysts methane production was lower than that of nonprereduced catalysts. Although only a limited number of data points were obtainable for olefin/paraffin and branched straight chain ratios, these values are given in Table 8 to illustrate that olefin/ paraffin ratios are high and branched hydrocarbon production is minimal for light hydrocarbons. Representative data for prereduced Ru/APM catalysts reacted at lower temperatures is also included here as it shows that conversion decreased substantially.

The Schulz-Flory plots shown in Figure 28 demonstrate that higher hydrocarbon production is favored for the prereduced catalysts. The yields of the various hydrocarbons produced fall on a straight line for all three run conditions, obeying SF. Further, the slopes for both prereduced runs are clearly similar, but these slopes differ from the catalyst that was not prereduced. Additionally, it should be pointed out that methane production decreased substantially when Ru/APM catalysts were run at 225°C as compared to higher reaction temperatures. Methanation is favored at higher temperatures, as shown in the simple scheme of run variables in Chapter I, so this result is expected.

What was not expected is the relatively large difference between the α values for nonprereduced catalysts compared to their prereduced counterparts. The relationship between these plots does not change significantly in the first few hours on stream either, suggesting that a significant difference between the steady state nature of nonprereduced and prereduced catalysts. Additionally, the deviations from SF distributions found initially for nonprereduced catalysts were not observed for prereduced catalysts.

Infrared investigations of $\mathrm{Ru_3(CO)}_{12}$ decomposition products on $\mathrm{Al_2O_3}$ as a function of treatment conditions (150, 156-158) have shown that surface aluminates and microcrystallites of Ru form in $\mathrm{H_2}$ at temperatures above 350°C. Kuznetsov et al. (150) investigated ruthenium carbonyl clusters of varying nuclearity and found that all

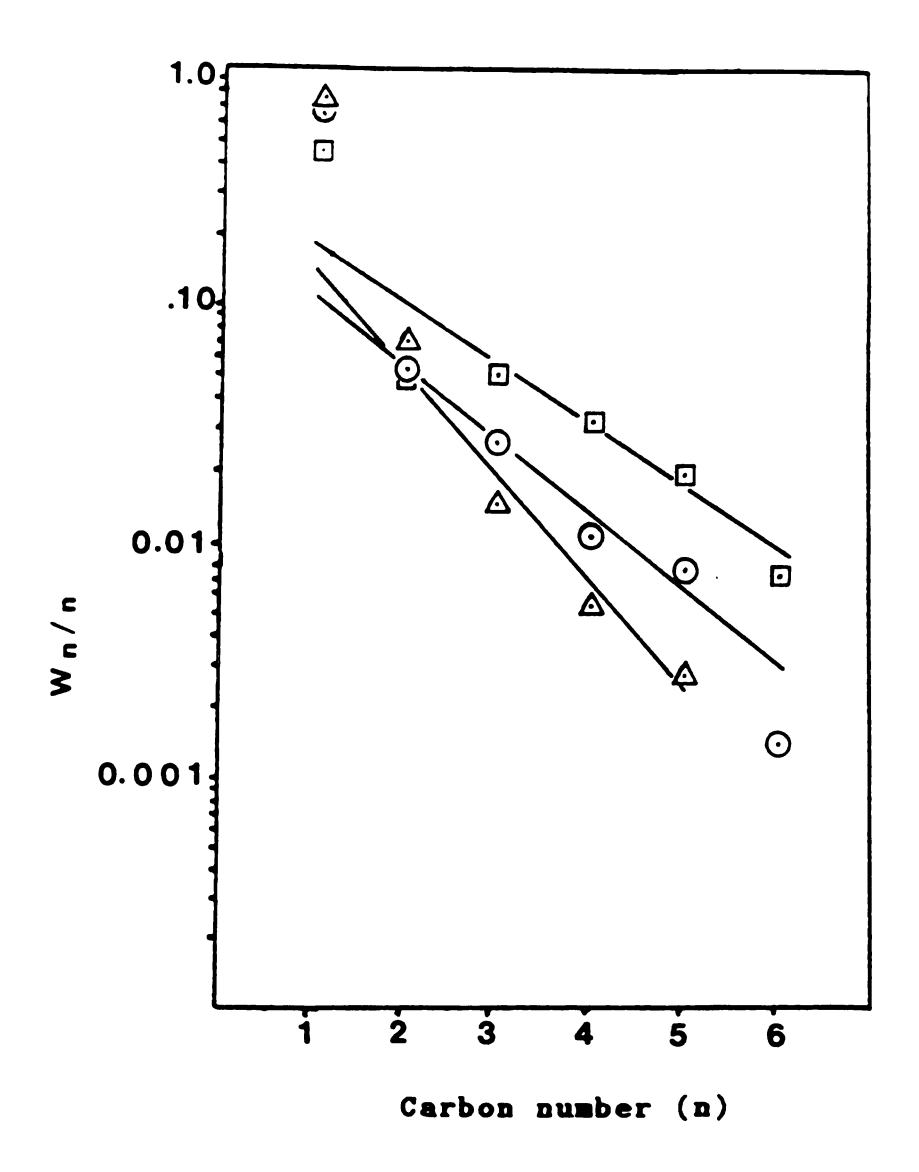


Figure 28. Comparison of Schulz-Flory plots for prereduced ⊙ and nonprereduced △ catalysts at 275°C. A prereduced catalyst run at 225°C gave the distribution shown by ⊡ . Reaction conditions: 1 atm., 300 hr⁻¹, 50 min. TOS.

metal precursors decompose at room temperature in air (or vacuum elevated temp.) to a form that can be represented as $[Ru(CO)_2(O-Al <)_2]_n$. This is also the species postulated by Giannelis (103) for Ru/APM at temperatures above 200°C in vacuum. It would seem reasonable then that the Ru microcrystallites formed by prereduction in hydrogen at 275°C and those formed without prereduction for Ru/APM at 275°C in H₂ and CO should be similar. Yet the fact that FT catalysis of prereduced and nonpreduced Ru/APM is significantly different suggests that the decomposition products of $[HRu_3(CO)_{12}]^+$ initially found within the micropores of APM are substantially different for these two catalyst treatments.

To investigate potential differences between prereduced and nonprereduced catalysts high resolution analytical electron microscopy was applied.

C. Electron Microscopy

In order for valid conclusions to be made regarding Ru crystallites observed by electron microscopy, potential sample artifacts induced by the electron beam had to be identified and eliminated. For this purpose freshly prepared Ru/APM samples that had not been run under catalytic conditions were examined. These studies showed that initially Ru microcrystallites were not clearly discernable on the APM support at magnifications up to 1 million times, in agreement with arguments stating that the microcrystallites formed from carbonyl precursor decomposition are less than

2 nm (150, 156-158). However, with time aggregation did occur in the electron beam and large Ru crystallites were found on the clay surface. Use of a liquid nitrogen cooled sample stage in the microscope though, very effectively minimized Ru aggregation as confirmed by additional studies using fresh Ru/APM samples. These studies are described in additional detail in Appendix A. Micrographs shown in throughout the rest of this text are taken from studies using the liquid nitrogen stage. Initial microscope studies of Ru/APM also revealed catalyst contamination by the feed gas (caused by iron and nickel carbonyl deposition) and confirmed the successful elimination of this contamination by appropriate purification procedures. This aspect of the research is presented in Appendix B.

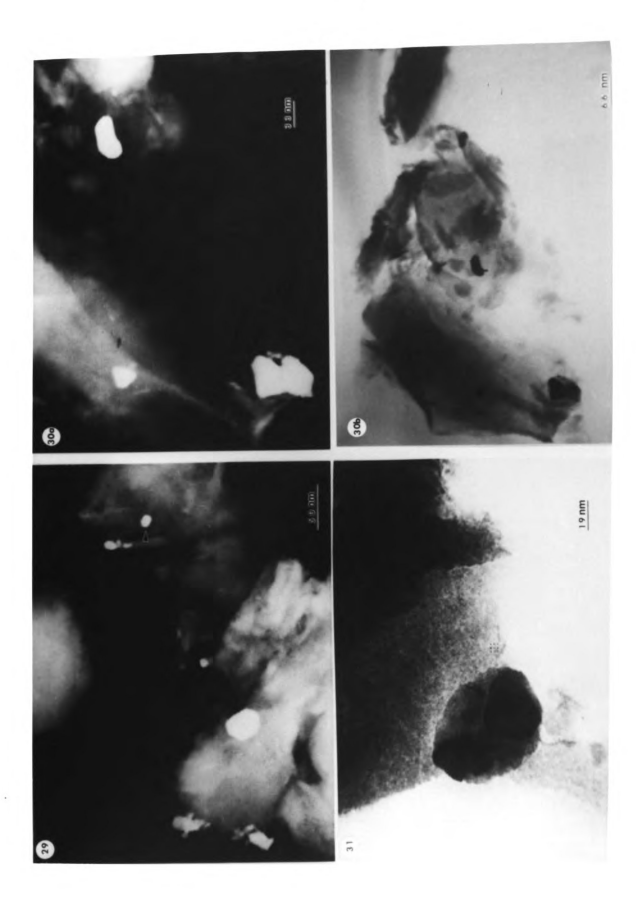
Representative STEM micrographs of nonprereduced catalysts (159) are shown in Figures 29-31. The large Ru crystallites present in micrographs are clearly evident as they exhibit markedly different form and contrast as compared to the diffuse image of the APM support. They are particularly distinguishable in dark field images.

The Ru crystallites observed in numerous micrographs of spent Ru/APM catalysts that were <u>not</u> prereduced occurred over a broad size distribution as shown in Figure 32. Formulas for the statistical averages of Ru particle sizes observed in numerous micrographs of these catalysts are given below.

Figure 29. Dark field image of Ru/APM catalyst after 30 hrs. of catalysis at 275°C showing Ru aggregates. The catalyst was not reduced prior to catalysis. Arrows indicate aggregate examined by the BDS analysis in Figure 33.

Figure 30. Dark (a) and bright field (b) images of the Ru/APM catalyst showing a coalesced Ru particle. Catalyst was <u>not</u> prereduced.

Figure 31. Twinned Ru aggregate on a Ru/APM postrun catalyst sample \underline{not} reduced prior to catalysis. The catalyst was run for 30 hrs. of FT catalysis.



Ru/APM not produced

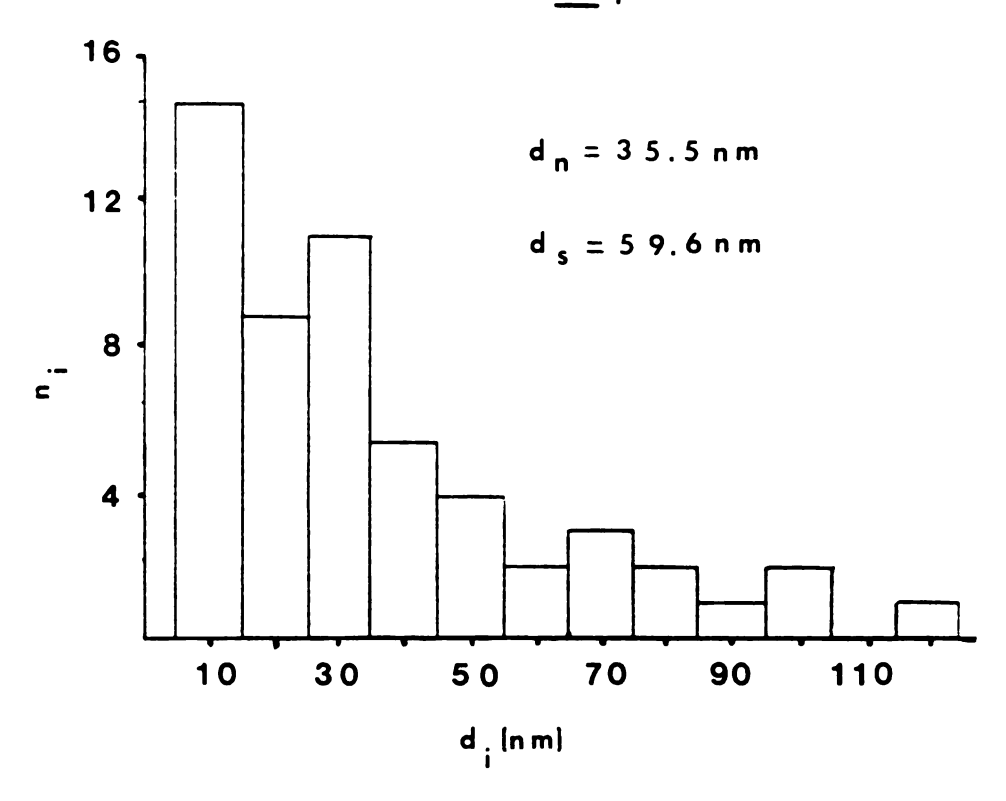


Figure 32. Ruthenium crystallite sizes observed by STRM for nonprereduced catalysts after 30 hrs. of FT reaction at 275°C. Here n_i is the number of particles with diameter d_i , d_n is the number average and d_s is the surface average particle size.

$$d_n = \frac{\sum n_i d_i}{\sum n_i}$$
 $d_s = \frac{\sum n_i d_i^3}{\sum n_i d_i^2}$

Here d_n is the number average, d_s is the surface average, and n; represents the number of metal particles of diameter d; (nm). The surface average size for nonprereduced catalysts is 59.6 nm. Based on the size, and contrast with the clay support, it is clear that these Ru particles are definitely located on the exterior surfaces of the pillared clay. This distribution shows that large crystallites were favored with nonprereduced catalysts as Ru particles less than 10 nm were not found. Metal particle coalescence is apparent in Figure 30 and multiple twinning of small crystallites is evident in Figure 31. These features are reminiscent of the crystallite migration model (160, 161) of metal sintering where large crystallites move across the support surface, collide, and merge into a single unit. The complicated geometries of multiply twinned particles result in surface sites that are unusual in catalyst particles, and may have particular importance in catalytic reactions that are dependent on surface crystallography (162, 163).

EDS microanalyses (Chapter II) were used in STEM investigations to confirm the identity of small microcrystallites, as the appearance of supported metals is a sensitive function of numerous microscope parameters. The representative EDS spectrum given in Figure 33 is from the

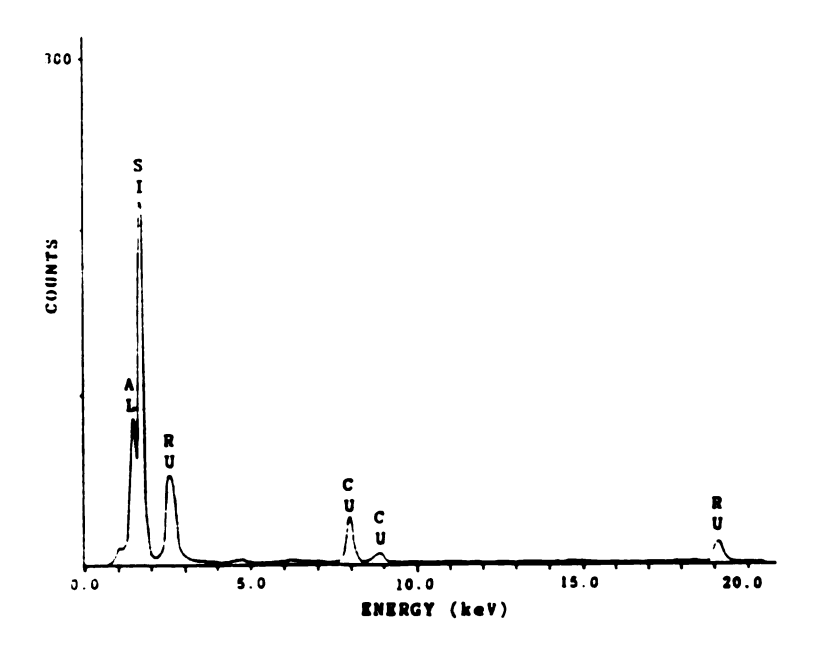


Figure 33. EDS spectrum from the Ru crystallite indicated in Figure 29. The Cu peaks are artifacts originating from the Cu microscope grids.

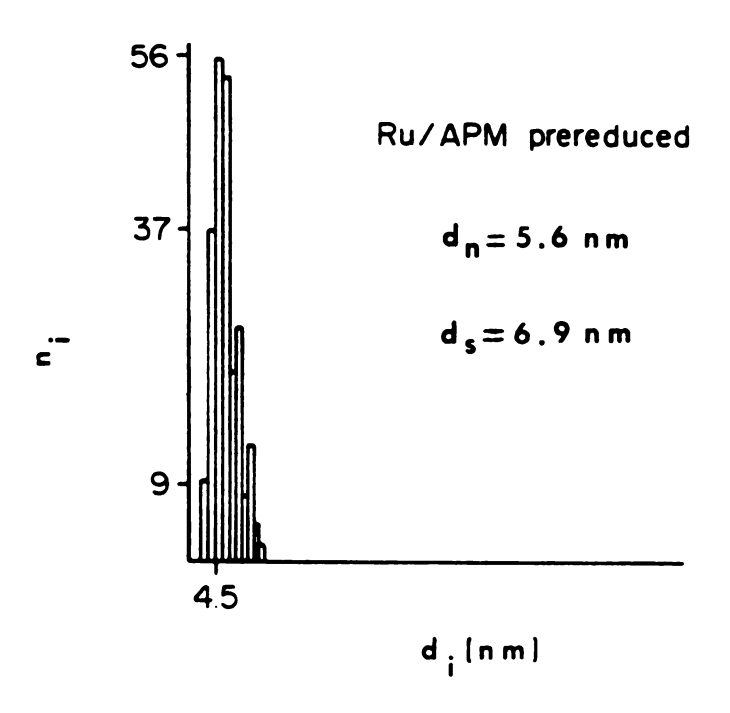
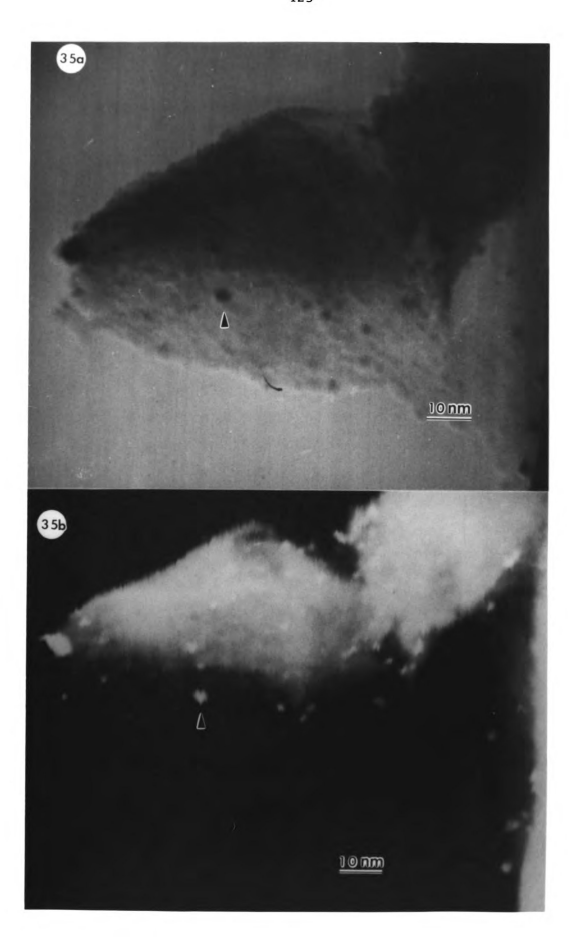


Figure 34. Ru crystallite sizes determined by STEM studies on numerous Ru/APM particles after 30 hrs. of reaction.

area indicated in Figure 29. It shows that this aggregate on the clay support consists of pure ruthenium. EDS showed that the occasional presence of Fe in spectra was due to the presence of iron in the clay structure, which is typically 0.01 wt% based on bulk elemental analyses. This iron did not migrate to the Ru aggregates as the iron intensity was always identical to spectra taken from neighboring regions without Ru aggregates.

STEM investigations, revealed however that the mean size of the Ru microcrystallites for prereduced catalysts was near 7 nm (Figure 32) nearly an order of magnitude smaller than catalysts not prereduced. Additionally, the distribution of particle sizes was nearly an order of magnitude narrower. Figure 35 illustrates these crystallites for a thin area of clay support. EDS analysis again confirms their identity and purity as illustrated in Figure 35c. The annular dark field image clearly distinguishes these microcrystallites from the support in thin areas but the contrast in thicker areas is greatly diminished due to increased scattering from the clay layers. The 10 nm crystallite at the tip of the clay support in Figure 35 clearly is on the surface or edge of the clay layers, however the number of Ru particles on the external surface is relatively small. Surely if microcrystallites as small as those imaged in Figure 35 were present on the surface they would have aggregated during FT catalysis. Most of the Ru is contained within the clay particles, as opposed

Figure 35. Representative <u>pre</u>reduced Ru/APM catalyst particle, found by STRM bright field (a), and dark field images (b), showing small Ru microcrystallites. A RDS microanalysis is given in Figure 35c. The catalyst was run for 30 hrs. of FT at 275°C and 1 atm.



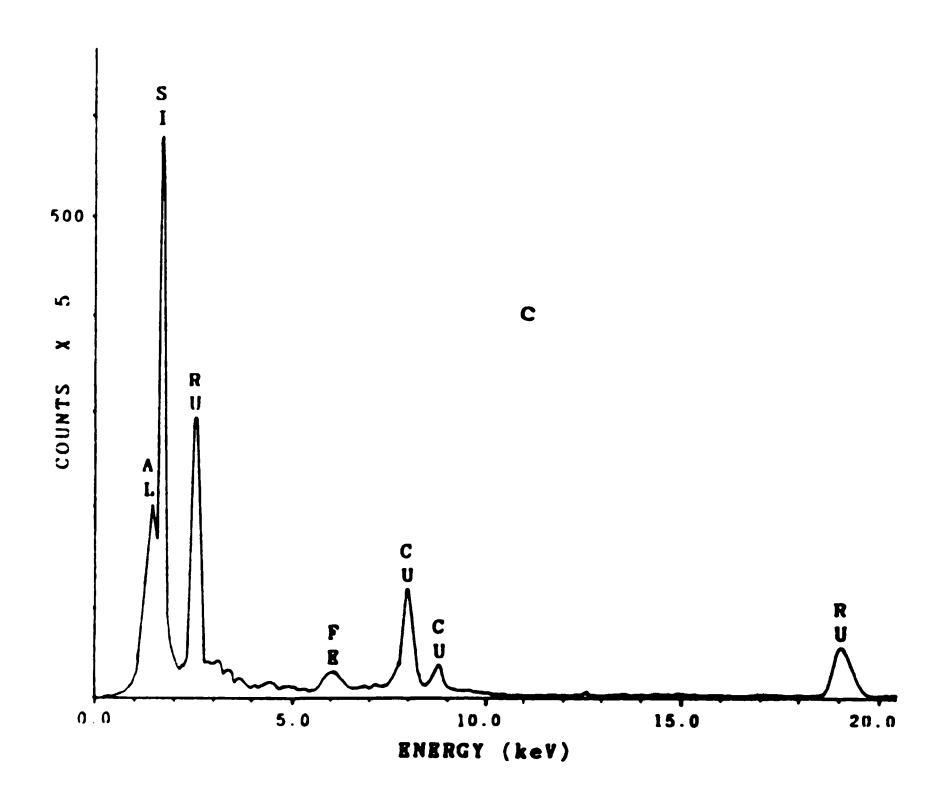


Figure 35c. KDS spectrum from the 5 nm microcrystallite indicated in Figure 35.

to the exterior dispersion observed for the catalyst which was not prereduced (Figures 29-31).

The observation that prereduction results in more efficient Ru dispersion, and that the majority of Ru crystallites appear to remain within the microporous APM support is significant. Clearly there is a marked difference in the Ru decomposition products obtained with prereduction versus nonprereduction. The relative degree of Ru migration and agglomeration as well as location is quite different with these two catalysts and may account for catalytic differences already discussed.

The sintering of supported metals is commmonly encountered in heterogeneous catalysis, thus the mechanisms, kinetics and measurement techniques of metal sintering have received considerable attention. Sintering, and the design of catalytic reactors to minimize it, has been reviewed recently by Lee and Ruckenstein (164). mechanisms account for the majority of phenomena observed, and the mechanisms can occur simultaneously or singularly. According to the crystallite theory (161), individual metal crystallites move across the support surface, and merge into larger crystallites when they come close. The features shown in Figure 30 of large Ru crystallites in the process of coalescing on the surface of APM, clearly shows that this process is occurring. The atom migration model (160) conversely explains that crystallite growth is caused by the diffusion of single atoms or small molecules on a

substrate. The formation of the small Ru microcrystallites on prereduced catalysts, and the migration of Ru from APM micropores, suggests that this mechanism is also operative in Ru/APM catalysts. Sintering is promoted by elevated reaction temperatures due to enhanced thermal motion of atoms, which makes the energy liberated by exothermic reactions (i.e. FT) especially important. Conversion was normally kept below 7% in this study to minimize such temperature affects.

Atom migration and sintering during reaction affects the metal dispersion, geometrical structure of the supported metal, and degree of electronic interaction with support. The conversion increase observed for nonprereduced catalysts is most likely due to the relatively rapid migration of highly dispersed Ru atoms into microcrystallites and eventually the large crystallites observed after 30 hrs. of reaction in the STEM studies. King (165) found that the specific activities for methanation and CO consumption increased monotomically with decreasing metal dispersion, which supports the conversion increase observed with Ru/APM. Kellner and Bell (96) studied 1.3 wt% Ru/Al₂O₃, prepared from Ru₃(CO)₁₂, in a glass microreactor capable of measuring synthesis activity and H2 chemisorption isotherms immediately following catalysis. They determined that as the dispersion fell from 0.9 to 0.6, due to Ru particle growth, the specific activity for hydrocarbon production (activity per exposed metal atom)

increased dramatically. The results of Ohukara et al. (166) further support this inverse relationship between specific activity and dispersion. They suggested, based on infrared evidence, that this is due to the increased relative concentration of the tightly bound, inactive diadsorbed CO mentioned earlier with smaller Ru particles. Although Ru/APM catalysts were run for 30 hrs. with reaction procedures different from these studies, for comparison the final dispersions of prereduced and nonprereduced catalysts would be 0.2 and 0.03, respectively (dispersion = 1/d(nm), from Figures 32 and 33, assuming spherical particles).

The probability of chain growth was independent of dispersion in the work of Okuhara et al., but Kellner and Bell found that it increased slightly with decreasing dispersion. The increase in α shown in Figure 28 for a non-prereduced catalyst agrees with this latter relationship. The increased selectivity for methanation with even longer run times does not. The lack of chain propagation at extended periods may be the result of the large crystallites, present in nonprereduced catalysts, oxidizing as they grow forming active sites that can only produce methane.

The decrease in SF deviations with time is certainly due to the relatively rapid migration of Ru for the nonprereduced catalysts. Whether the active site of nonprereduced catalysts was unusual in structure, or electronic interaction with the support is overshadowed by the fact

that with nonprereduced catalysts Ru readily vacates the micropores of the APM. The most important feature of the Ru/APM catalysts is that the ruthenium is selectively dispersed in micropores where the Bronsted acid sites responsible for the Ru₃(CO)₁₂ protonation are located. The loss of this distinguishing feature for nonprereduced catalysts makes them of diminished interest relative to the Ru microcrystallites retained within the micropores for prereduced catalysts.

The molecular weight distributions and chain growth probabilities afforded by prereduced Ru/APM catalysts are very similar to the above-mentioned studies with highly dispersed Ru on Al₂O₃. Very few deviations from SF were observed for prereduced Ru/APM, which is also consistent with the Ru/Al₂O₃ studies. These similarities suggest that prereduced Ru/APM is in fact very similar to Ru/Al2O3 and that no unusual deviations due to the steric confines of the micropores are observed, even at short run times. As mentioned in Chapter I, increased hydrocarbon chain length has a much smaller effect on the diffusivity of paraffins than that of branching. Chain limitation has been claimed as a characteristic feature of active sites confined in zeolite cages (Chapter I), yet these SF deviations usually are short-lived, because metal migration alters the initial active site. This is, of course, similar to what is observed here.

A few other points should be mentioned here concerning

the nature of the pillared clay support. The two-dimensional pores of pillared clays are less rigidly defined as they are the result of pillars placed between two-dimensional sheets, rather than the three-dimensional channel networks of zeolites. These pores are also not as well-ordered as their zeolite counterparts. When pillared clays are air dried on glass the layers stack parallel to the glass in a regular fashion for the most part. As they dry, surface tension forces associated with the evaporating water promote face to face interactions. Yet, occasional layer packing disorders introduce larger pores into the air dried structure than expected based on the gallery height from XRD.

We propose that the Ru microcrystallites, observed by electron microscopy, for prereduced samples are formed in interlayer voids created by layer packing disorders, and within the original clay gallery micropores. In this model, illustrated in Figure 36, the larger Ru particles in the range 2-6 nm are accommodated in the mesopores formed by imperfect packing between adjacent clay layers and by folding of the clay layers. On the other hand, the smaller Ru aggregates (≤ 2 nm) are of appropriate size to be accommodated in the galleries defined by the pillared clay layers. Additional support for this model is found in the pore size distribution shown in Figure 37, which was determined by nitrogen desorption isotherms at -196°C for the APM used in catalyst studies. Although the majority of the

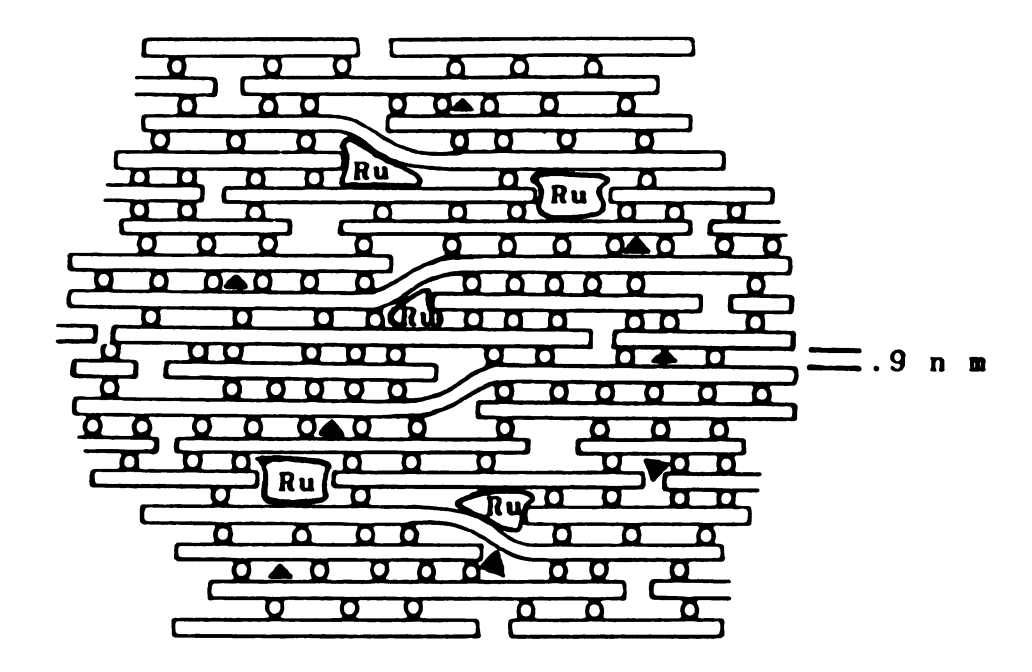


Figure 36. Model of air dried pillared clay showing mesopores created by layer packing disorders and layer bending. Plausible locations of Ru microcrystallites >2nm (labeled Ru), and less than 2nm (filled triangles) are indicated. Slabs represent clay layers and small open circles the "alumina" pillars.

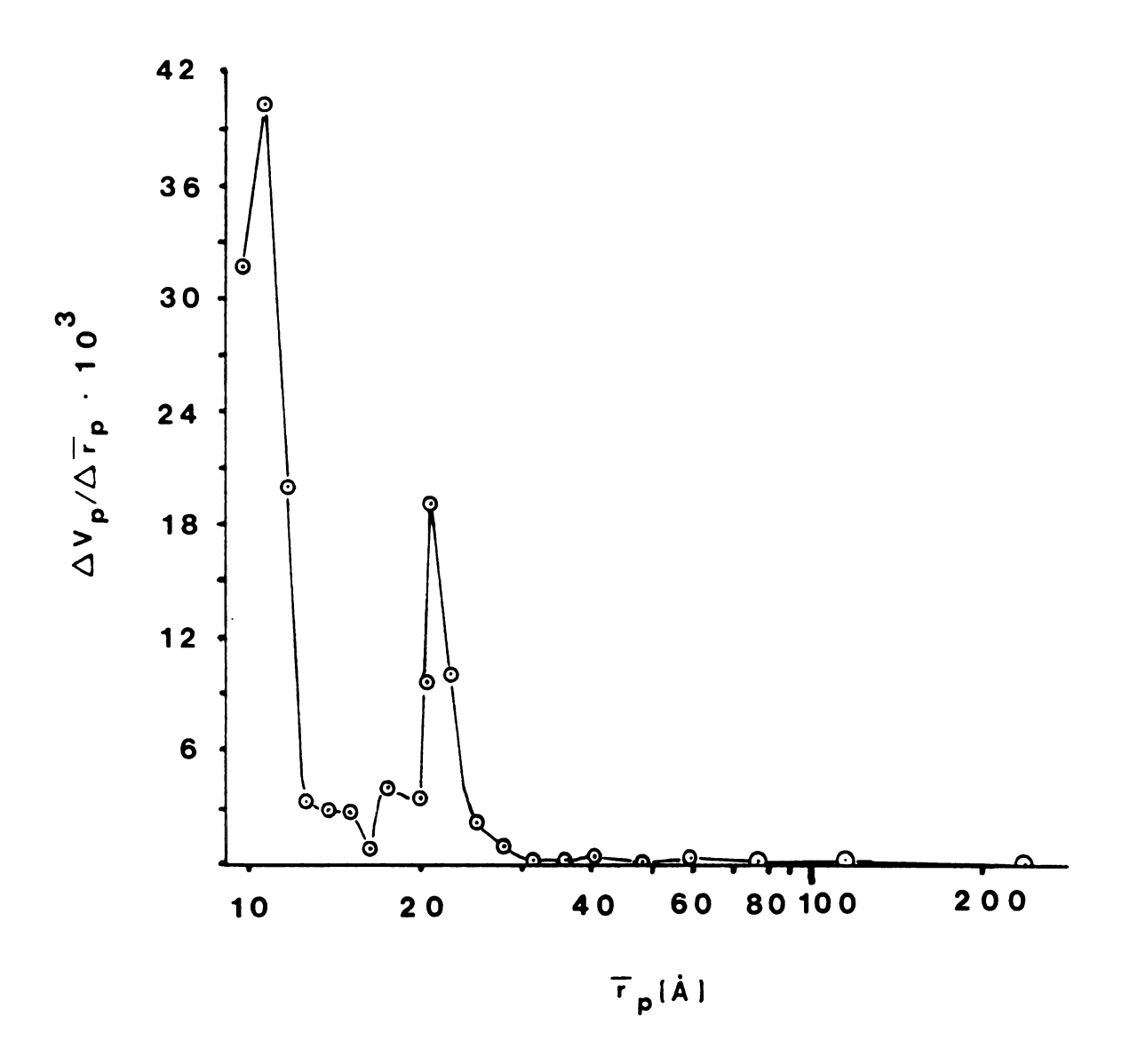


Figure 37. Pore size distribution of APM from liquid nitrogen desorption isotherms. Here \overline{r}_p is the mean pore radius, and $\triangle V_p$ is the change in pore volume.

pore volume is due to micropores with diameters near 20Å, mesopores with diameters near 40 Å are also present.

Apparently, reduction in hydrogen limits the migration of the ruthenium to these two regions of the microporous support. However, when the Ru/APM is not prereduced, Ru3(CO)12 may be formed and migrate to external surfaces where it decomposes and eventually Ru atoms aggregate into very large crystallites up to several hundred nm in diameter. Metal sintering on a support is dependent on the magnitude of surface interactions and chemical environment, among other factors. It is likely that the initial presence of CO in nonprereduced catalysts induces the formation of metal carbonyls which have enhanced volatility. Conversely, prereduction in hydrogen at elevated temperatures probably causes the formation of Ru microcrystallites within the micro- and mesopores. These microcrystallites may then be trapped within the support and not as mobile when CO is introduced for FT reactions. Goodwin et al. (167) found that a 3.8 wt% Ru/Al₂O₃ catalyst lost up to 40% of the metal when exposed to 1 atm. CO under flow conditions for 24 hrs and 200-265°C. They identified Ru(CO)₅ as the volatile species at 25°C and Ru₃(CO)₁₂ at temperatures above 200°C, by infrared characterization of a solvent trap. Clearly such a reversal of the original metal loading process would account for metal migration from micropores, transportation through the catalyst bed, and deposition and aggregation on clay surfaces.

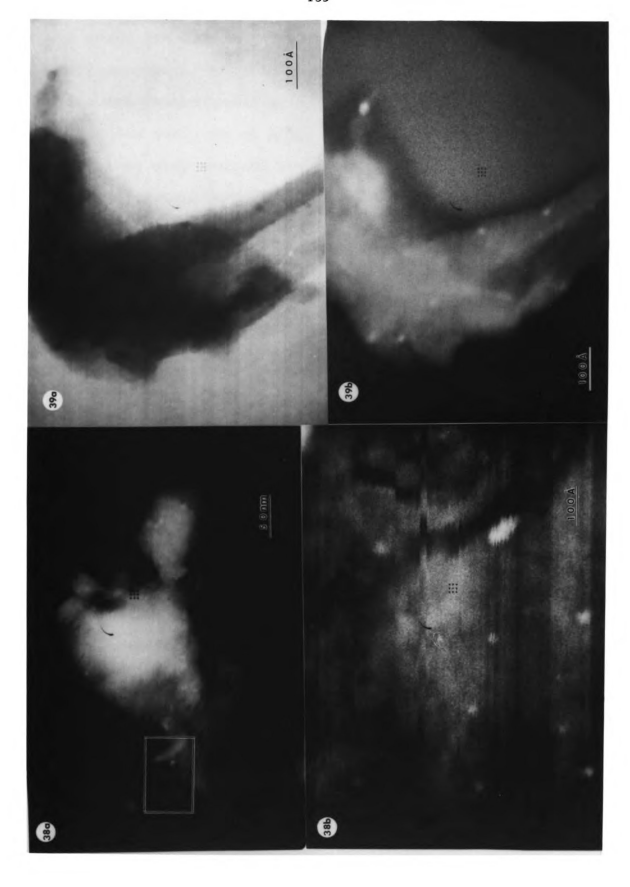
D. Nature of Ru microcrystallites.

Direct evidence for microcrystallites within thicker regions of the APM support would give evidence to the model stated above. The characterization of the nature of these microcrystallites would also provide useful information.

The identification of Ru microcrystallites > 5 nm is readily accomplished by dark field imaging, but thickness variations and electron scattering by the APM support diminish the effectiveness of dark field imaging for smaller microcrystallites. In many cases conventional bright field images lack sufficient contrast for positive identification of small, supported metal particles (168). The Z-contrast imaging technique (169) however, seems well suited for the detection of small metal crystallites and even atoms of high atomic number on light weight supports. This technique of electronically combining the elastic and inelastic signals recorded by the dark field detector and electron spectrometer, respectively, changes the dominant contrast mechanism forming the final image (169). The ratio or difference of these two signals supresses background variations due to variations in support thickness or electron source intensity so that detection of heavy atoms is enhanced. Figure 38 shows the improved contrast between Ru microcrystallites in the Z-contrast ratio image as compared with a normal dark field image. Aggregates less than 5 nm are evident in the Z-contrast image which are not discernable in the dark field image. Figure 39 compares a bright

Figure 38. Dark field (a) image of Ru/APM after catalysis. The area indicated in (a) is shown below in (b), using the Z-contrast ratio imaging technique, which shows microcrystallites < 5nm. Catalyst prereduced.

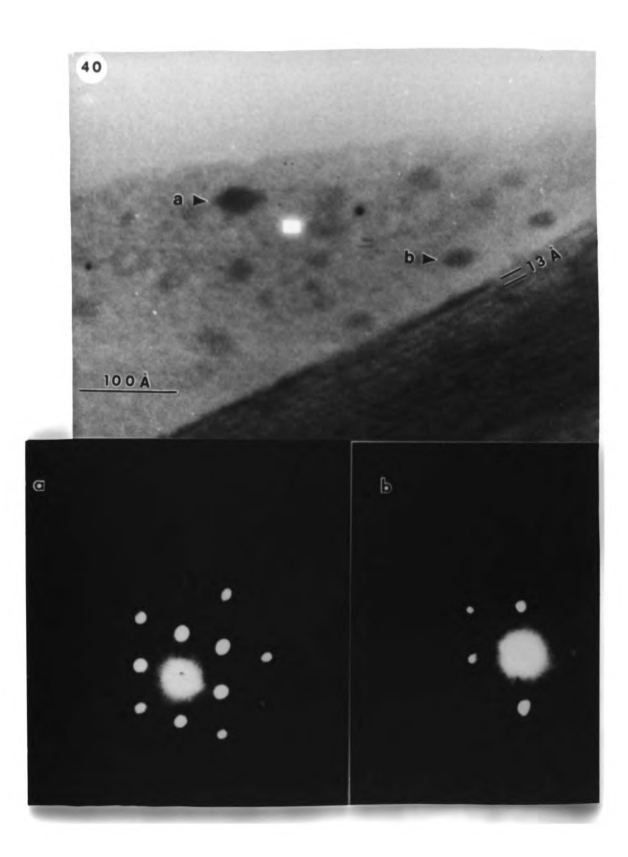
Figure 39. Bright field (a) and difference Z-contrast image (b) for a prereduced Ru/APM catalyst particle showing the ability of Z-contrast to image Ru in thicker clay regions.



field image and the Z-contrast difference image. Clearly, Z-contrast greatly simplifies the identification of the Ru domains and demonstrates Ru microcrystallites are present within thick sections of APM. The inelastic signal from the pillared clay support could not be completely subtracted in these studies because of the strong Bragg reflections from the support itself. Bragg reflections are known to contribute to the dark field signal in crystalline materials and to decrease the effectiveness of the Z-contrast technique (168).

A prereduced Ru/APM catalyst sample was examined at Arizona State University on a VG HB5 STEM to further explore Ru microcrystallite location and nature. Figure 40 exhibits a high resolution micrograph along with nanodiffraction patterns from the Ru crystallites indicated. The dark circle present in the diffraction patterns and in the bright field image results from a small mirror in the optical system which is capable of obtaining diffraction patterns of nanometer-sized crystals (170). The bright rectangle (BF image) is caused by the beam locater. patterns obtained reveal that the microcrystallites were indeed crystalline, in agreement with previous work for Ru/SiO2 catalysts (171). Figures 40b and 40c show pseudohexagonal diffraction patterns, similar to those obtained previously for Ru metal <011> and <121> zones, respectively (171). Although the diffuseness of the Ru aggregates in the image suggests that they may be located between clay

Figure 40. (a) STEM bright field image for prereduced APM following FT catalysis. Nanodiffraction patterns (b) and (c) are from the microcrystallites indicated. (Provided courtesy of J. M. Cowley, Arizona State University.



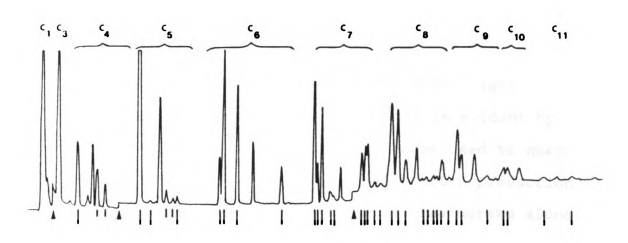
layers, the quality of small particle imaging is dependent on many factors, including defocus. The repeat distance of the fringes in the lower right in Figure 40a is approximately 1.3 nm. These fringes could be assigned as Moire fringes, yet their general agreement with the 1.8 nm XRD spacing of bulk APM samples prior to catalysis suggests that they are pillared clay lattice fringes instead. The magnification of Figure 40a was calibrated using experimental observation of carbon fringes. The fact that diffraction patterns corresponded to crystalline Ru metal is interesting as apparently a pure metal phase is formed by migration not an oxide or an aluminate.

E. Atypical Features of Ru/APM Fischer-Tropsch Catalysts

The high proportion of branched hydrocarbons and
internal olefins produced by prereduced Ru/APM are two
aspects of these catalysts that are uncommon in FischerTropsch chemistry.

Both of these anomalies are readily evident in the gas chromatograms (GC) obtained from catalytic runs. Representative GC traces are shown in Figure 41 for the gaseous and trapped liquid fractions. The chromatogram from the gaseous sample illustrates that branched hydrocarbons dominate the C_5^+ hydrocarbons, although branching is also present in C_4 products. Production of internal olefins is greatest for C_4 hydrocarbons. The chromatogram of the trapped liquid demonstrates internal olefin production for

а



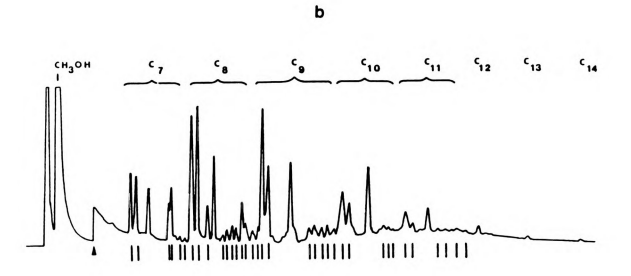


Figure 41. Representative gas chromatograms for prereduced Ru/APM catalysts showing production of branched (Long bars) and internal olefin (short bars) products. Chromatogram (a) is for the gaseous fraction, and (b) illustrates the components in the condensed liquid. Arrows indicate attenuation changes. (250°C, 190 psi, 2930 hr⁻¹, 200 min).

up to ${\rm C}_{10}$ hydrocarbons. The relative concentration of internal olefins is inversely related to branched hydrocarbon production as they decrease with higher hydrocarbon molecular weight.

The high production of methane and other light hydrocarbons relative to other components is evident by taking into account the attenuation changes used to keep the scale expanded. Additionally, hydrocarbon production to C_{13} should be pointed out in these chromatograms along with the relatively large MeOH production detected from the trapped liquid.

Figure 42 shows the variation of branched/straight chain (BC_n/SC_n) ratios on Ru/APM catalysts as a function of temperature. The production of branched hydrocarbons is clearly favored with higher reaction temperatures for Ru/APM although the relationship is not linear. The non-linearity suggests that this increased branched hydrocarbon production is affected by more than just the reaction temperature, as a direct relationship would show a simple activation energy dependence.

Branched hydrocarbon production in FT typically is minor compared to production of straight chain hydrocarbons. However, high pressure and low temperature favor branched hydrocarbon production on Co, Fe and Ni catalysts. In Schulz's (172) recent review on FT, he illustrated that branching selectivities were greatest for C₅ hydrocarbons on these metals and the product distribution for Ni showed

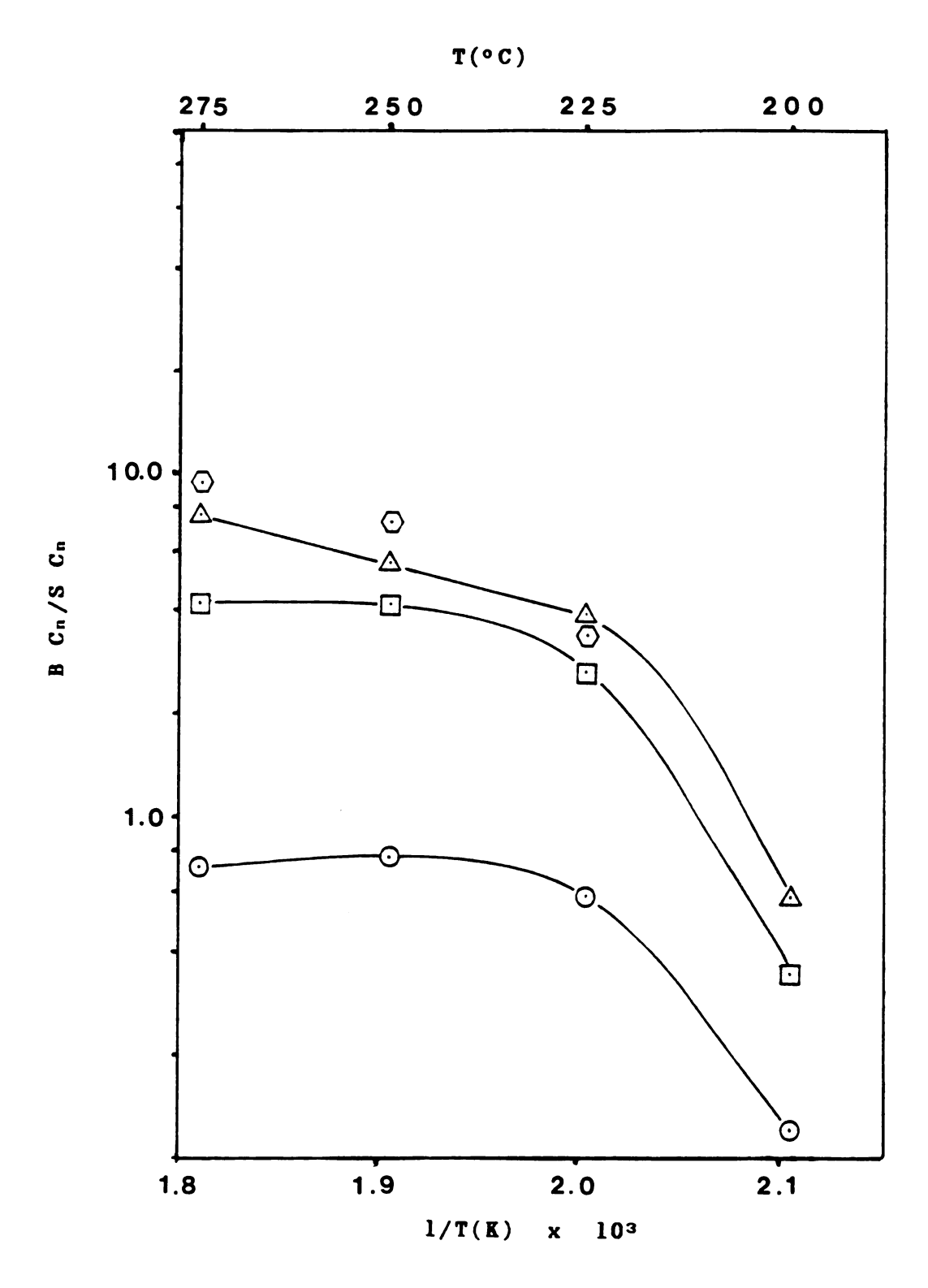


Figure 42. Variation of the branched/straight chain hydrocarbon selectivities with temperature for Ru/APM catalysts. The symbols represent C₄ \odot , C₅ \square , C₆ \triangle and C₇ \bigcirc hydrocarbon fractions. The FT conditions were; 120 psi., 1910 hr⁻¹, H₂/CO = 2, 50 min. TOS, prereduced.

30 mol.% branched C_n for Ni, and 12% for Fe. At these conditions branching can be very selective, occurring only in the 2 and 3 positions. This is probably due to steric demands for branching of small species which strongly favors fixation at terminal hydrocarbon positions.

Reports of hydrocarbon branching for supported ruthenium catalysts have been rare, and when branched products were observed (173) they were in much smaller concentrations than their straight chain counterparts. Exceptions to this have been observed for Ru dispersed on silica/alumina mixtures (165) and zeolite supports (165, 174-176). The proportion of branched hydrocarbons however, has not always been observed to increase with temperature as a variety of zeolite supported Ru catalysts showed isobutane selectivity to decrease with temperature (174).

Increases in reaction pressure are commonly associated with increases in CO conversion. To separate the effects that conversion may have on the branched hydrocarbon yields BC_n/SC_n ratios for a pressure study of Ru/APM were normalized with respect to conversion. The changes in this ratio for the numerous hydrocarbons produced are illustrated in Figure 43. The curves obtained demonstrate that branched hydrocarbons decreased relative to straight chain C_n with increasing pressure. This decrease was greatest between 15 psi (1 atm) and 70 psi, after which BC_n/SC_n were less sensitive to pressure variation. Maximum proportions of branched hydrocarbons were obtained in all cases for C_7

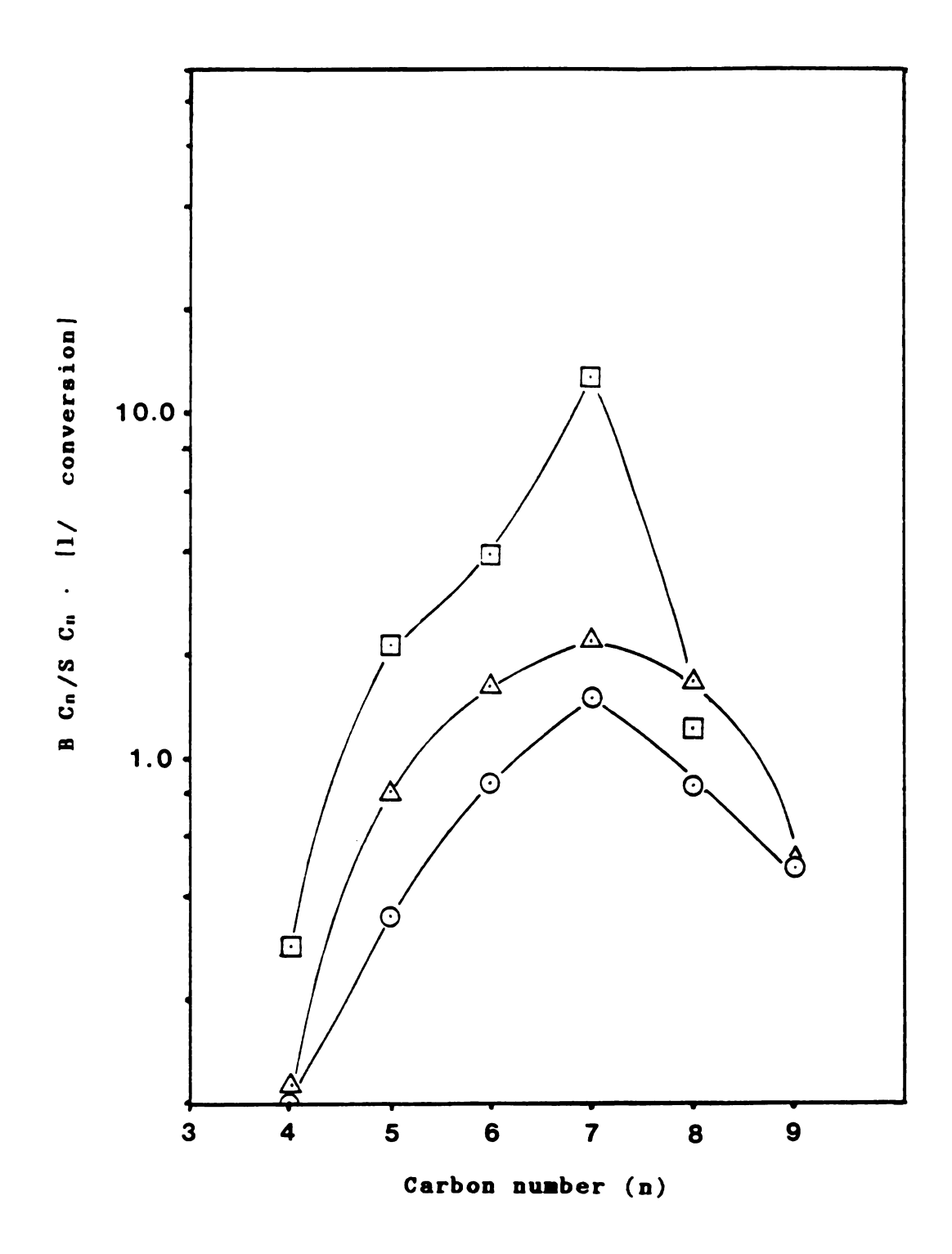


Figure 43. Change in the branched/straight hydrocarbon ratio, normalized for conversion variation, at various pressures. Here the Tepresent data at 1 atm.,

A at 70 psi, and Tepresent data at 1 atm.,

b at 70 psi, and termediate pressures follow these trends but are excluded for clarity.

hydrocarbons.

As branched hydrocarbon production reported for supported Ru catalysts has been sparse, the trend toward decreased branched hydrocarbon production with increasing pressure may be characteristic for APM as a Ru support.

Increased pressures would increase the concentration of the intermediate responsible for branched hydrocarbon production, yet it is plausible that these intermediates may be consumed by a competing reaction favored at elevated pressures.

The propensity for production of C7 branched hydrocarbons compared to lighter and heavier fractions is of interest as industrial reforming reactions strive to achieve high proportions of branched products in the gasoline range due to increased octane ratings. An examination of longer run times reveals that this selectivity is maintained (Figures 44 and 45). Comparison with the first BC_n/SC_n versus 1/temperature plot (Figure 42) shows that although these ratios decrease with carbon number, the greatest branched/straight chain ratios are obtained for C7 and C6 hydrocarbons. These figures demonstrate that the selectivity of C₇ and C₆ branched hydrocarbons is stable with longer run times and represents a significant departure for Ru/APM catalysts compared to typical supported Ru cata-It should also be noted that isobutane fractions decrease with higher temperatures at longer reaction times contrary to the results at 50 minutes. This relationship

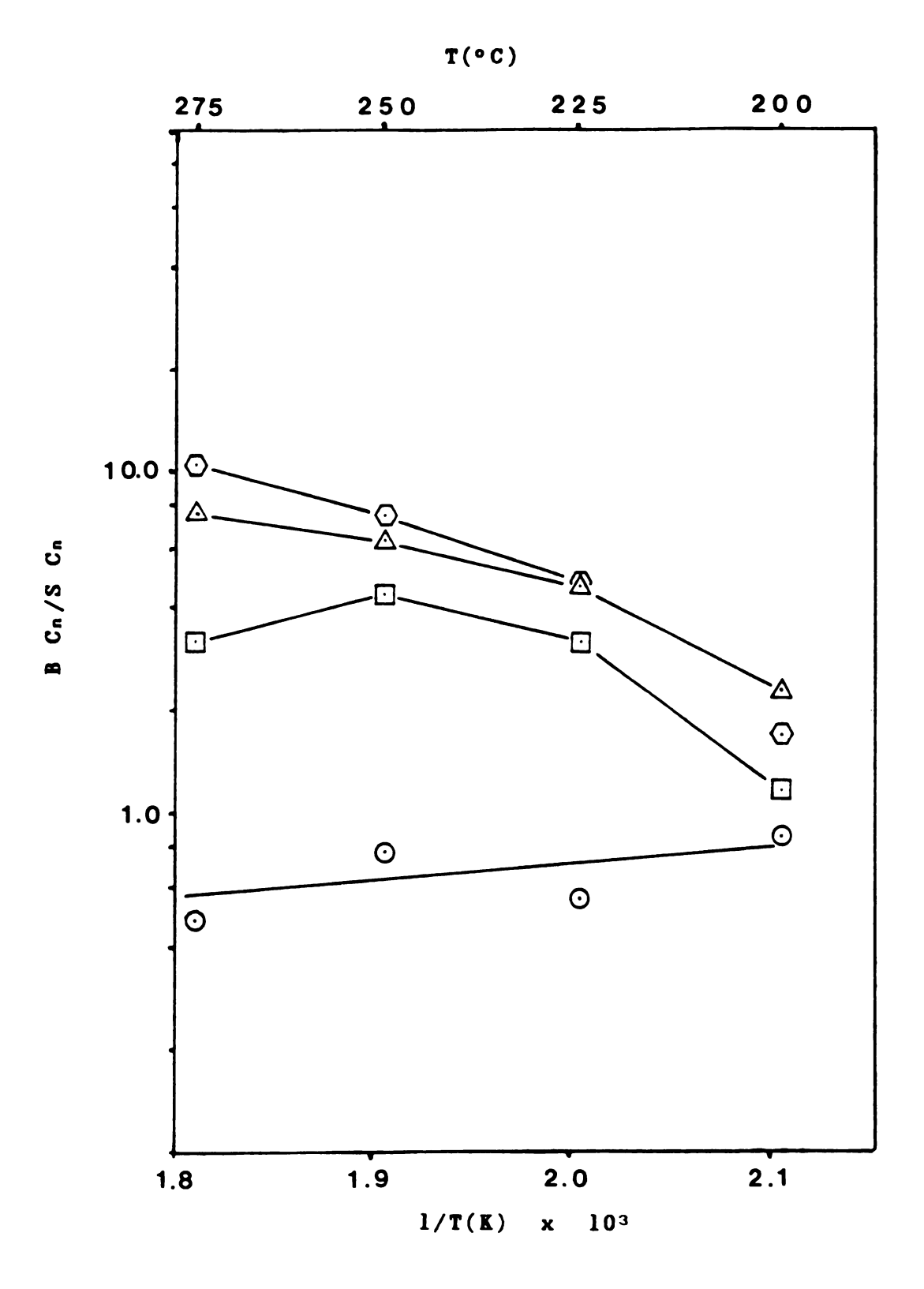


Figure 44. Production of Branched/ straight hydrocarbons at longer run times (100 min.) for C_4 \odot , C_5 \boxdot C_6 \triangle , and C_7 \bigodot hydrocarbons. Pressure 1 atm. Run conditions were the same as in Figure 42.

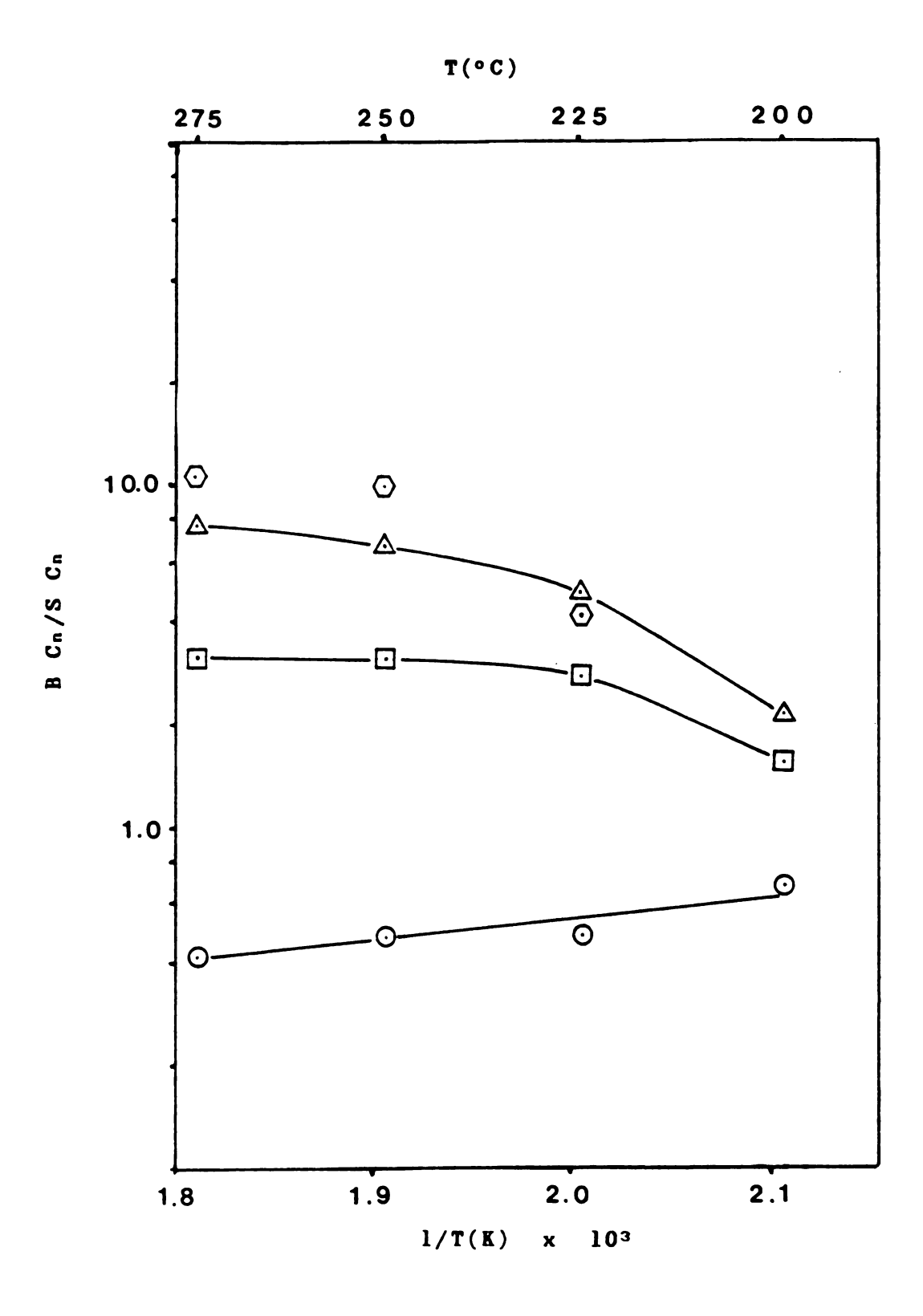


Figure 45. Steady state (200 min.) selectivity for branched hydrocarbons for $C_4\odot$, $C_5\odot$, $C_6\bigtriangleup$, and $C_7\odot$ products. Run conditions were the same as in Figure 42.

is consistent with the earlier mentioned trend for Ru/zeolites (174) that originally appeared contradictory to Ru/APM results.

The fact that branched hydrocarbons are not normally produced in FT has led several authors (165, 174-176) to propose that the acidic nature of supports such as silica alumina mixtures or zeolites are responsible for hydrocarbon branching. King (165) found that a mechanical mixture of Ru/Al₂O₃ with an ultrastable zeolite gave products rich in isobutane and isopentane, whereas the Ru/Al₂O₃ catalyst alone gave only minor branched products. This strongly suggests that isomerization of primary FT hydrocarbons occurs subsequent to initial FT production and that this could take place downstream of the original active site. If this is the case the production of secondary, branched products should be affected by the feed gas velocity.

Figure 46 shows the result of a study on BC_n/SC_n ratios for Ru/APM catalysts run at different flow rates. The Ru/APM catalyst was run at the gas hourly space velocity (GHSV, V/V/h) of 2700 hr⁻¹ for 3 hrs at 275°C. This allowed steady-state hydrocarbon production to be achieved before the flow was increased and equilibrated at each flow rate for 45 min. After the data points were collected for various flow rates the flow was returned to the original values and equilibrated for 45 min so that an estimate of the effect of cycling could be obtained. The decreasing

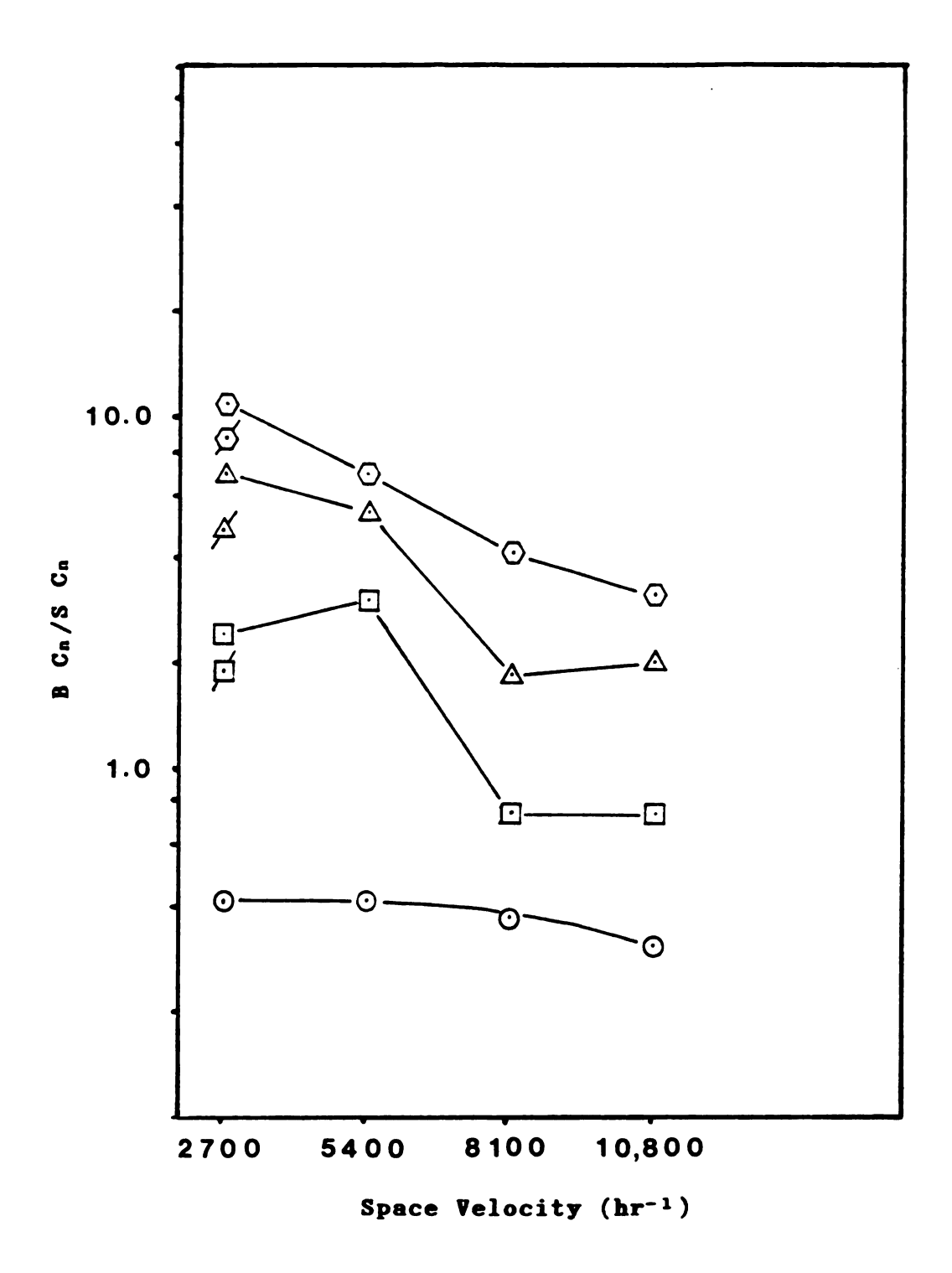


Figure 46. Effect of space velocity on the branched/
straight ratio. The C₄ hydrocarbons are represented by ⊙,
C₅ by ⊡, C₆ by △, and C₇ are shown by ⊙. The
slashed symbols show the ratio when the flow was returned to
the original value. (275°C, 110 psi, H₂/CO = 2, 45 min.
TOS, prereduced, contact time from 1.3-0.33 seconds).

production of branched relative to straight chain products with increasing flow rate is clearly evident. The magnitude of this effect was greatest for the heavier hydrocarbons (C_6 , C_7) and decreased for lighter branched products.

A number of factors may influence the BC_n/SC_n ratios as the flow rate is increased including: conversion, residence time and diffusivity of individual hydrocarbon components in the microporous APM, flux of product molecules at the catalyst surface and location of sites responsible for isomerization. We would be remiss at this point if we did not point out the complexity associated with these factors, which are coupled with the complicated kinetics, and mechanism of FT. A simple, yet plausible, explanation would be that the decreasing diffusivities of higher molecular weight hydrocarbons would inhibit diffusion of molecules such as 1-heptene back into micropores once it has left the APM interior, relative to say 1butene. Increasing flow rates would magnify such differences as the alkene intermediates are pushed through the catalyst bed with a higher velocity and reaction of molecules with lower diffusivities would become diffusion limited.

The relationship between the ratio of internal olefins to terminal olefins with reaction temperature is shown in Figure 47. This ratio decreases with increasing temperature as does the ratio of internal olefins/straight chain

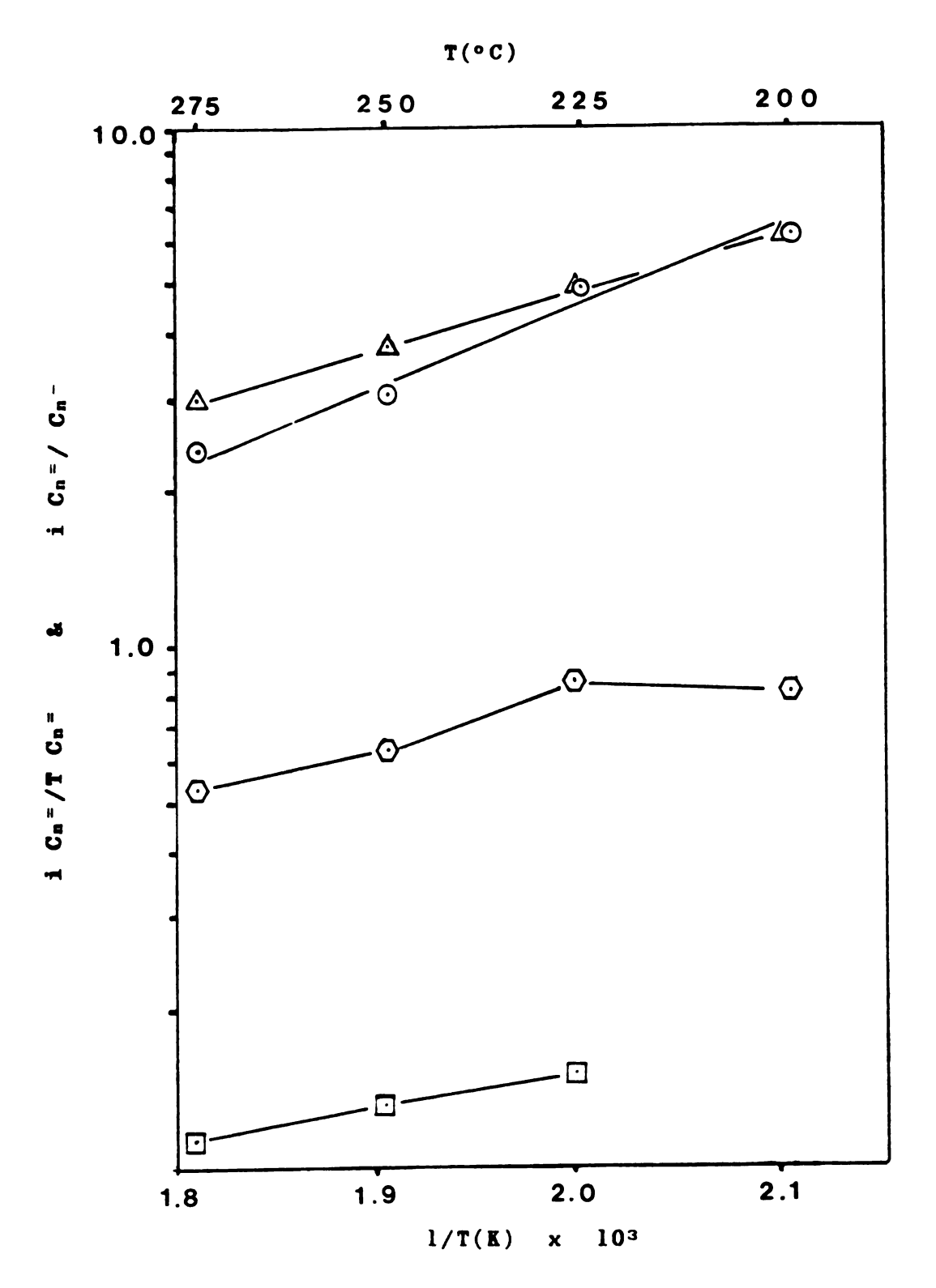


Figure 47. Production of internal olefins relative to terminal olefins (i $C_n=/T$ $C_n=$), and n-alkanes (i $C_n=/C_n=$) as a function of temperature. Here the symbols are defined as; iC₄=/TC₄= is \odot , iC₄=/C₄- \odot , iC₅=/TC₅= \triangle , and iC₅=/C₅- is \odot . Conditions were 120 psi., 1910 hr⁻¹, H₂/C0=2, 50 min. TOS, prereduced.

hydrocarbons. The proportionally smaller production of C₅ internal olefins is also evident from this plot. Kellner and Bell (173) found that olefins exhibited a higher activation energy for formation than paraffins (about 6 kcal/mole), indicating greater olefin production should occur with elevated temperatures. Their experiments revealed however, that above 215°C the olefin to paraffin ratio decreased, and they attributed this to increased hydrogenation. This would also explain the observed decrease with Ru/APM catalysts.

The internal olefin production versus terminal olefin hydrocarbon ratios were essentially invariant with respect to pressure. When the sum of all alkenes (including branched olefins) was compared with the total alkane production and normalized for the different conversions obtained with the pressure study, the plot of Figure 48 was obtained. The relative position of these curves suggests that the total olefin yield relative to paraffins generally increased with pressure. Although this might be due to the increased conversion obtained with greater pressure these plots were normalized with respect to conversion and separate plots of alkene/alkanes versus conversion did not show a significant correlation between these two parameters. The dip in C_n^{-}/C_n^{-} for C_4-C_6 hydrocarbons may be due to enhanced olefin hydrogenation with the longer residence times expected for higher molecular weight hydrocarbons. The increase beyond C₆ hydrocarbons however is not

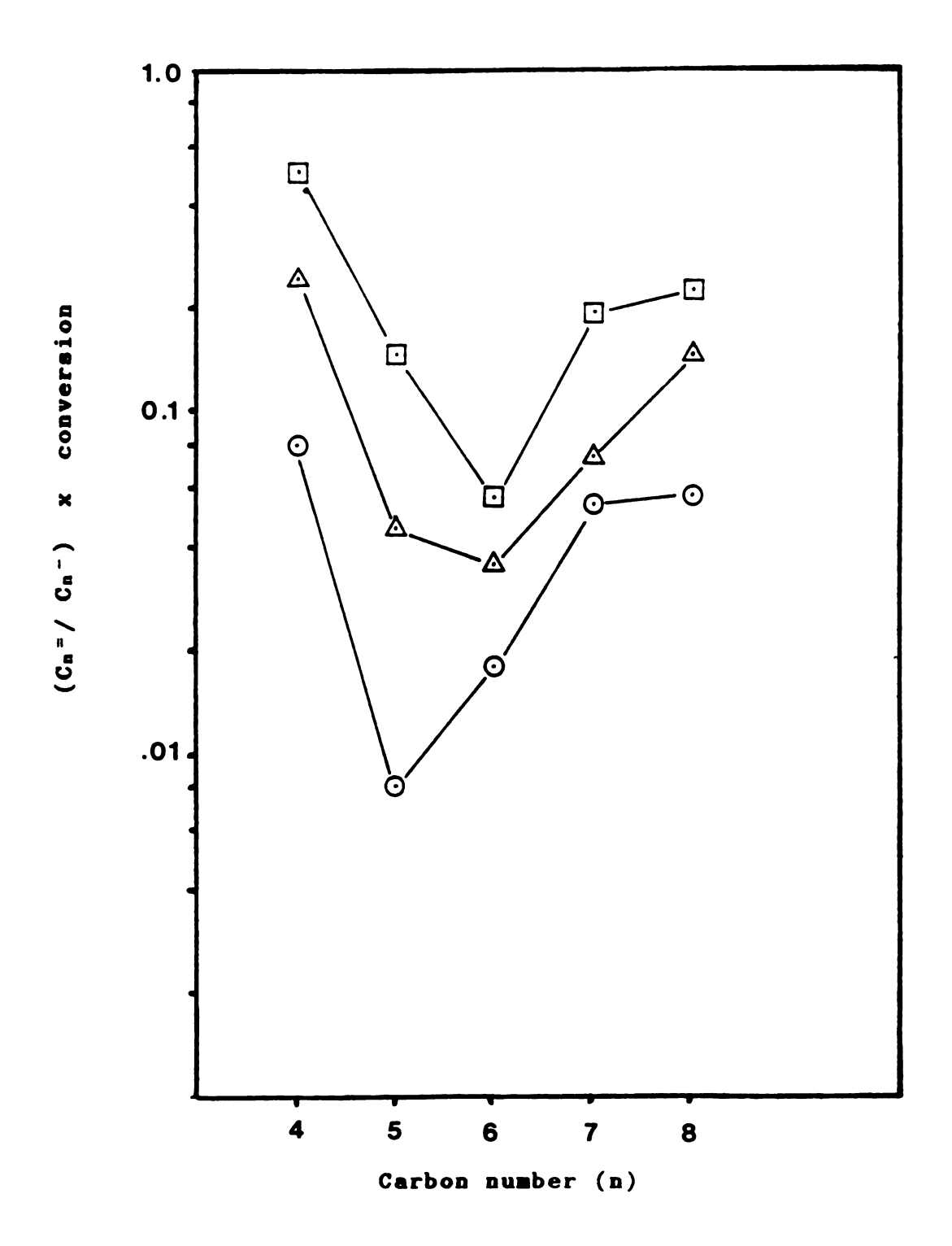


Figure 48. Comparison of total alkene/alkane, normalized with respect to conversion, for 1 atm. \odot , 70 psi \triangle , and 190 psi \square . FT conditions were; 250°C, 1910 hr⁻¹, H₂/CO=2, 50 min. TOS, prereduced.

explainable by this reasoning.

The ratio of alkenes to alkanes determined from the flow rate study, previously described for branching, is given in Figure 49. The trends for C_4 , C_5 and C_6 hydrocarbons all show increased olefin production with increased space velocity. Yet, the trends are not smooth and a few deviations from these trends are evident. A return to the original flow rate followed by 45 min of equilibration showed only slightly higher C_n^-/C_n^- ratios than obtained originally. A breakdown of these olefins into iC_n^-/TC_n^- and iC_n^-/C_n^- ratios is given in Figure 50. The iC_n^-/TC_n^- ratios do not correlate well with the increased flow rates but the iC_n^-/C_n^- ratios for C_5 and C_4 do exhibit a regular dependence on space velocity.

The dependence of C_n^-/C_n^- on flow rate is closely re lated however to conversion, as conversion also decreased steadily with increased flow rates for Ru/APM catalysts. This dependence is supported by previous studies on supported Ru catalysts (165,174,177) which all showed the C_n^-/C_n^- ratio to decrease with increased conversion. With increased conversion greater incorporation of light olefins into growing hydrocarbon chains is expected.

F. Isomerization Mechanisms

The acidity of APM clays is well documented, and the involvement of this acidity in isomerization of FT products to branched paraffins and internal olefins is supported by studies relating acidity to these unusual features. Olefin

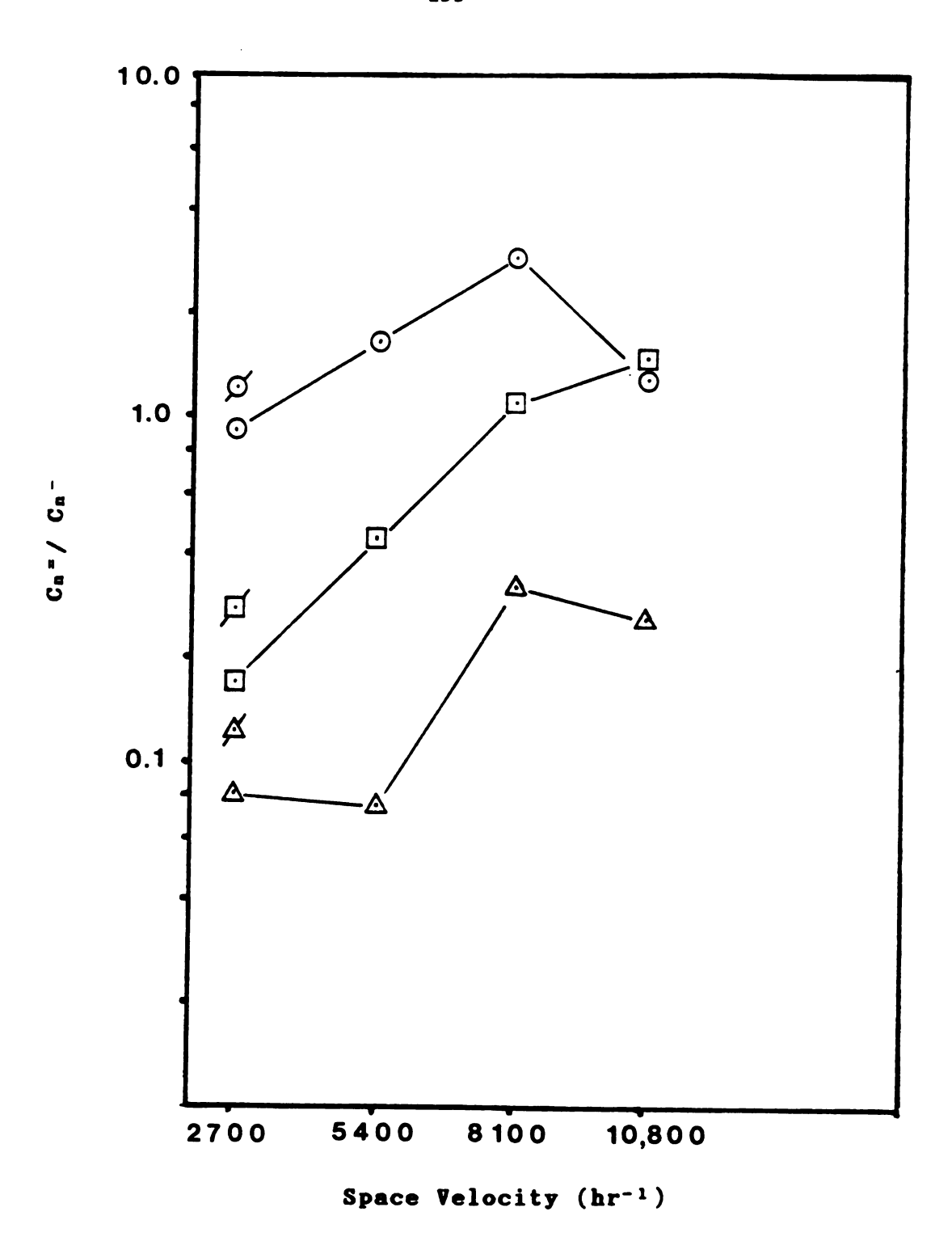
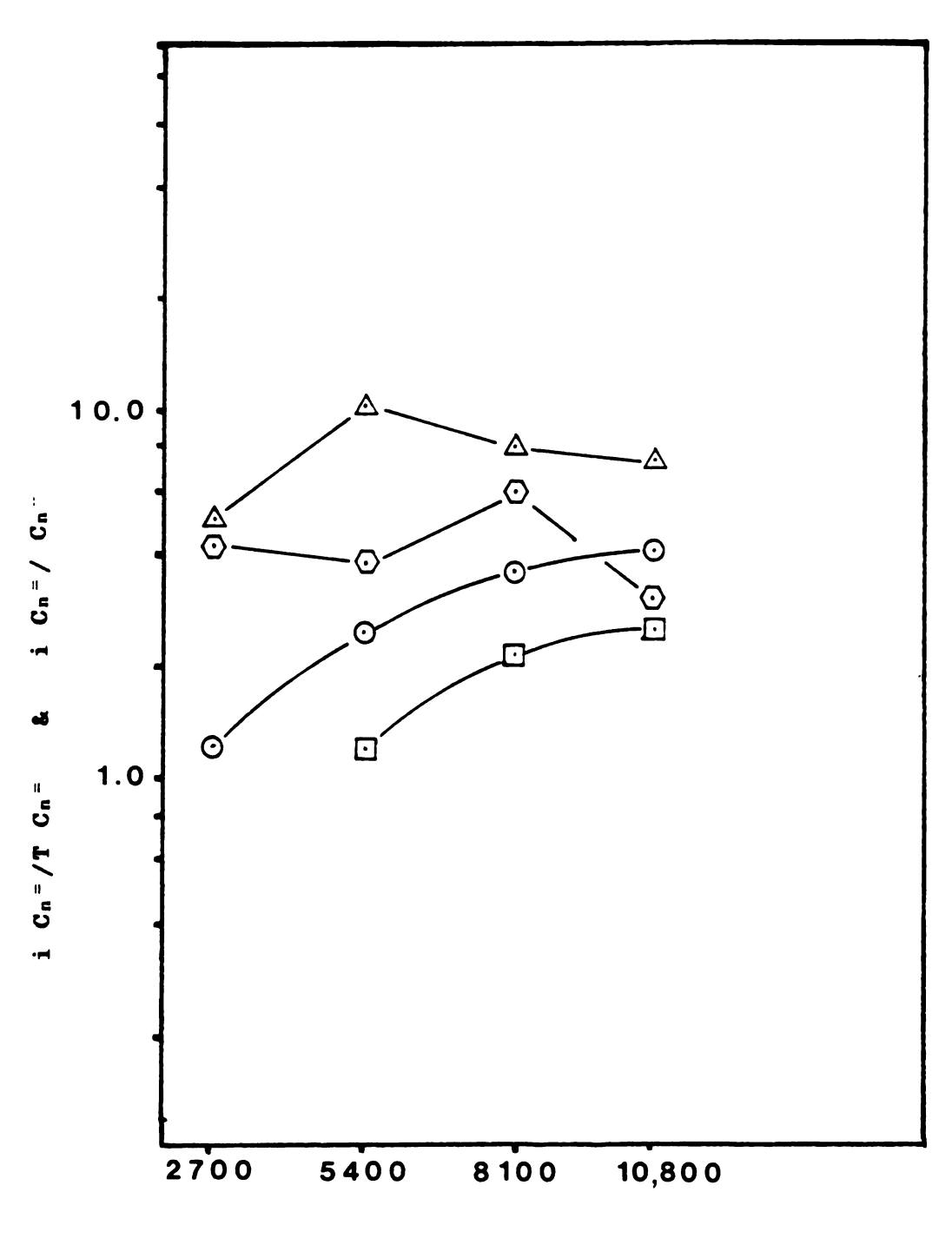


Figure 49. Ratio of alkenes to alkanes for Ru/APM catalysts as a function of flow rate. The symbols show C_4 \odot , C_5 \odot and C_6 \triangle hydrocarbons. The slashed symbols show the recycle values. Conditions were 275°C, 110 psi., $H_2/C0=2$, 45 min. TOS, contact time from 1.3-0.33 seconds.



Space Velocity (hr^{-1})

Figure 50. Yields of internal olefins relative to 1-alkenes and n-alkanes as a function of flow rate. Symbols are; $iC_4=/l-C_4=$ \odot , $iC_4=/l-C_5=$ \odot and $iC_5=/l-C_5=$ \odot (275°C, 110 psi., $H_2/l-C_5=$ 45 min. TOS, 1.3-0.33 sec. contact time).

isomerization reactions occur readily on acid catalysts. The relative strength of acid sites required for these carbonium ion reactions increases in this order: cis-trans isomerization < branching < alkylation (12). Skeletal isomerization of alkanes is more difficult than that of corresponding alkenes and high temperatures or strongly acidic sites are needed, but the presence of traces of olefins markedly accelerates this reaction as they are readily protonated to form carbonium ions (13).

The relevance of support acidity was indicated by King's study (165) where it was determined that the Si/Al ratio of silica-alumina mixtures and zeolite supports appeared to be important in affecting enhanced yields of branched products. Results from Chen et al. (175) added additional support for the influence of Si/Al ratios on branching selectivities when zeolites were exchanged with $Ru(NH_3)_5^{3+}$. Yet when these same zeolites were prepared using vapor impregnation of ruthenium carbonyls at the identical dispersion and Si/Al. No isobutane was obtained. Thus the Si/Al ratio does not directly determine the isobutane yield. They suggested that greater Si/Al ratios increased the acid strength of the OH groups formed within the zeolite support when the cluster decomposed during calcination (ie. the formation of 3H⁺/Ru³⁺). Thus the presence of these Bronsted acid sites may initiate branching of primary FT products, creating bifunctional catalyst properties.

It is also plausible that the changing strength of the Si/Al ratio may induce hydrogen suppression of neighboring Ru crystallites (178). Nearly a monolayer of hydrogen is adsorbed on Ru surfaces during catalysis (179) and alteration of this hydrogen concentration could effect chain growth, hydrogenation and hydrocarbon isomerization.

A number of mechanisms have been proposed to account for hydrocarbon branching in FT, the most illustrative ones are depicted in Figure 51. The incorporation of propene in growing alkyl chains was postulated based on 14C experiments for the normal pressure cobalt synthesis, yet this has not been supported by additional experiments (71). addition of a methyl species into chemisorbed growing chains, and isomerization of fixed chains has also been cited as possible mechanisms (172). The formation and rearrangement of a alkylidiene species has also been suggested as a intermediate responsible for branching (127). Decreases in hydrogen concentration would enhance chain branching according to this mechanism. This mechanism was supported by the finding that K promoted Fe₂O₃ catalysts produced branching whereas unpromoted catalysts gave no branched hydrocarbons. They also noted that K promotion increases CO adsorption and decreases ${\rm H_2}$ adsorption. A mechanism involving olefin protonation and rearrangement through a carbonium intermediate would also account for the observed results. Although there would be a significant difference between branching and nonbranching

(a)
$$RCH_2$$
 $+$ $CH_2CH = CH_2$ $RCH_2 - CH - CH_2$

(b) RCH CH_3 RCH_2 CH_3

(c) RCH_2CH_2 RCH_3 CH_3 CH_2 CH_2 CH_2 CH_2 CH_2 CH_2 CH_2 CH_2 CH_2 CH_3 CH_3 CH_4 CH_5 CH_5 CH_6 CH_7 CH_8 CH_8 CH_8 CH_8 CH_9 CH

Figure 51. Plausible mechanisms to account for hydrocarbon branching showing: (a) insertion of propene, (b) addition of chemisorbed methyl species, (c) isomerization associated with hydride shift, (d) formation and rearrangement of an alkylidiene, (e) carbocation rearrangements.

rearrangements in such a mechanism the high acid strength in clay interlayers (chapter I) and the high concentration of acid sites within micropores could account for the branching propensity of APM. The isomerization of terminal olefins could take place on these acid sites also as illustrated below:

Silica is known to be a good isomerization catalyst and experiments with precipitated iron on silica catalysts showed that as the silica content in a catalyst series increased so did the production of internal olefins relative to 1-olefins (180). This was interpreted as evidence that most of the internal olefins were produced by isomerization of 1-olefins.

Based on the relevance of these mechanistic arguments to the selectivity of branched and isomerized products on Ru/APM, additional experiments were conducted with the addition of alkene probe molecules, and variation of $\rm H_2/CO$ ratio.

G. Alkene Probe Addition, and H_2/CO /Variation.

In the first experiment a known concentration of C_2 - C_6 olefins (in He) was added to a Ru/APM catalyst that had been run in FT synthesis for 3 hrs at 120 psi and 275 $^{\circ}$ C to achieve steady state conditions. The relationship between the masses of the alkene standard added was C_2 4.2, C_3

6.5, C_4 = 9.3, C_5 = .9, C_6 = 1.0. The concentration of alkenes added in the first step of this experiment was roughly similar to that of total hydrocarbons produced for each C_n and the second concentration corresponded to twice this concentration. To achieve this higher concentration the flow of alkenes relative to CO feed was altered (total flow kept constant.

Figure 52 shows the distribution of hydrocarbon products detected relative to methane for the FT production before alkene additions, along with those after 40 min of eqilibration with each alkene concentration. The distributions obtained form the alkene additions parallel each other closely, but some differences are evident relative to the initial FT distribution. Even though the concentration of alkenes added increased as $C_4^{=>}$ $C_3^{=>}$ $C_2^{=>}$, the concentration of $C_4^{=>}$ >> $(C_5^{=>}$, $C_6^{=>}$) should give greatly decreased hydrocarbon production for > C_4 hydrocarbons. Yet, C_5 and C_6 hydrocarbons continued to increase relative to the steady state FT distribution shows that production of C_7 , C_8 and C_9 hydrocarbons was also increased by these alkene additions.

Figure 53 indicates the mass of olefins incorporated for branched and straight chain hydrocarbons relative again to the steady state SF production. From this plot it is clear that straight chain hydrocarbons showed increasing production in the order $C_6 > C_5 > C_4$, but production of hydrocarbons $> C_6$ actually decreased slightly for both

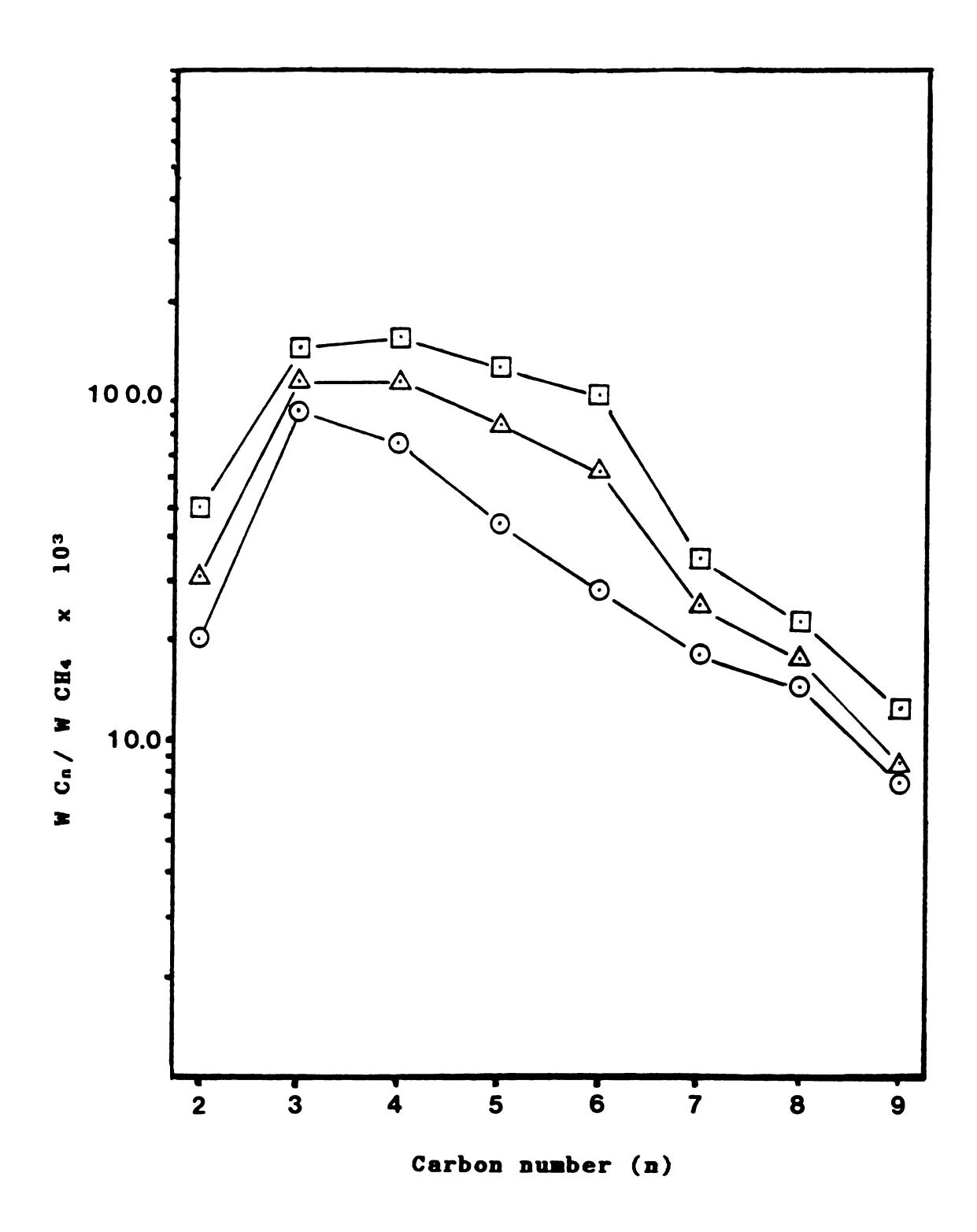


Figure 52. Increase in hydrocarbon production resulting from incorporation of 1-alkene probe molecules. The symbols signify; steady state FT (100 min.) \odot , hydrocarbon distribution during the first alkene addition \triangle , and after the second additon \square . The [alkene] in the second addition was twice the first. (275°C,110psi.,4336 hr⁻¹, H₂/CO=2, prereduced).

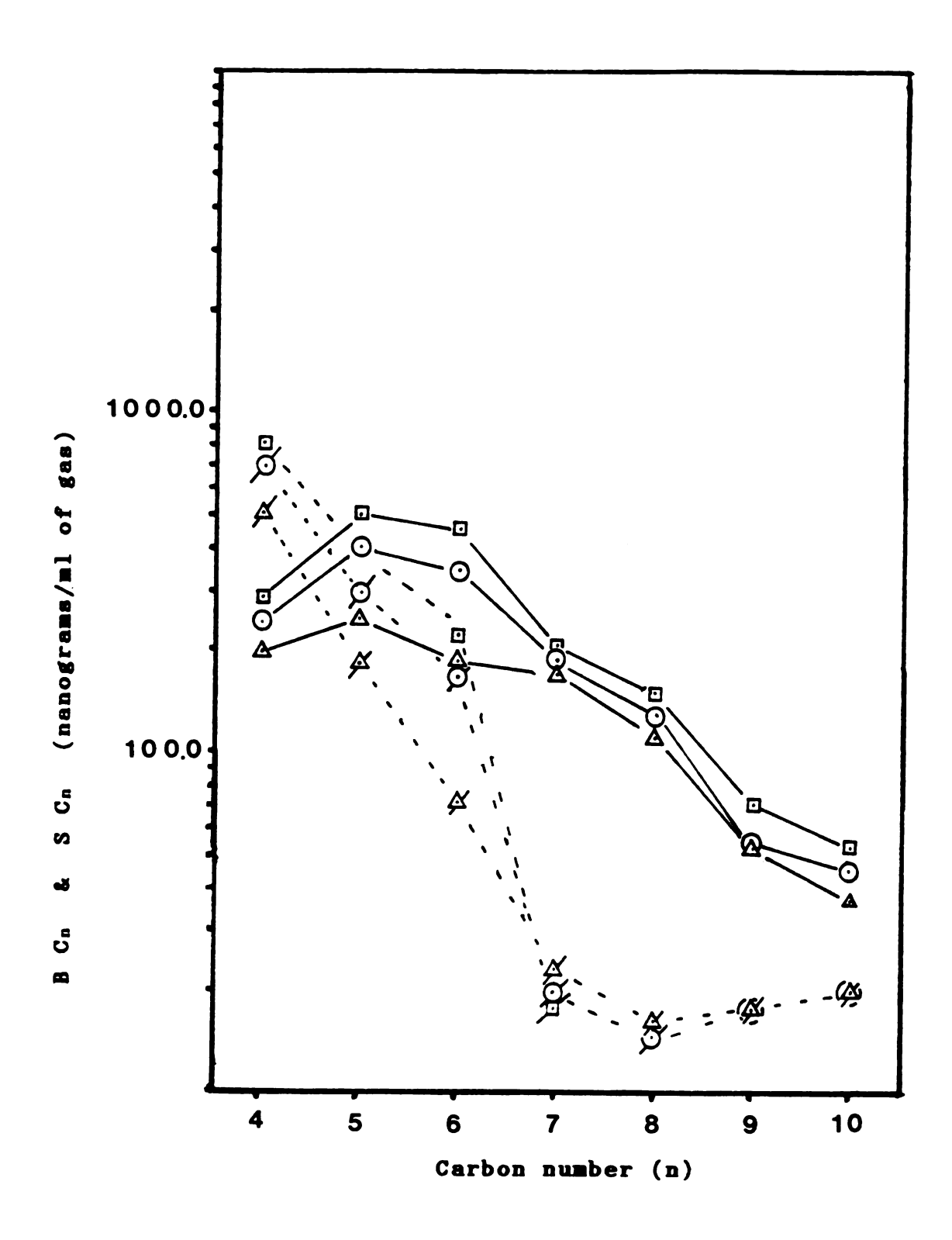


Figure 53. Production of branched and straight hydrocarbons before and after 1-alkene additions. The \triangle show steady state FT (180 min.), and \odot and \odot production after the first and second alkene additions, respectively. The slashed points are for straight isomers and the regular symbols are for branched products. (275°C, 110 psi., 4336 hr⁻¹, H₂/CO=2, prereduced).

alkene concentrations. Enhanced production of C_6 and C_5 branched products were similar and were greater than that for C_4 branched products. Production of branched products dropped sharply for $C_n > C_6$ but remained somewhat higher than initial FT production for C_7 - C_{11} products. This indicates enhanced production of hydrocarbons greater than the C_2 - C_6 olefins added occurred, and that olefins were incorporated into branched hydrocarbon products. This is consistent with the incorporation of olefins into growing chains and the proposal that Ru/APM catalysts are selective for branched products due to their intracrystalline acidity.

Figure 54 shows a breakdown of olefin incorporation for the internal alkenes produced in FT with these additions compared to the paraffin incorporation. The incorporation of olefins added also is evident in the production of internal alkenes. Based on the relationship obtained, which is nearly linear, it is also clear that cis-trans isomers are also increased for C7 hydrocarbons. This also lends support to the ability of Ru/APM to isomerize 1olefins to cis-trans isomers. The decreasing production of internal olefins with increasing C_n for Ru/APM is however contrary to the opposite trend observed by Dictor and Bell (127), who used iron based catalysts. They attributed their increased yields of internal olefins to longer residence times for higher C_n. The strong hydrogenation activity of Ru/APM catalysts however could readily transform internal olefins to paraffins which would explain this

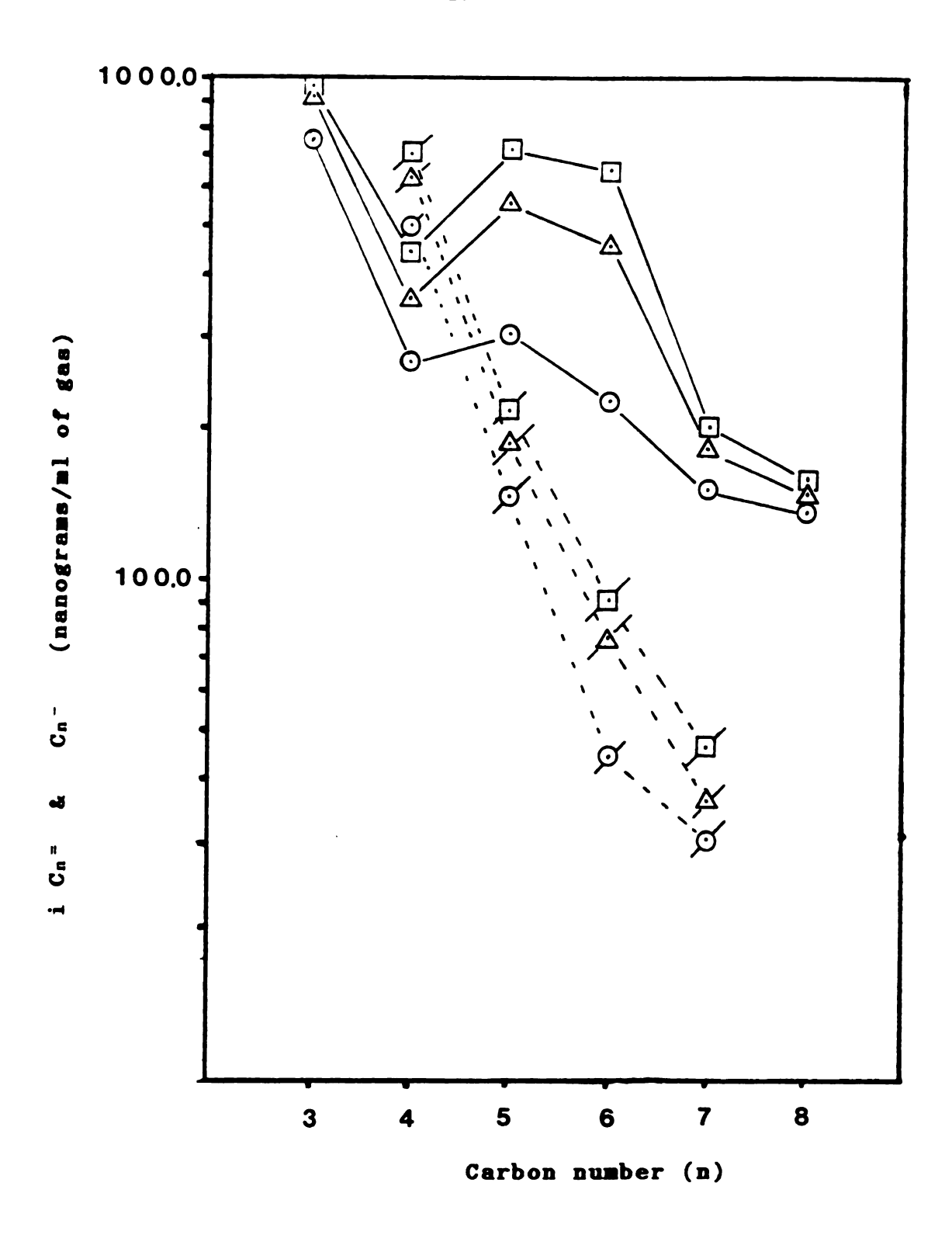


Figure 54. Breakdown of the 1-olefin probe molecules added during FT into internal olefins (iCn $^{\pm}$), and total paraffins (Cn $^{-}$). The regular symbols for FT steady state (180 min.) \odot , first addition \triangle , and second \odot refer to paraffins and the slashed symbols to internal olefins. FT conditions as in Figure 53.

discrepancy. The olefin/paraffin ratios obtained for Ru/APM are not as high as other supported Ru systems which could be due to this hydrogenation propensity.

When the C_2 - C_6 olefin mixture was passed over the Ru/APM at 275°C, 120psi, in the absence of CO (prior to FT) essentially 100% of the C_2 , C_3 olefins were converted to paraffins, demonstrating this hydrogenation activity. Residual alkenes for C_4 , C_5 and C_6 could just barely be detected. Chuang et al. (81) showed that 97% of C2 added to Ru/SiO2 catalysts under synthesis conditions (CO present) was hydrogenated to ethane. They detected 2% incorporation of ethylene into growing chains. The alkene addition to Ru/APM in the abscence of CO also yielded large quantities of methane which is due to hydrogenolysis. Chuang et al. (81) did not observe hydrogenolysis of the added ethylene, but cited references supporting the fact that this was due to the presence of CO, and competition of reactions such as chain growth. Hydrogenolysis on Ru has been studied extensively and the reader is referred elsewhere (182) for additional information.

To diminish the potential masking effects of hydrogenation in the production of internal olefins and branched hydrocarbons on Ru/APM catalysts the mass of alkene/mass of $\rm H_2$ was varied in the absence of CO. $\rm H_2$ /CO ratios were also varied during FT to examine these features.

For the first experiment the mass of alkene added to the Ru/APM catalyst at $275^{\circ}C$ and 1 atm, was changed with

respect to the flow of H_2 . To obtain higher dilutions of the H_2 in the feed gas He flows were also used. Flow rates were maintained at constant values throughout these experiments. These alkene additions were separated by a 30 min period of pure H_2 flow.

The relationships shown in Figure 55 for this study illustrate that the mass of C_n^- produced relative to methane decreased as the relative concentration of ${\rm H}_2$ was decreased. The lines drawn through the points show good correlations for all C_n except for C₃. These trends illustrate suppression of the hydrogen concentration at the metal surface because of the decreased conversion of added olefins to paraffins. The increase in olefin concentrations with decreased H2 concentration, shown in Figure 56, is in agreement with the paraffin plot (Figure 55). Of particular interest is the dramatically increased yields of both cis and trans isomers with decreased H2 concentrations. The ratio of cis to trans isomers would be expected to reach equilibrium values when skeletal rearrangement is occurring (13), whereas if they were produced as primary FT products their concentrations may be equal. It is also of great significance that at the lowest concentration of ${\rm H}_2$ branched products were observed clearly in the GC trace (Figure 57). Although their concentration is low relative to that of the neighboring paraffins produced by hydrogenation, they are similar in concentration to the peaks that represent the residual alkenes. This clearly demonstrates

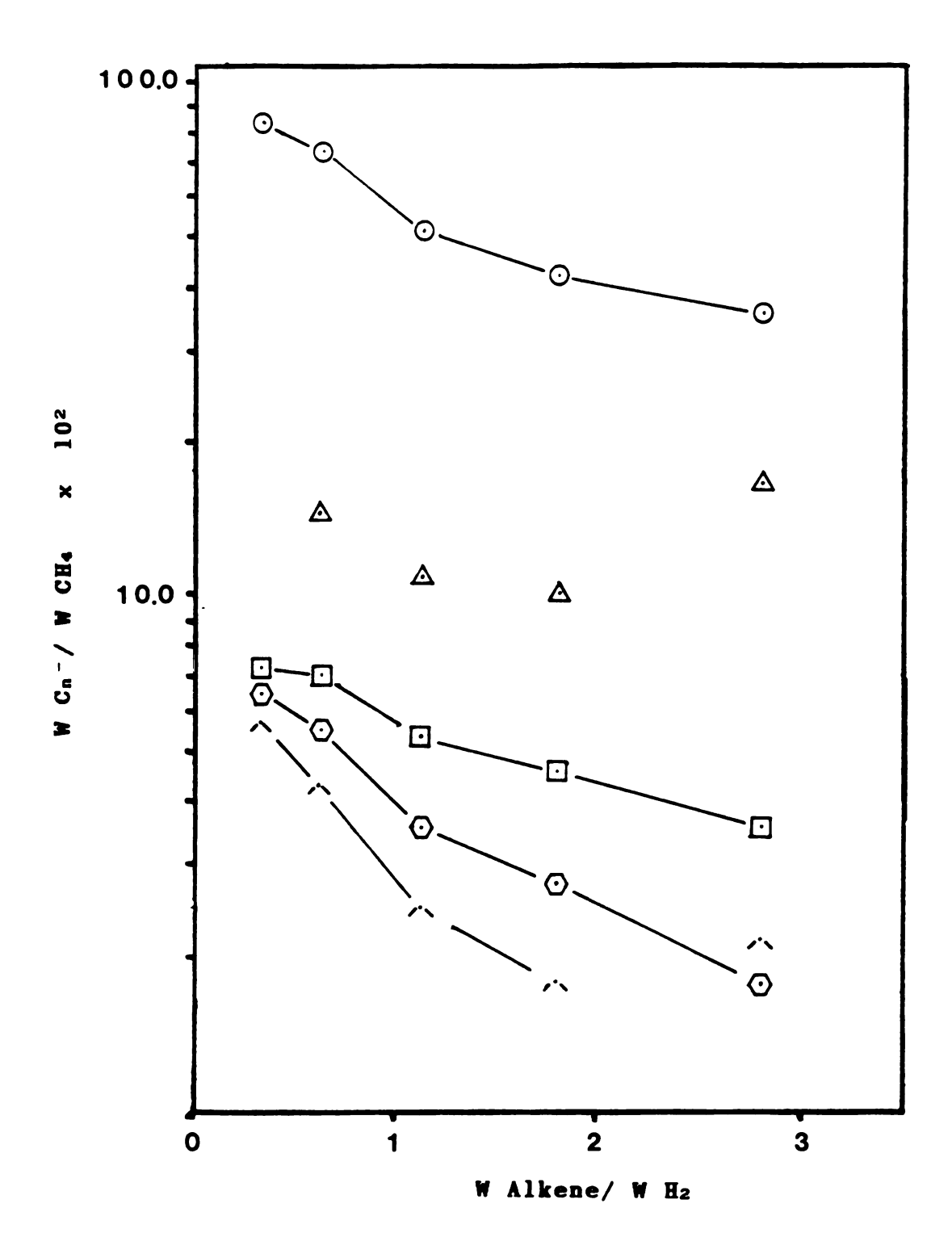


Figure 55. Transformation of 1-alkene probe molecules to alkanes in the absence of CO (no FT) as a function of the alkene to hydrogen ratio. The symbols represent; $C_2 \odot , C_3 \bigtriangleup , C_4 \sim , C_5 \odot ,$ and $C_6 \odot . (275°C, 1 atm., 3230 hr⁻¹)$

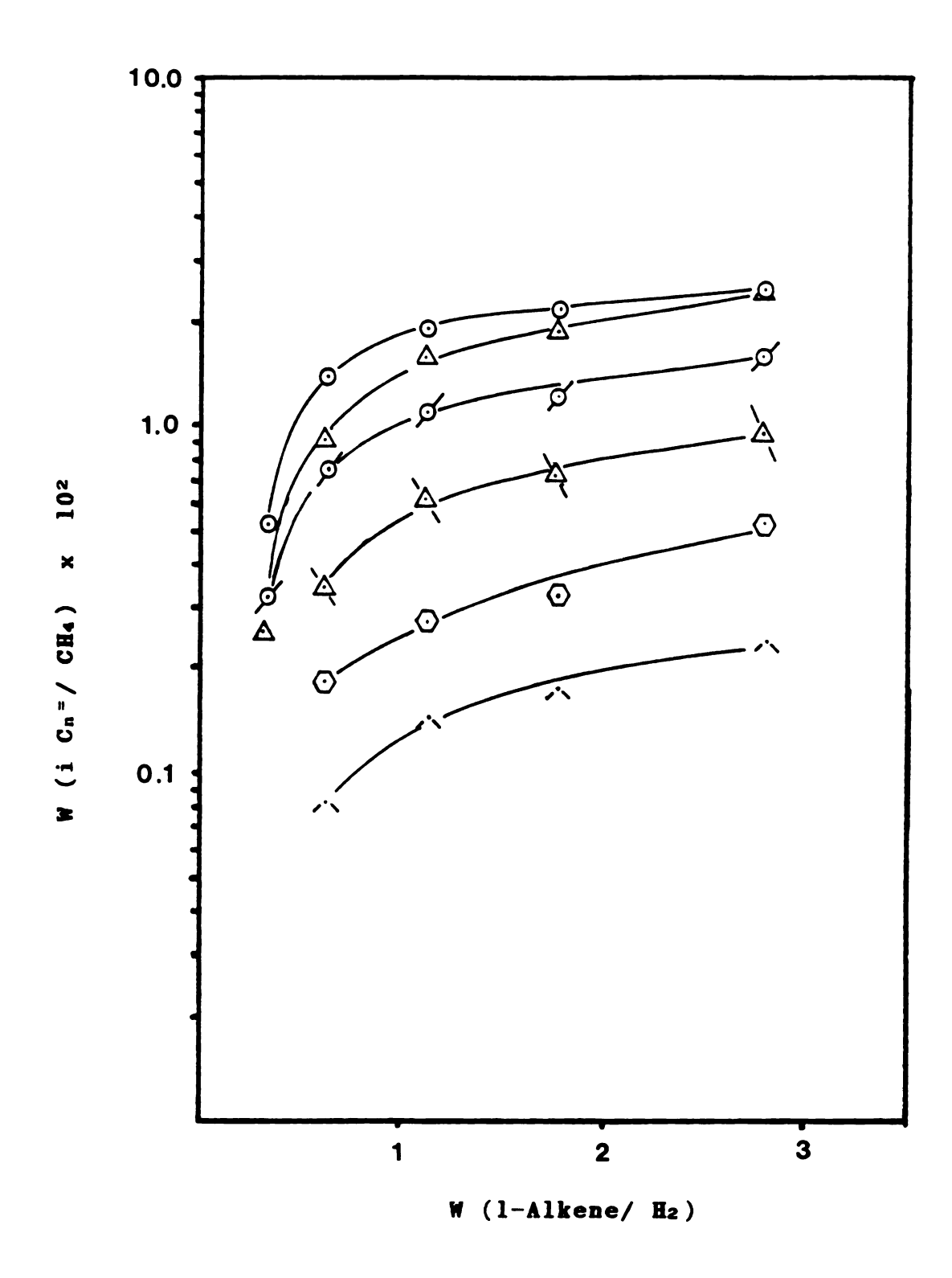


Figure 56. Transformation of the added 1-alkene probes to internal olefins as a function of the alkene to hydrogen ratio. The symbols are; cisC₄ \odot , trans C₄ \odot , cis C₅ \triangle , trans C₅ \triangle , $1-C_4$ = \bigcirc , $1-C_5$ = \bigcirc (275°C, 1 atm., 3230 hr⁻¹, prereduced.

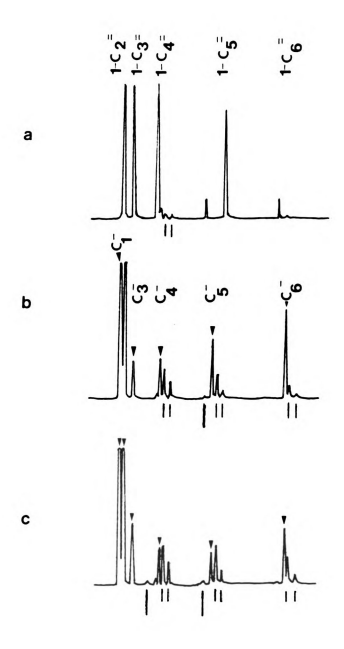


Figure 57. Gas chromatograms of 1-alkene probe molecules after passing through the Ru/APM catalyst bed. (a) 25° C before any isomerizations, (b) reactor effluent when alkenes are added to the catalyst at 275° C, 1 atm., 3230 hr $^{-1}$, 50 min. TOS, $(1-C_n=/H_2=1.25)$, (c) $1-C_n=/H_2=2.8$. Long bars indicate branched products and short bars internal olefins.

that 1-olefins can diffuse through the micropores of APM and be isomerized to branched products as well as internal olefins. Further, desorption of branched products through the micropores is possible for C_5 and C_6 hydrocarbons. The propensity for methane formation through hydrogenolysis (in the absence of CO) is also evident from the GC trace. The low H_2 concentration required for this branching to be detected suggests that H_2 concentration is very important to branching.

To examine the effects of decreased hydrogenation on branched hydrocarbons and internal olefin yields the $\rm H_2/CO$ ratio was varied during FT synthesis conditions. This was done following the alkene additions above by halting the alkene addition and increasing the $\rm H_2$ flow to 35 ml/min for 30 min to flush residual alkenes. The pressure was then increased from 15 to 120 psi while the $\rm H_2$ flow was kept constant. After 45 min at this pressure and 275°C the CO was added, and the $\rm H_2$ decreased so that a total flow rate of 35 ml/min was obtained. Fischer-Tropsch hydrocarbon production was equilibrated for 55 min before the first data point was taken. Each subsequent $\rm H_2/CO$ data point was taken after 50 min of equilibration.

Figure 58 relates the data obtained for the change in BC_n/SC_n with H_2/CO ratio. The relationships obtained show that branched hydrocarbon production increased with decreased H_2/CO . This was consistent with the data obtained for the alkene additions. Figure 59 further demonstrates

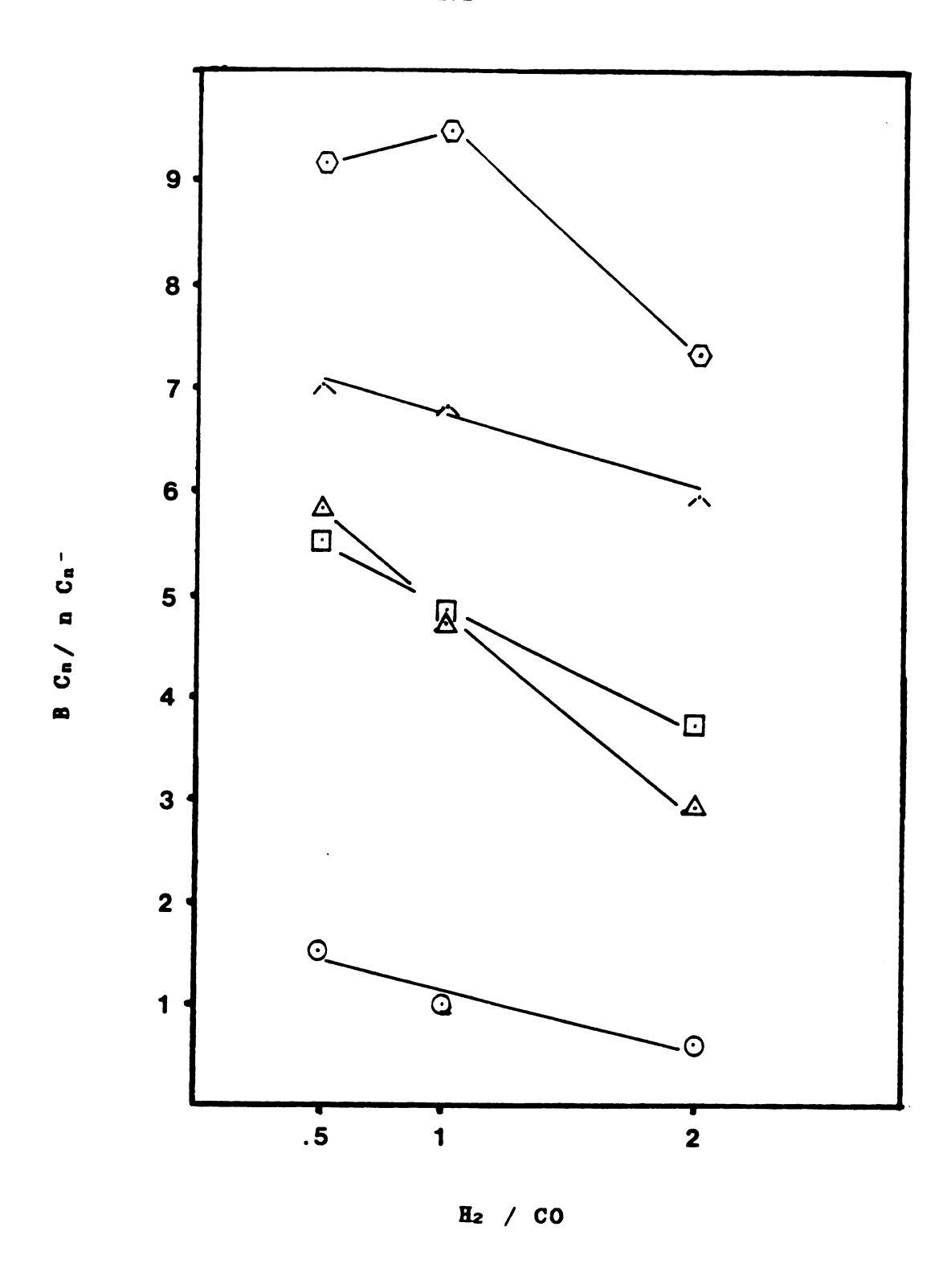


Figure 58. Change in the selectivity for branched hydrocarbons during FT with H_2/CO . The symbols are; C_4 \odot , C_5 \triangle , C_6 \bigcirc , C_7 \bigcirc , C_8 \nearrow . (275°C, 120 psi., 3230 hr⁻¹, prereduced).

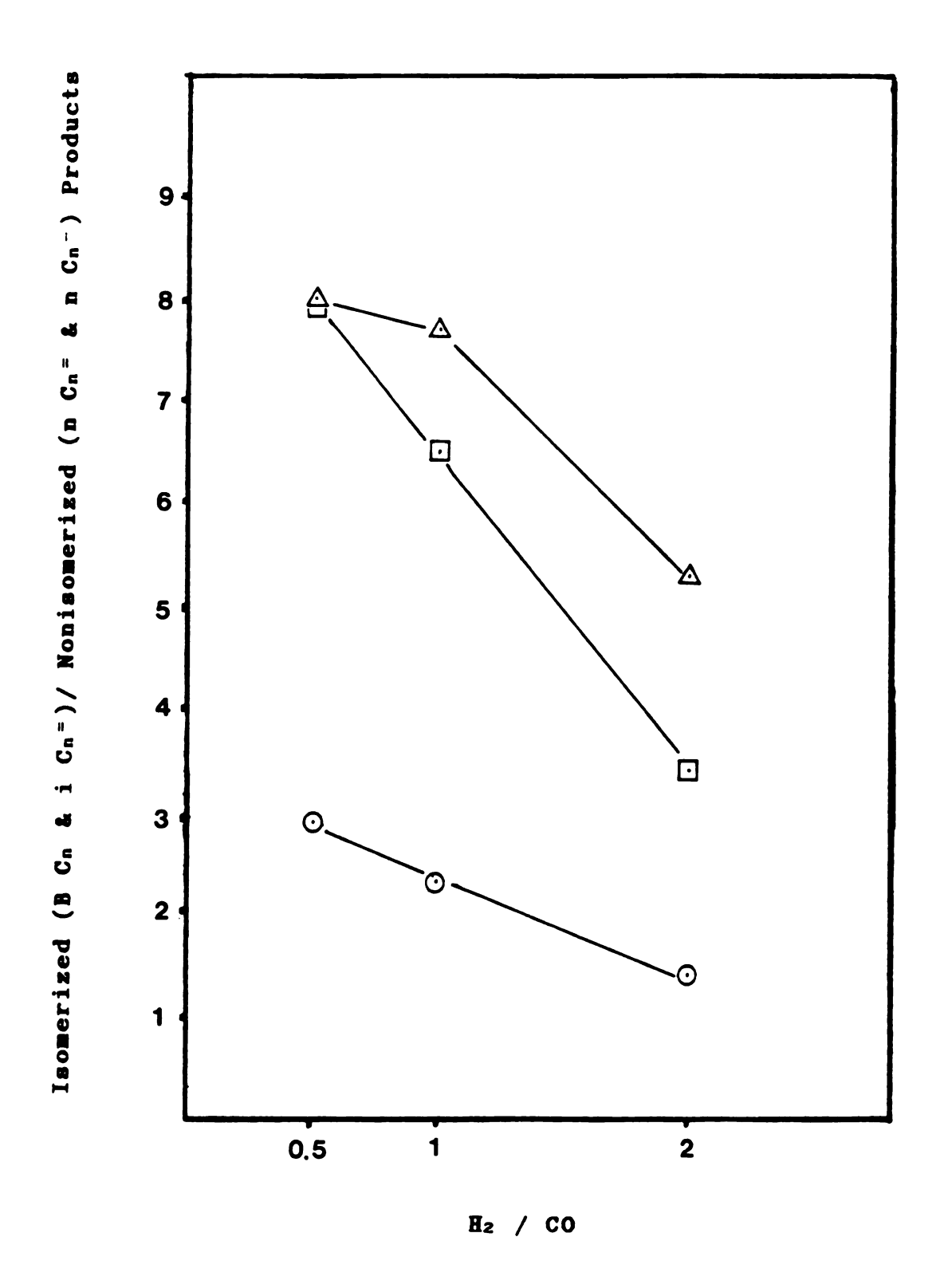


Figure 59. Isomerized hydrocarbon production vs. normal FT production (n-alkanes and 1-alkenes) as a function of the $\rm H_2/CO$ ratio. Here C₄ hydrocarbons are shown as \odot , C₅ as \odot , and C₆ as \triangle . (275°C, 120 psi., 3230hr⁻¹)

that decreased H_2 resulted in increased mass of isomerized products (branched hydrocarbons and internal olefins) relative to initial FT products (terminal olefins, and straight C_n).

These data clearly support the argument that decreased hydrogen concentration will result in increased yields of isomerized products. The correlation of enhanced branched hydrocarbon production with decreasing $[H_2]$ also supports the argument that 1-olefins are isomerized to branched hydrocarbons as their concentration would increase with lower H_2/CO . The increased olefin concentrations at lower H_2/CO would allow a higher proportion of molecules to reach the Bronsted acid sites of Ru/APM and be isomerized into branched products.

The isomerization selectivity for Ru/APM catalysts, due to the interaction of primary FT terminal olefin products with APM intracrystalline acid sites, is enhanced for prereduced catalysts as the Ru is retained within APM micro- and mesopores. Terminal olefins that originate on these Ru microcrystallites must diffuse past numerous intracrystalline acid sites on their way to the APM exterior. These interactions are strongly enhanced by the retention of Ru within the pore structure, which results in prereduced catalysts having a much higher selectivity for isomerized products than their nonprereduced counterparts (external dispersion of Ru). The chemical nature of APM then influences the FT production of hydrocarbons on metals

dispersed in pillared clays, which results in this unique isomerization selectivity for Ru.

H. Conclusions

The method of highly dispersing ruthenium in the micropores of alumina pillared montmorillonite (APM) by the intracrystalline protonation of Ru3(CO)12 presents potential advantages for heterogeneous catalysis. The ruthenium is dispersed within the micropores in a low oxidation state for example, and a prereduction in H2 was not required for activity in the hydrogenation of carbon monoxide (FT). Catalytic characterization of Ru/APM showed that deviations from SF were produced at short reaction times such as the apparent existance of more than one chain growth probability. Such deviations were short lived however, and after one hour hydrocarbon distributions closely followed SF. Catalysts that were prereduced in hydrogen conversely exhibited no initial SF deviations, but did give higher conversions and favored the production of higher molecular weight hydrocarbons.

High resolution electron microscopy studies proved vital in investigation of differences between nonprereduced and prereduced catalysts. These investigations revealed that in nonprereduced catalysts considerable Ru sintering occurred. The Ru migrated from the micropores of these materials and formed large crystallites on the APM support during catalysis. Nonprereduced catalysts run 30 hrs in FT

had a broad distribution of external metal crystallite sizes with an surface average mean particle size of 56 nm. Prereduced Ru/APM catalysts were significantly different as the majority of Ru atoms were retained within the APM during catalysis. The distribution of metal microcrystallites was much narrower for these catalysts and crystallites greater than 10 nm were not detected in the numerous samples studied by EM. Catalysts run for 30 hrs. gave a mean particle size of 6 nm, nearly an order of magnitude lower than their nonprereduced counterparts. Investigation of Ru/APM catalysts after reaction showed that microcrystallites on the order of 5 nm gave nanodiffraction patterns for Ru metal not ruthenium aluminates or oxides.

A model was proposed for the nature of the clay support to account for the presence of Ru microcrystallites on the order of 5 nm as the gallery height of 1 nm for APM should not accomodate such large crystallites. This model shows that such crystallites can be held in layer packing disorders created when clay layers stack atop one another in the air drying process. Physical characterization of APM lent support for this model, and the application of z-contrast imaging showed that indeed Ru microcrystallites were present in thicker regions where such void spaces would be numerous. These void spaces may trap Ru microcrystallites formed during the prereduction step and hinder their migration to form larger crystallites. Nonprereduced catalysts conversely may interact with CO present in the

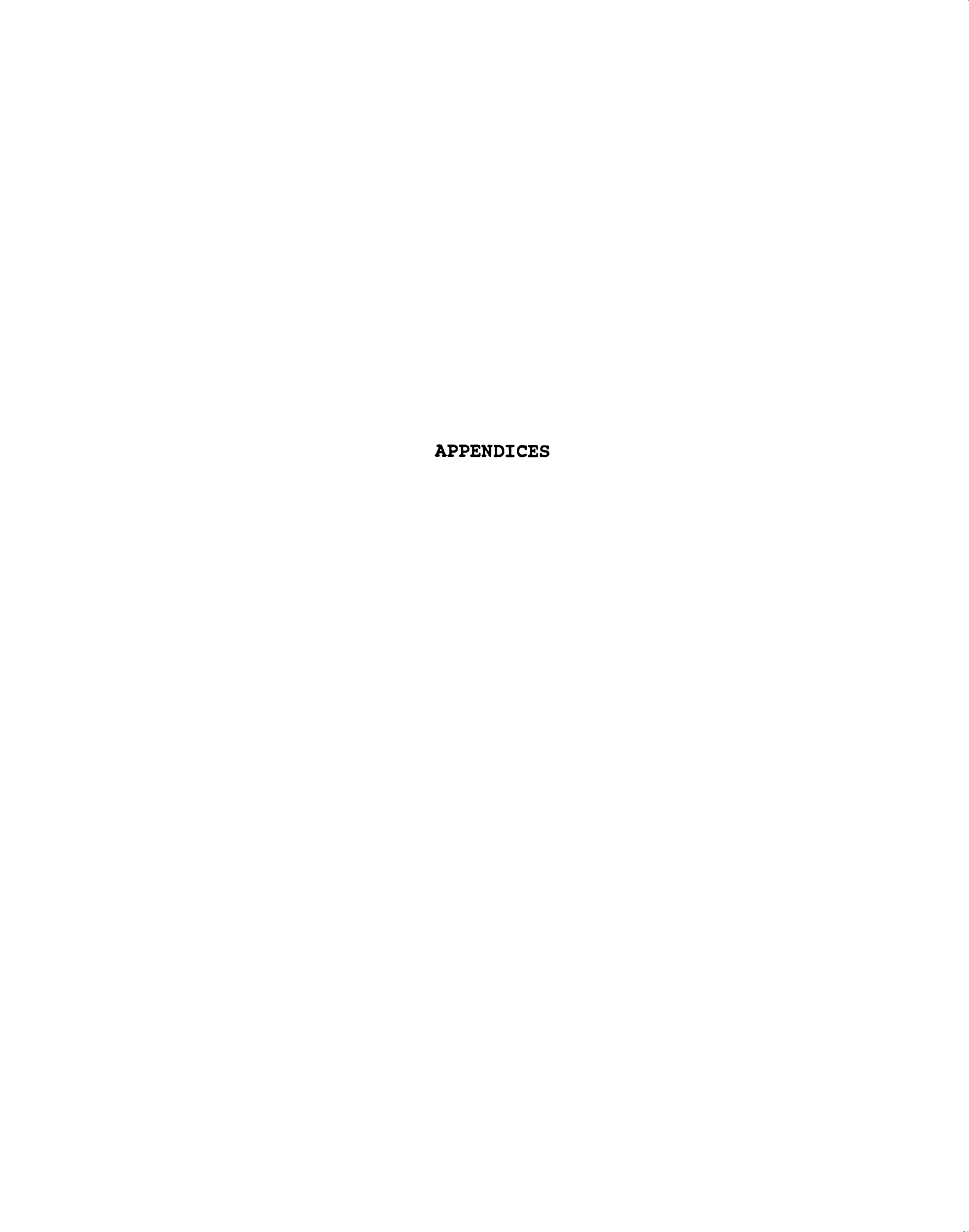
feed gas when FT begins, forming molecular clusters which readily desorb from the micropore regions and sinter on the APM surface.

Further catalytic examination of prereduced catalysts revealed that the carbon number distributions produced in FT followed SF regardless of run conditions and the containment of Ru within a micropore cavity did not give anomalous distributions of $C_{\rm n}$.

The two features that are surprising for Ru/APM catalysts in FT though are the high selectivities for branched hydrocarbons and internal olefins. Branching was found to be dependent on temperature, flow rate and to a lesser extent pressure. Internal olefin production was also dependent on these parameters, and these atypical products are changed somewhat with alteration of the CO conversion.

As production of these fractions is quite unusual for supported Ru catalysts potential mechanisms were discussed. These mechanisms pointed to the intracrystalline acidity of APM playing a significant role in production of these uncommon isomers. Addition of 1-olefin probe molecules showed that olefins were incorporated into higher molecular weight olefins and paraffins in agreement with previous literature results. Yet, these experiments also showed that these olefin probes were incorporated into branched hydrocarbons and internal olefins. Variation of the alkene /H₂ ratio showed that decreased hydrogen concentrations increased the yield of internal olefins and provided

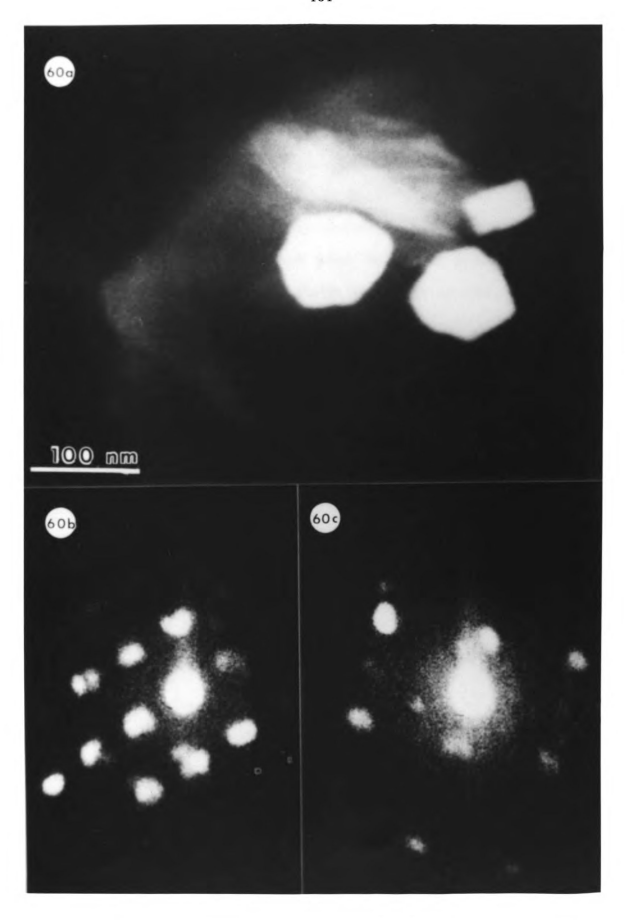
evidence that 1-olefins could diffuse to the acid sites and be isomerized to branched products as well as internal olefins. A study of production of these unusual products as a function of $\rm H_2/CO$ ratio during FT catalysis proved that production of branched hydrocarbons and internal olefins increased with decreasing $\rm H_2$ concentration. These experiments with alkene additions and $\rm H_2/CO$ variation added considerable support to the proposal that these products have enhanced selectivities for Ru/APM catalysts due to the intracrystalline acidity of alumina pillared clay.



Appendix A: Minimization of Microscope Artifacts

Ru/APM prior to catalysis contained essentially triatomic ruthenium centers weakly bound in the silicate interlayer, as shown by the physical characterization methods mentioned in Chapter IV. However, initial STEM studies of the Ru/APM prior to use as a FT catalyst showed no discernible Ru clusters when the sample was mounted on an ambient temperature stage. These triatomic clusters are apparently too small to scatter sufficient electrons, relative to the clay support, to be detectable in bright or dark field images. After extended periods (hrs.) of exposure to the electron beam however, the sample exhibited Ru aggregates on clay particles microns from the areas initially studied (159). Large aggregates (> 50 nm) exhibited symmetrical shapes, such as the pseudo-hexagonal and rectangular aggregates illustrated in Figure 60. These particular aggregates gave well ordered microdiffraction patterns consistent with hexagonal and monoclinic lattices as shown in Figures 60b and 60c, respectively. The presence of large Ru aggregates was inconsistent with the initial STEM studies and physical data mentioned earlier, so several regions of the sample were examined on numerous squares of the Cu grid. Ru aggregation appeared to diminish on

Figure 60. STEM dark field image of Ru crystallites formed by beam induced agglomeration in the microscope. Microdiffraction patterns are from the pseudo-hexagonal (a), and rectangular (b) crystallites. Sample stage at room temperature.



surfaces far from the initial study areas, but in some cases Ru aggregation was significant. The Ru appeared to cluster on external clay surfaces near edges or other sharp features that may have acted as nucleation centers.

Atom migration due to localized specimen heating has been reported previously (171,183-85). The selective loss of low mass elements or weakly-bound species due to localized beam heating also has been observed (183,184).

When a liquid nitrogen stage was used in the microscope, transported Ru aggregates were not found and Ru migration was minimized effectively in the numerous samples examined. Although the mechanism of Ru migration warrants further study, the important point is that with the use of a cold stage beam-induced Ru agglomeration was not evident. Thus, the Ru crystallite sizes observed for the spent catalyst should be truly reflective of the size distributions resulting from catalysis. It is noteworthy, however, that when the Ru/APM catalyst precursor was investigated by EDS microanalysis at 143 K with a tilt stage, characteristic Ru x-rays were not observed. It may be that the Ru carbonyl species on the surface were boiled-off by the beam or that the low Ru loadings of these catalysts (0.2-0.4 wt%) were near the EDS detection limit.

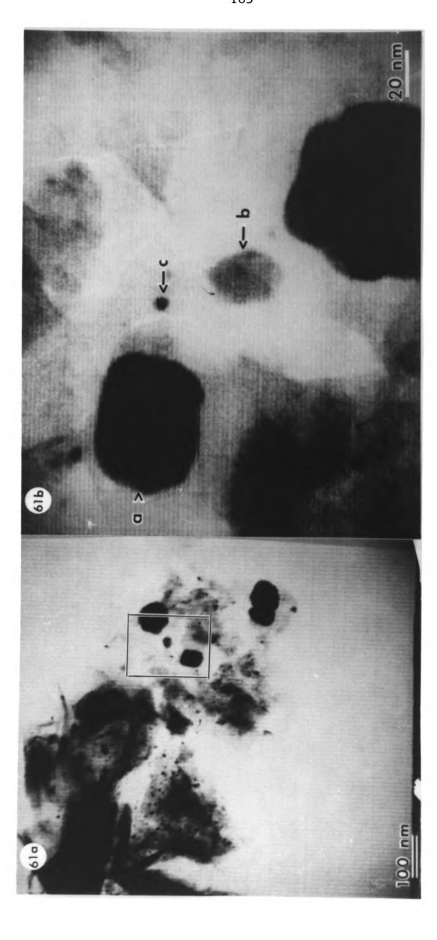
Appendix B: Feed Gas Impurities

The results from Chapter IV were obtained on catalyst samples exposed to purified reagent gases. In control runs for iron pillared clays catalytic characterization of the activity of the reactor system (mainly CH₄ production) was negligible relative to the hydrocarbon production from the Fe/PILC. With the low loadings of the Ru/APM system, and low conversion for nonprereduced catalysts, this background activity was not negligible.

Analytical STEM studies revealed the dramatic consequences of the use of technical grade gases. Figure 61 shows nonprereduced Ru/APM catalyst samples after 30 hrs of catalytic reaction in unpurified H₂ and CO. EDS analyses of these crystallites, shown in Figure 62, proved that not only Ru but also Ru/Fe and Ru/Ni alloy aggregates were present on the clay. The large concentrations of these impurities relative to Ru explains the high apparent metal concentration.

Numerous experiments proved that the contaminants were originating from metal carbonyls present in the feed gas, which was purchased in a steel tank. By changing the CO tank from steel to aluminum, use of ultra high purity gases, and the through purification procedures outlined in

Figure 61. Ru/APM after 30 hrs. of FT reaction with feed gas containing carbonyl impurities at low (a), and high magnification (b). Microscope sample stage at room temperature.



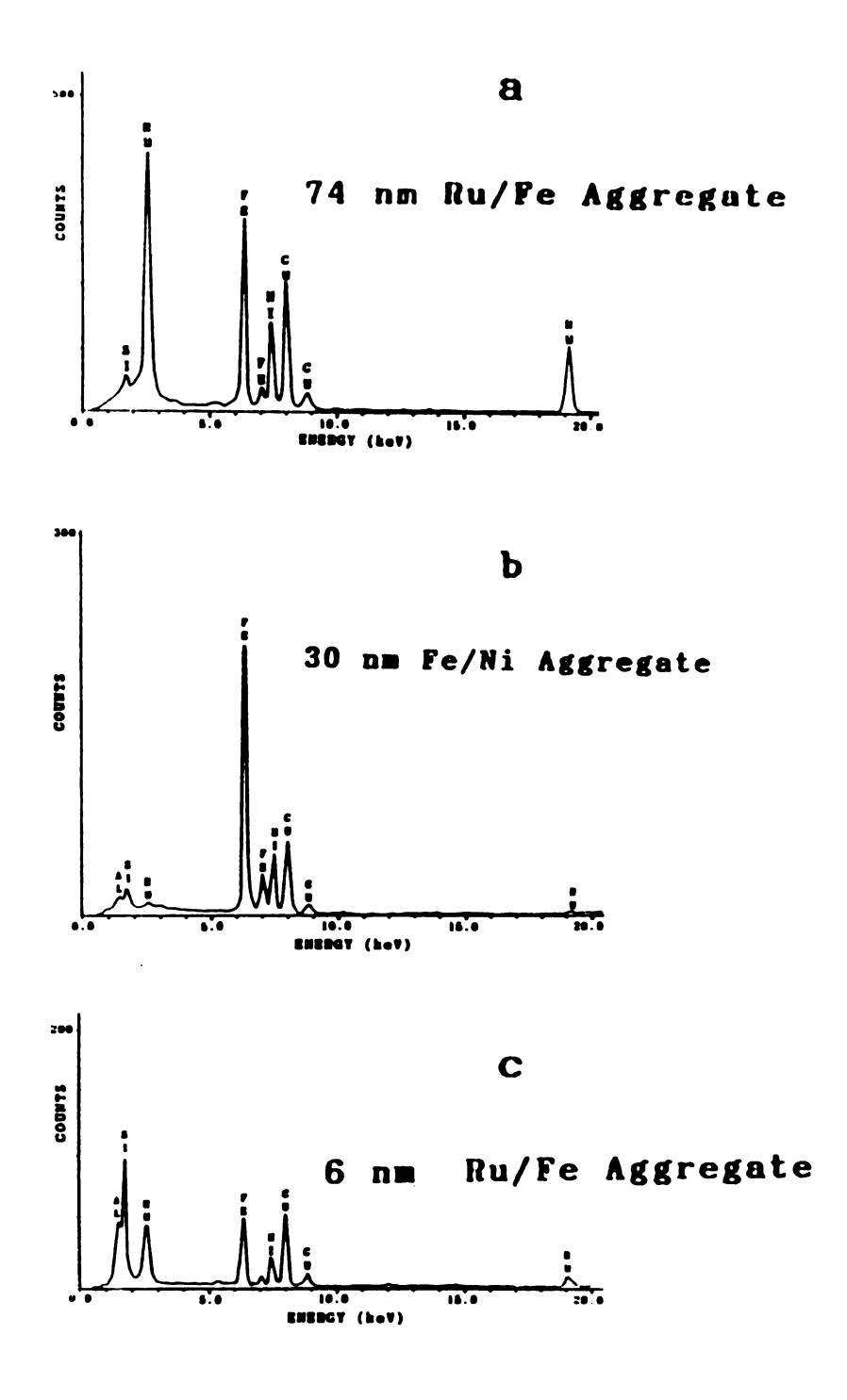


Figure 62. EDS analyses of the aggregates indicated in Figure 61, which show the presence of Fe and Ni impurities.

Chapter II this problem was eliminated. Control reactions of the new reactor system , run > 10 hrs., revealed that no background activity from the reactor was obtained up to 180 psi. when the reactor was reduced in $\rm H_2$ at 420°C overnight. The lack of metal carbonyl decomposition products inside the quartz insert further confirmed the successful removal of metal carbonyls. Finally, EDS microanalysis of post-run catalysts in the STEM did not show Fe, or Ni present on the catalyst surface.

Appendix C: Preparation of Oxygen Scrubber

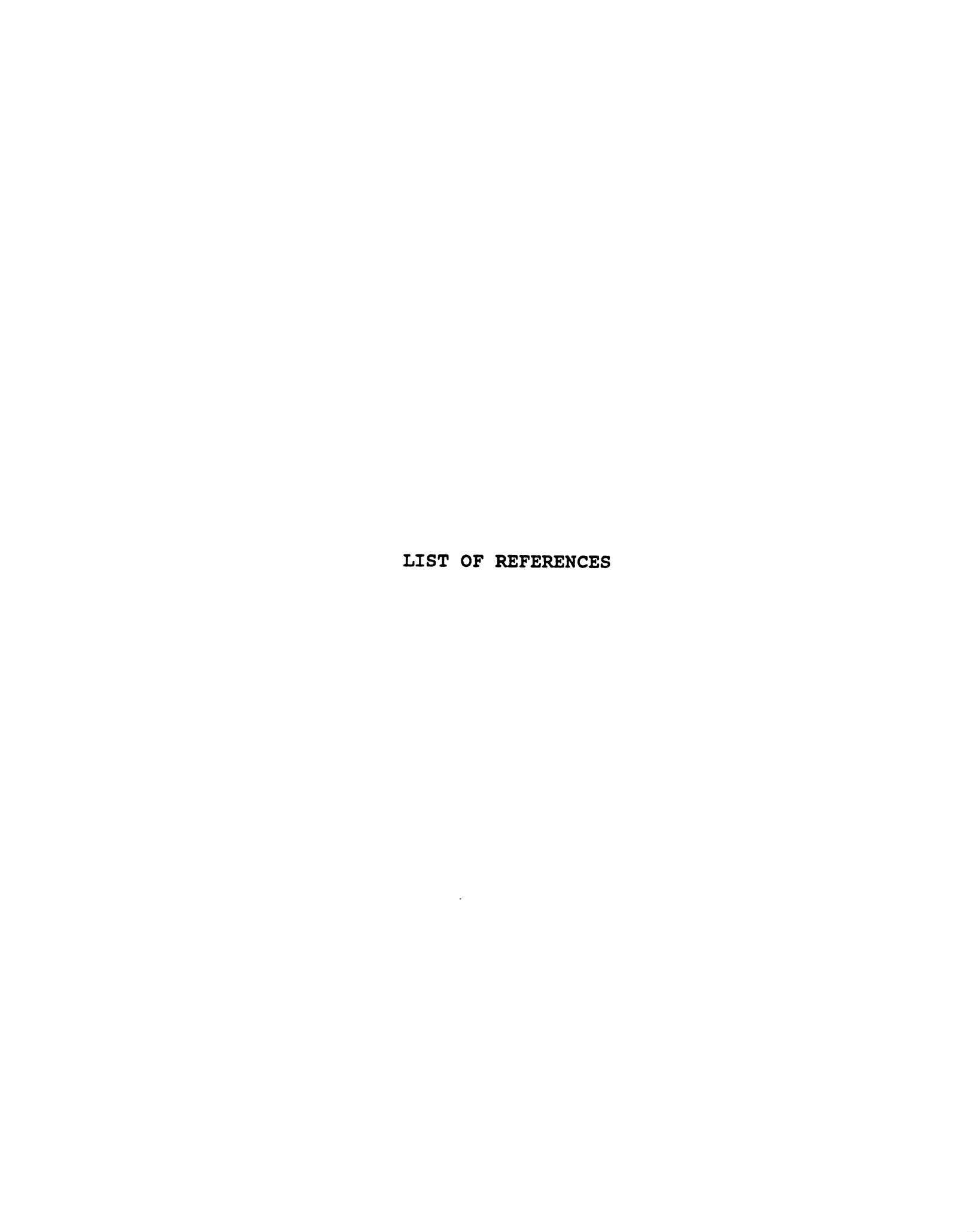
The synthetic method of Mc Ilwrick and Phillips (105) was the basis for the preparation of the Mn (II) oxide/SiO₂ oxygen scrubber used in the present work. They reported that Mn (II) oxide/ Celite diminished the oxygen concentration in N₂ streams to the parts per billion range.

The impregnation of Mn (II) on SiO₂ began by dissolving 500g of high purity Mn(C2H3O2)2 x 4H2O (Riedel-DeHaen AG) in enough MeOH to cover one pound of 12-28 mesh SiO₂ (Aldrich) placed in a crystallizing dish. The solution was dried by gentle warming with a hot plate (oven drying at 50°C would be preferable) with occasional stirring. After transferring the material to a baking dish and heating in an oven at 70°C overnight the solid was placed in calcining tubes. Argon was passed through the tubes (hood ventalation required) and the temperature was slowly increased to 400°C, which was maintained for 5 hrs. A vacuum was then pulled on the material at 400°C to insure complete removal of acetic acid. After slowly oxidizing at 25°C, air was passed over the material at 410°C, and cooled before it was resieved.

Nitric acid (3N) was added to the solid in a

crystallizing dish to remove any traces of other metal oxides, and to assure its catalytic inactivity. After 30 min. it was filtered with a Buchner funnel. It was then washed with copious quantities of deionized water. The Mn(II) oxide/SiO₂ was dried at 410° under vacuum before being added to the reactor system. This catalyst was activated in H₂ (50 ml/min.) by very slowly increasing the temperature to 420°C and maintaining this temperature overnight. The catalyst was tested for response to O₂ and reacted instantaneously when exposed to oxygen, turning from green to black.

This catalyst was also synthesized using mangenous nitrate (50wt% solution, Fischer) and SiO₂ beads 2-4 mm in diameter (Sigma), that had been additionally purified by acid and washings with deionized H₂O. The steps for impregnation were similar, but the nitrous oxides that evolve during heating required the use of a hood in an unoccupied room. This material was somewhat more difficult to reduce and was used only where larger catalyst particles were required.



REFERENCES

- Davies, J.E.D.; Kemula, W.; Powell, H.M.; Smith, N.O. J. Incl. Phenom. 1983, 1, 3.
- Setton, R.; ed. "Chemical Reactions in Organic and Inorganic Constrained Systems," D. Reidel, New York, 1986.
- 3. Whittingham, M.S., "Intercalation Chemistry," Whittingham, M.S.; Jacobson, A.J., eds., Academic Press, New York, 1982, 1.
- 4. Flanigen, E.M., "Zeolites: Science and Technology,"
 Riberio, F.R.; Rodrigues, A.E.; Rollman, L.D.;
 Naccache, C., eds., Martinus Nijhoff, Boston, 1984, 3.
- 5. Thomas, J.M.; Williams, C., "Chemical Reactions in Organic and Inorganic Constrained Systems," D. Reidel, New York, 1986, 49.
- 6. Dwyer, J., Chem. Ind., 1984, 258.
- 7. Barrer, R.M., "Zeolites and Clay Minerals as Sorbents and Molecular Sieves," Academic Press, New York, 1978.
- 8. Weisz, P.B.; Frilette, V.J., <u>J. Phys. Chem.</u>, 1960, <u>64</u>, 382.
- 9. Csicsery, S.M., Zeolites, 1984, 4, 202.
- 10. Maxwell, I.E., <u>J. Incl. Phenom.</u>, 1986, <u>4</u>, 1.
- 11. Derouane, E.G.; Gabelica, Z., J. Catal., 1980, 65, 486.
- 12. Corma, A.; Wojciechowski, B.W., <u>Catal. Rev. Sci. Eng.</u>, 1985, 27(1), 29.
- 13. Gates, B.C.; Katzer, J.R.; Schuit, G.C.A., "The Chemistry of Catalytic Processes," McGraw-Hill, New York, 1974.
- 14. Breck, D.W., "Zeolite Molecular Sieves," Wiley, New York, 1974.

- 15. Sudo, T.; Shimoda, S.; Yotsumoto, H.; Aita, S.,
 "Developments in Sedimentology 31: Electron Micrographs
 of Clay Minerals," Elsevier, New York, 1981.
- 16. Borchardt, G.A., "Minerals in Soil Environments,"
 Dixon, J.B.; Weed, J.B., eds., Soil Science Society of
 America, 1982, 293.
- 17. Pinnavaia, T.J. Science, 1983, 220, 3651.
- 18. Scurrell, M.S., "Specialist Periodical Reports.
 Catalysis"; Royal Society of Chemistry, London, 1978,
 2, 215.
- 19. Bailar, J.C. Jr., <u>Catal. Rev. Sci. Eng.</u>, 1974, <u>10(1)</u>, 17.
- 20. Bailey, D.C.; Langer, S.H., Chem. Rev., 1981, 81(2), 109.
- 21. Pinnavaia, T.J; Raythatha, R.; Lee, J.G.S., Halloran, L.J; Hoffman, J., J. Am. Chem. Soc., 1979, 101, 6891.
- 22. Mortland, M.M.; Raman, K.V., Clays Clay Miner., 1968, 16, 393.
- 23. Fripiat, J.J., ACS Symp. Ser., 1976, 34, 261.
- 24. Mortland, M.M., Trans. 9th Int. Congr. Soil Sci., 1968, 1, 691.
- 25. Mortland, M.M.; Fripiat, J.J.; Chaussidon, J.; Uytterhoeven, J.; J. Phys. Chem., 1963, 67, 248.
- 26. Laszlo, P., Acc. Chem. Res., 1986, 19, 121.
- 27. Benesi, H.A.; Winquest, B.H., <u>Adv.</u> <u>Catal.</u>, 1978, <u>27</u>, 170.
- 28. Ballantine, J.A., "Chemical Reactions of Organic and Inorganic Contstrained Systems," Setton, R., ed., D. Reidel, Boston, 1986, 197.
- 29. Cornelis, A.; Laszlo, P., <u>ibid.</u>, 213.
- 30. Thomas, J.M., "Intercalation Chemistry," Whittingham, M.S.; Jacobson, A.J., eds., Academic Press, New York, 1982, 55.
- 31. Adams, J.M.; Clapp, T.V.; Clement, D.E.; Reid, P.I., J. Mol. Cat., 1984, 27, 179.

- 32. Ballantine, J.A.; Davies, M.; Patel, I.; Purnell, H.; Rayanakorn, M.; Williams, K.J.; Thomas, J.M., J. Mol. Cat., 1984, 26, 37.
- 33. Weiss, A., Angew. Chem. Int. Ed. Engl., 1981, 20, 850.
- 34. Barrer, R.M; MacLeod, D.M., <u>Trans. Faraday Soc.</u>, 1955, <u>51</u>, 1290.
- 35. Barrer, R.M.; Reay, J.S.S., <u>Trans. Faraday Soc.</u>, 1957, 53, 1253.
- 36. Mortland, M.M.; Berkheiser, V.E., Clays Clay Miner., 1976, 24, 60.
- 37. Shabtai, J.; Frydman, N.; Lazar, R., <u>Clays Clay</u> <u>Miner.</u>, 1978, <u>26</u>, 107.
- 38. Berkheiser, V.E.; Mortland, M.M., Clays Clay Miner., 1977, 25, 105.
- 39. Traynor, M.F.; Mortland, M.M.; Pinnavaia, T.J., Clays Clay Miner., 1978, 26, 313.
- 40. Koppelman, M.H.; Dillard, J.G., Clays Clay Miner., 1980, 28, 211.
- 41. Brindley, G.W.; Sempels, R.E., Clay Miner., 1977, 12, 229.
- 42. Yamanaka, S.; Brindley, G.W., Clays Clay Miner., 1978, 26, 21.
- 43. Lahav, N.; Shani, V.; Shabtai, J., <u>Clays Clay Miner.</u>, 1978, 26, 107.
- 44. Vaughan, D.E.W.; Lussier, R.J., preprints, Fifth International Conference on Zeolites, Naples, Italy, June 2-6, 1980.
- 45. Shabtai, J.; Lahav, N., U.S. patent 4,216,188 (1980).
- 46. Shabtai, J., U.S. patent 4,238,364 (1980).
- 47. Lussier, R.J.; Magee, J.S.; Vaughan, D.E.W., preprints, Seventh Canadian Symposium on Catalysis, Edmonton, Alberta, 19-22 October, 1980.
- 48. Vaughan, D.E.W.; Lussier, R.J.; Magee, J.S., U.S. patents 4,176,090 (1979); 4,271,043 (1981); 4,248,739 (1981).
- 49. Shabtai, J.; Lazar, R.; Oblad, A.G., New Horiz. Catal., 1981, 7, 828.

- 50. Occelli, M.L.; Tindwa, R.M.; <u>Clays Clay Miner.</u>, 1983, <u>31</u>, 22.
- Gaaf, J.; van Santen, R.; Knoester, A.; Winderden, B.,
 Chem. Soc. Chem. Comm., 1983, 655.
- 52. Kikuchi, E.; Hamana, R.; Nakano, M.; Takehara, M.; Morita, Y., <u>J. Jpn. Pet. Inst.</u>, 1983, <u>26</u>, 116.
- 53. Burch, R.; Warburton, C.I., <u>J. Catal.</u>, 1986, <u>97</u>, 503.
- 54. <u>ibid.</u>, 510.
- 55. Endo, T.; Mortland, M.M.; Pinnavaia, T.J., Clays Clay Miner., 1980, 28, 105.
- 56. Yamanaka, S.; Yamashita, G.; Hattori, M., Clays Clay Miner., 1980, 28, 281.
- 57. Brindley, G.W.; Yamanaka, S., <u>Amer. Miner.</u>, 1979, <u>64</u>, 830.
- 58. Tzou, M.S., Ph.D. Dissertation, Michigan State University, 1983.
- 59. Yamanaka, S.; Doi, T.; Sako, S.; Hattori, M., <u>Mat.</u> <u>Res.</u> <u>Bull.</u>, 1984, <u>19</u>, 161.
- 60. Pinnavaia, T.J., Chemical Synthesis using Supported Reagents, *Laszlo, P., ed., 1986.
- 61. Pinnavaia, T.J., "Chemical Reactions in Constrained Systems," Setton, R., ed., D. Reidel, New York, 1986, 151.
- 62. Barrer, R.M., <u>J. Incl. Phenom.</u>, 1986, <u>4</u>, 109.
- 63. Lewis, R.M.; Ott, K.C.; van Santen, R.A., U.S. patent 4,510,257 (1985).
- 64. Sabatier, P.; Senderens, J.B.; <u>J. Soc. Chem. Ind.</u>, 1902, <u>21</u>, 504.
- 65. <u>Badische Anilin und Soda Fabrik</u>, German Patents 293,787 (1913), 295,202 (1914).
- 66. Fischer, F.; Tropsch, H., <u>Brennst. Chem.</u>, 1923, <u>4</u>, 276.
- 67. <u>ibid.</u>, 1926, <u>7</u>, 97.

- 68. Masters, C., "Advances in Organometallic Chemistry," Stone, F.G.A.; West, R., eds., Academic Press, London, 1964, 63.
- 69. Pichler, H., Adv. Catal., 1952, 4, 271.
- 70. Storch, H.H.; Columbic, N.; Anderson, R.B., "The Fischer-Tropsch and Related Synthesis," J. Wiley, New York, 1956, Volume 4.
- 71. Anderson, R.B., "Catalysis" Emmett, P.H., ed., Reinhold, New York, 1956.
- 72. Vannice, M.A., J. Catal., 1975, 37, 449.
- 73. Mills, G.A.; Steffgen, F.W., <u>Catal.</u> <u>Rev.</u>, 1974, <u>8</u>, 159.
- 74. Bell, A.T., Catal. Rev.-Sci. Eng., 1981, 23(1), 203.
- 75. Boudart, M.; MacDonald, M.A., <u>J. Phys. Chem.</u>, 1984, 88, 2185.
- 76. Ponec, V., "Specialist Periodical Reports. Catalysis"; Royal Society of Chemistry, London, 1982, 5, 48.
- 77. Vannice, M.A., "Catalysis. Science and Technology," Anderson, J.R.; Boudart, M., eds., Springer-Verlag, Heidelberg, 1982, 3, 139.
- 78. Biloen, P.; Sactler, W.M.H., <u>Adv.</u> <u>Catal.</u>, 1981, <u>30</u>, 165.
- 79. Kellner, C.S.; Bell, A.T., J. Catal., 1981, 70, 418.
- 80. Pichler, H.; Schulz, H., Chem.-Ing.-Tech., 1970, 42, 1162.
- 81. Dry, M.E., <u>Ind. Eng. Chem. Prod. Res. Dev.</u>, 1976, <u>15</u>, 282.
- 82. Henrichi-Olive, G.; Olive, S., <u>Angew. Chem. Int. Engl.</u> <u>Ed.</u>, 1976, <u>15</u>, 136.
- 83. Flory, P.J., J. Am. Chem. Soc., 1936, 58, 1877.
- 84. Schulz, G.V., Z. Phys. Chem., 1935, 30, 399.
- 85. King, D.L.; Cusumano, J.A.; Garten, R.L., <u>Catal. Rev.-Sci. Eng.</u>, 1981, <u>23(1)</u>, 233.
- 86. Fraenkel, D.; Gates, B.C., <u>J. Am. Chem. Soc.</u>, 1979, 102, 2478.

- 87. Nijs, H.H.; Jacobs, P.A.; Uytterhoeven, J.B., <u>J. Chem.</u> Soc. Chem. Commun., 1979, 180.
- 88. ibid., 1979, 1095.
- 89. Nazar, L.F.; Ozin, G.A.; Hughes, F.; Godber, J.; Rancourt, D., J. Mol. Cat., 1983, 21, 313.
- 90. Ballivet-Tkatchenko, D.; Tkatchenko, I., J. Mol. Cat., 1981, 13, 1.
- 91. Vanhove, D.; Makambo, P.; Blanchard, M., J.C.S. Chem. Comm., 1979, 605.
- 92. Madon, R.J., <u>J. Catal.</u>, 1979, <u>57</u>, 183.
- 93. Bailey, D.C.; Langer, S.H., Chem. Rev., 1981, 81, 109.
- 94. Zwart, J.; Snel, R., J. Mol. Cat., 1985, 30, 305.
- 95. Nijs, H.H.; Jacobs, P.A., J. Catal., 1980, 65, 328.
- 96. Kellner, C.S.; Bell, A.T., J. Catal., 1982, 75, 251.
- 97. Anderson, J.R., "Structure of Metallic Catalysts," Academic Press, London, 1975, 369 and 245.
- 98. Basset, J.M.; Ugo, R., "Aspects of Homogeneous Catalysis," Ugo, R., ed., D. Reidel, Boston, 1977, Volume 3.
- 99. Gallezot, P., Catal. Rev. Sci.-Eng., 1979, 20, 21.
- 100. Chang, C.D.; Lang, W.H.; Silvestri, A.J., <u>J.</u> <u>Catal.</u>, 1979, <u>56</u>, 268.
- Caesar, P.D.; Brennan, J.A.; Garwood, W.E.; Ciric, J.,
 <u>J.</u> Catal., 1979, <u>56</u>, 274.
- 102. Chang, C.D.; Lang, W.H.; Silvestri, A.J., U.S. patent 4,086,262 (1978).
- 103. Giannelis, E.P., Ph.D. Dissertation, Michigan State University, 1984.
- 104. Landau, S.D., Ph.D. Dissertation, Michigan State University, 1984.
- 105. McIlwrick, C.R.; Phillips, C.S.G., <u>J. Phys.</u> <u>E.</u>, 1983, <u>6</u>, 1973.
- 106. Anderson, R.B., "The Fischer-Tropsch Synthesis," Academic Press, New York, 1984.

- 107. Brenner, A.; Hucul, D.A., <u>Inorg. Chem.</u>, 1979, <u>18</u>, 2836.
- 108. Hughes, F.; Bussiere, P.; Basset, J.M.; Commerenc, D.; Chauvin, Y.; Bonneviot, L.; Oliver, D., Proc. Seventh Int. Cong. Catal., Seiyama, T.; Tanabe, K., eds., Elsevier, Amsterdam, 1981, A. 418.
- 109. Lung, H-J.; Vannice, M.A.; Mulay, L.N.; Stanfield, R.M.; Delgass, W.N., J. Catal., 1982, 76, 708.
- 110. Sylva, R.N., Pure. Appl. Chem., 1972, 22, 115.
- 111. Flynn, C.M. Jr., Chem. Rev., 1984, 84, 31.
- 112. Arnek, R.; Schlyter, K., <u>Acta. Chem. Scand.</u>, 1968, <u>22</u>, 1327.
- 113. Spiro, T.G.; Allerton, S.E.; Renner, J.; Terzis, A.; Bliss, R.; Saltman, P., <u>J. Am. Chem. Soc.</u>, 1966, <u>88</u>, 2721.
- 114. Murphy, D.J.; Posner, A.M.; Quirk, J.P., <u>J.</u> Colloid Interface Sci., 1976, <u>56</u>, 270.
- 115. ibid., 284.
- 116. ibid., 298.
- 117. ibid., 312.
- 118. Matijevic, E.; Scheiner, P., J. Colloid Interface Sci., 1978, 63, 509.
- 119. Barnhisel, R.I., "Minerals in Soil Environments,"
 Dixon, J.B.; Weed, S.B., eds., Soil Science Society
 of America, Madison, WI, 1977, 345.
- 120. Oades, J.M., Clays Clay Miner., 1984, 32, 49.
- 121. Krebs, H.J.; Bonzel, H.P.; Schwarting, W.; Gafner, G., J. Catal., 1981, 72, 199.
- 122. Madon, R.J.; Taylor, W.F., J. Catal., 1981, 69, 32.
- 123. Dwyer, D.J.; Somorjai, G.A., <u>J. Catal.</u>, 1978, <u>52</u>, 291.
- Dwyer, D.J.; Hurdenbergh, H., <u>J. Catal.</u>, 1984, <u>87</u>, 66, and references therein.
- 125. Raupp, G.B.; Delgass, W.N., J. Catal, 1979, 58, 361.

- 126. Niemantsverdriet, J.W.; van der Kraan, A.M.; van der Dijk, W.L.; van der Baan, H.S., J. Phys. Chem., 1980, 84, 3363.
- 127. Dictor, R.A.; Bell, A.T., J. Catal., 1986, 97, 121.
- 128. Accuri, K.B.; Schwartz, L.H.; Piotrowski, R.D.; Butt, J.B., J. Catal., 1984, 95, 349.
- 129. Amelse, J.A.; Schwartz, L.H.; Butt, J.B., <u>J. Catal.</u>, 1981, 72, 95.
- 130. Pichler, H.; Schulz, H., Chem. Ing. Tech., 1970, 42, 1162.
- 131. Konig, L.; Gaube, J., Chem. Ing. Tech., 1983, 55, 14.
- 132. Huff, G.A. Jr.; Satterfield, C.N., <u>J. Catal.</u>, 1984, 85, 370.
- 133. Gard, J.S., ed., "The Electron-Optical Investigation of Clays," Mineralogical Society, London, 1971.
- 134. Zvyagin, B.B., "Electron Diffraction Analysis of Clay Mineral Structures," Plenum Press, New York, 1967.
- 135. Thomas, J.M.; Jefferson, D.A.; Mullinson, L.G.; Smith, D.J.; Crawford, E.S., Chem. Scripta., 1978-79, 14, 167.
- 136. Cowley, J.M.; Goswomi, A., <u>Acta. Cryst.</u>, 1961, <u>14</u>, 1071.
- 137. Goldstein, J.I., "Practical Scanning Electron Microscopy," Goldstein, J.I.; Yakowitz, H., eds., Plenum Press, New York, 1975.
- 138. Cliff, G.; Lorimer, G.N., <u>J. Microsc.</u>, 1975, <u>103</u>, 203.
- 139. Pinnavaia, T.J.; Tzou. M.S.; Landau, S.D.; Raythatha, R.H., <u>J. Mol. Cat.</u>, 1984, <u>27</u>, 195.
- 140. Occelli, M.L.; Tindwa, R.M., <u>Clays Clay Miner.</u>, 1983, <u>31(1)</u>, 22.
- 141. Occelli, M.L.; Landau, S.D.; Pinnavaia, T.J., <u>J.</u> Catal., 1984, <u>90</u>, 256.
- 142. Occelli, M.L.; Landau, S.D.; Pinnavaia, T.J., submitted to J. Catal., 1986.
- 143. van Damme, H.; Fripiat, J.J., <u>J. Chem. Phys.</u>, 1985, <u>82</u>, 2785.

- 144. Pinnavaia, T.J., personal communication.
- 145. Plee, D.; Borg, F.; Gatineau, L.; Fripiat, J.J., <u>J.</u>
 <u>Am.</u> Chem. Soc., 1985, 107, 2363.
- 146. Schmidt, L.D.; Wang, T.; Vacques, A., Ultramicroscopy, 1982, 8, 175.
- 147. Delannay, F., "Characterization of Heterogeneous Catalysts," Marcel Dekker, New York, 1984, 71.
- 148. Lyman, C.E., J. Mol. Cat., 1983, 20, 357.
- 149. Cowley, J.M., "Catalytic Materials: Relationship Between Structure and Reactivity," Whyte, T.E. Jr.; Della Betta, R.A.; Derovane, E.G.; Baker, R.T.K., American Chemical Society, Washington, D.C., 1984, 353.
- 150. Kuznetzov, V.L.; Bell, A.T.; Yermakov, Y.I., <u>J.</u> Catal., 1980, 65, 374.
- 151. Chen, Y.W.; Wang, H.T.; Goodwin, J.G. Jr., Shiflett, W.K., Appl. Catal., 1983, 8, 303.
- 152. Egiebor, N.O., <u>C</u>₁ <u>Mol.</u> <u>Chem.</u>, 1985, <u>1</u>, 253.
- 153. Dalla Betta, R.A.; Shelef, M., <u>J. Catal.</u>, 1977, 48, 111.
- 154. King, D.L., J. Catal., 1980, 61, 77.
- 155. Kellner, C.S.; Bell, A.T., <u>J. Catal.</u>, 1981, <u>71</u>, 296.
- 156. Guglielminotti, E.; Zecchina, A.; Bossi, A.; Camia, M., J. Catal., 1982, 74, 225.
- 157. ibid., 240.
- 158. ibid., 252.
- 159. Rightor, E.G.; Pinnavaia, T.J., to be published, Ultramicroscopy, 1987.
- 160. Flynn, P.C.; Wanke, S.E., <u>J.</u> Catal., 1974, <u>34</u>, 396.
- 161. Pulvermacher, B.; Ruckenstein, E., <u>J. Catal.</u>, 1974, <u>35</u>, 115.
- 162. Avery, N.R.; Sanders, J.V., J. Catal., 1970, 18, 129.
- 163. Volta, J.C.; Tatibouet, J.M., <u>J. Catal.</u>, 1985, <u>95</u>, 467.

- 164. Lee, H.H.; Ruckenstein, E., <u>Catal.</u> <u>Rev.-Sci. Eng.</u>, 1983, <u>25(4)</u>, 475.
- 165. King, D.L., <u>J. Catal.</u>, 1978, <u>51</u>, 386.
- 166. Okuhara, T.; Kumura, T.; Kobayashi, K.; Misono, M.; Yoneda, Y., Bull. Chem. Soc. Japan, 1984, 57, 938.
- 168. Treacy, M.M.J.; Howie, A., J. Catal., 1980, 63, 265.
- 169. Crewe, A.V.; Langmore, J.P.; Isaacson, M.S.,
 "Physical Aspects of Electron Microscopy and
 Microbeam Analysis," Siegel, B.M.; Beaman, D.R., J.
 Wiley, New York, 1975, 47.
- 170. Cowley, J.M., "Scanning Electron Microscopy/1982,"

 Johari, ed., (SEM, AMF, O'Hare, IL, 1983), volume 1,

 51.
- 171. Howie, A.; Marks, L.D.; Penneycook, S.J., Ultramicroscopy, 1982, 8, 175.
- 172. Schulz, H., C₁ Mol. Chem., 1985, 1, 231.
- 173. Kellner, C.S.; Bell, A.T., J. Catal., 1981, 70, 418.
- 174. Chen, Y.W.; Wang, H.T.; Goodwin, J.G. Jr., <u>J. Catal.</u>, 1984, 85, 499.
- 175. Chen, Y.W.; Wang, H.T.; Goodwin, J.G. Jr., <u>J. Catal.</u>, 83, 415.
- 176. Tatsumi, T.; Shul, Y.G.; Sugivra, T.; Tominaga, H., Appl. Catal, 1986, 21, 119.
- 177. Okuhara, T.; Tamura, H.; Misono, M., <u>J. Catal.</u>, 1985, <u>95</u>, 41.
- 178. Wang, H.T.; Chen, Y.W.; Goodwin, J.G. Jr., <u>Zeolites</u>, 1984, <u>4</u>, 57.
- 179. Winslow, P.; Bell, A.T., <u>J. Catal.</u>, 1985, <u>91</u>, 142.
- 180. Egiebor, N.O.; Cooper, W.C., <u>Appl.</u> <u>Catal.</u>, 1985, <u>17</u>, 47.
- 181. Chuang, S.C.; Tian, Y.H.; Goodwin, J.G. Jr.; Wender, I., <u>J.</u> Catal., 1985, <u>96</u>, 396.

- 182. Sajkowski, D.J.; Lee, S.Y.; Schwank, J.; Tian, Y.H.; Goodwin, J.G., J. Catal., 1986, 97, 549.
- 183. Lineweaver, L.J., <u>J. Appl. Phys.</u>, 1983, <u>34</u>, 1786.
- 184. Thomas, L.E., <u>Ultramicroscopy</u>, 1985, <u>18</u>, 173.
- 185. Crewe, A.V., Chem. Scripta., 1978-79, 14, 17.
- 186. Harris, W.J., Nature, 1962, 196, 499.
- 187. Brunauer, S.; Emmett, P.H.; Teller, E., <u>J. Am. Chem.</u>
 <u>Soc.</u>, 1938, <u>60</u>, 5.
- 188. Lowell, S.; Shields, J.E., <u>Powder Surface Area and Porosity</u>, Chapman and Hall, New York, Chapter 4.
- 189. Buessemeier, B.; Frohning, C.D.; Cornils, B.,
 Hydrocarbon Processing, November 1976, 55(3), 105.